NASA CR–189191
Contract NAS3–23940

Elevated Temperature Crack Growth

Final Report

K.S. Kim, R.H. Van Stone

GE Aircraft Engines
Cincinnati, Ohio 45215

December 1992

Prepared for
National Aeronautics and Space Administration
Lewis Research Center
21000 Brookpark Drive
Cleveland, Ohio 44135

National Aeronautics and Space Administration

(NASA-CR-189191) ELEVATED TEMPERATURE CRACK GROWTH Final Report, Aug. 1988 - Jun. 1992 (GE) 117 p

N93-19992

Unclas

G3/39 0148136

NASA
National Aeronautics and Space Administration

Report Documentation Page

1. Report No.	2. Government Accession No.	3. Recipient's Catalog No.
NASA–CR– 189191		

4. Title and Subtitle	5. Report Date
Elevated Temperature Crack Growth	December 1992
	6. Performing Organization Code

7. Author(s)	8. Performing Organization Report No.
K.S. Kim R.H. Van Stone	R89AEB325–01
	10. Work Unit No.

9. Performing Organization Name and Address	11. Contract or Grant No.
GE Aircraft Engines Advanced Technology Operation One Neumann Way Cincinnati, OH 45215–6301	NAS3–23940
	13. Type of Report and Period Covered
12. Sponsoring Agency Name and Address	Final Report August 88 – June 92
National Aeronautics and Space Administration Lewis Research Center Cleveland, Ohio 44135–3191	14. Sponsoring Agency Code

15. Supplementary Notes

16. Abstract

The purpose of this program was to extend the work performed in the base program (CR182247) into the regime of time-dependent crack growth under isothermal and thermal mechanical fatigue (TMF) loading, where creep deformation also influences the crack growth behavior. The investigation was performed in a two-year, six-task, combined experimental and analytical program. The path-independent integrals for application to time-dependent crack growth were critically reviewed. The crack growth was simulated using a finite element method. The path-independent integrals were computed from the results of finite-element analyses. The ability of these integrals to correlate experimental crack growth data were evaluated under various loading and temperature conditions. The results indicate that some of these integrals are viable parameters for crack growth predicition at elevated temperatures.

17. Key Words (Suggested by Author(s))	18. Distribution Statement
Elastic-plastic fracture mechanics, thermomechanical fatigue, fatigue crack growth, time-dependent crack growth, Alloy 718, finite element method, path-independent integral	

19. Security Classification (of this report)	20. Security Classification (of this page)	21. No. of pages	22. Price*
Unclassified	Unclassified	104	

Table of Contents

Section		Page
1.0	**Introduction**	**1**
2.0	**Review of Path-Independent Integrals for Time-Dependent Deformation**	**9**
2.1	Review of Path-Independent Integrals	9
2.1.1	The C*-integral	10
2.1.2	The $\hat{J}$-Integral and Its Rate Form	12
2.1.3	The J*-Integral and Its Rate Form	13
2.1.4	The ΔT-Integrals	14
2.2	Computation of Path-Independent Integrals	16
2.3	Conclusions	18
3.0.	**Crack Growth Under Thermomechanical Loading and Temperature Gradients**	**19**
3.1	Finite Element Analysis of Crack Growth	19
3.2	Results of Analysis	19
3.3	Conclusions	28
4.0	**Crack Growth Analysis on Hastelloy-X**	**29**
4.1	Method of Analysis	29
4.2	Results of Analysis	32
4.3	Conclusion	46
5.0	**Input for Finite Element Analysis of Time-Dependent Crack Growth**	**50**
5.1	Constitutive Theory	50
5.1.1	Creep Data Analysis	50
5.2	Boundary Conditions	55
6.0	**Crack Growth Under Static Loading Conditions**	**66**
6.1	Crack Growth Test	66
6.2	Finite Element Analysis of Crack Growth	66
6.3	Results of Analysis	68
6.4	Conclusion	71

Table of Contents (Concluded)

Section		Page
7.0	**Crack Growth Under Strain Cycling With Hold Time**	**80**
7.1	Crack Growth Test	80
7.2	Finite Element Analysis of Crack Growth	83
7.3	Prediction of Crack Growth Rate	83
7.4	Results of Analysis	84
7.5	Conclusion	94
8.0	**Crack Growth Under Thermomechanical Fatigue Loading With Hold Time**	**95**
8.1	Crack Growth Test	95
8.2	Crack Growth Results	95
9.0	**Summary and Recommendations**	**96**
References		**98**

List of Illustrations

Figure		Page
1.	Buttonhead single edge notch (SEN) specimen.	2
2.	Schematic drawing of triple extensometer buttonhead SEN test method.	3
3.	Variation of (a) stress, (b) control displacement, (c) CMOD, (d) back face displacement with cycles at maximum strain, minimum strain, crack closing and opening points of Alloy 718 specimen N4–3.	4
4.	Finite element model of the gage section of single edge notch specimen.	5
5.	Variation of the predicted and experimental (a) average stress and (b) CMOD range with crack length for Alloy 718 specimen N4–3.	6
6.	Comparison of predicted and experimental stress – CMOD hysteresis loops at crack length (a) 0.95 mm, (b) 2.54 mm for Alloy 718 specimen N4–3.	7
7.	Correlation of Alloy 718 cyclic crack growth data at 538°C with (a) $\Delta\hat{J}$, (b) ΔJ^*, (c) ΔTp, and (d) ΔTp^*.	8
8.	Integration paths and areas.	10
9.	Load cases and creep times for constant strain analysis of rate integrals.	16
10.	Variation of $\hat{J}$ with path (ε=0.01).	17
11.	Variation of $\dot{\hat{J}}$ with path (ε=0.01).	17
12.	Variation of C* with path (ε=0.01).	17
13.	Relaxation of the normal stress ahead of the crack tip (ε=0.01).	17

List of Illustrations (Continued)

Figure		Page
14.	Schematic of loading steps and crack lengths in crack growth simulation without hold time for SEN specimen.	20
15.	Comparison of trilinear approximation and experimental data in Alloy 718 temperature gradient tests.	21
16.	Variation of the average stress with crack length for Alloy 718 TMF specimens (a) N5–43, (b) N5–29, (c) N5–25, and (d) N4–36.	22
17.	Variation of the average stress with crack length for Alloy 718 temperature gradient specimens (a) N5–5 and (b) N4–39.	23
18.	Variation of the CMOD with crack length for Alloy 718 TMF specimens (a) N5–43, (b) N5–29, (c) N5–25, and (d) N4–36.	24
19.	Variation of the CMOD with crack length for Alloy 718 temperature gradient specimens (a) N5–5 and (b) N4–39.	25
20.	Variation of (a) $\hat{J}$ and (b) Tp* with path for Alloy 718 specimen N5–29.	26
21.	Variation of (a) $\hat{J}$ and (b) Tp* with path for Alloy 718 specimen N4–39.	26
22.	Correlation of Alloy 718 cyclic thermomechanical and temperature gradient crack growth data with ΔJ^*.	27
23.	Correlation of Alloy 718 cyclic thermomechanical and temperature gradient crack growth data with $\Delta\hat{J}$.	27
24.	Correlation of Alloy 718 cyclic thermomechanical and temperature gradient crack growth data with ΔTp^*.	27

List of Illustrations (Continued)

Figure		Page
25.	Correlation of Alloy 718 cyclic thermomechanical and temperature gradient crack growth data with ΔTp.	27
26.	Comparison of temperature effects on the Alloy 718 crack growth data correlation with (a) ΔJ^* and (b) $\Delta \hat{J}$.	28
27.	Tubular crack growth test specimen of Hastelloy-X.	29
28.	The cyclic stress – strain curves of Hastelloy-X used for finite element analysis of crack growth.	31
29.	The CCP finite element model of Hastelloy-X.	32
30.	The predicted plastic zone size in Hastelloy-X at (a) 427°C, $\Delta\varepsilon$=0.15% and a/W=0.25 and (b) 982°C, $\Delta\varepsilon$=0.40% and a/W=0.25.	33
31.	Variation of predicted Hastelloy-X average stress with crack length at various temperatures and $\Delta\varepsilon$=0.40%.	34
32.	Predicted Hastelloy-X crack profiles at various crack lengths at (a) 427°C and $\Delta\varepsilon$=0.40% and (b) 982°C and $\Delta\varepsilon$=0.40%.	35
33.	Influence of path on the variation of (a) $\hat{J}$ at 427°C and $\Delta\varepsilon$=0.4%, (b) Tp* at 427°C and $\Delta\varepsilon$=0.4%, (c) $\hat{J}$ at 982°C and $\Delta\varepsilon$=0.4%, and (d) Tp* at 982°C and $\Delta\varepsilon$=0.4%.	36
34.	Correlation of Hastelloy-X 427°C isothermal crack growth data with (a) ΔJ^*, (b) $\Delta \hat{J}$, (c) ΔTp^*, and (d) ΔTp.	37
35.	Correlation of Hastelloy-X 649°C isothermal crack growth data with (a) ΔJ^*, (b) $\Delta \hat{J}$, (c) ΔTp^*, and (d) ΔTp.	38

List of Illustrations (Continued)

Figure		Page
36.	Correlation of Hastelloy-X 871°C isothermal crack growth data with (a) ΔJ^*, (b) $\Delta\hat{J}$, (c) ΔTp^*, and (d) ΔTp.	39
37.	Correlation of Hastelloy-X 927°C isothermal crack growth data with (a) ΔJ^*, (b) $\Delta\hat{J}$, (c) ΔTp^*, and (d) ΔTp.	40
38.	Correlation of Hastelloy-X 982°C isothermal crack growth data with (a) ΔJ^*, (b) $\Delta\hat{J}$, (c) ΔTp^*, and (d) ΔTp.	41
39.	Comparison of Hastelloy-X isothermal crack growth rates as a function of (a) ΔJ^*, (b) $\Delta\hat{J}$, and (c) ΔTp^*.	42
40.	Correlation of Hastelloy-X out–of–phase 427°C – 871°C TMF crack growth data with (a) ΔJ^*, (b) $\Delta\hat{J}$, and (c) ΔTp^*.	43
41.	Correlation of Hastelloy-X 427°C – 927°C TMF crack growth data with (a) ΔJ^*, (b) $\Delta\hat{J}$, and (c) ΔTp^*.	44
42.	Correlation of Hastelloy-X out–of–phase 427°C – 927°C TMF crack growth data with (a) ΔJ^*, (b) $\Delta\hat{J}$, and (c) ΔTp^*.	45
43.	Comparison of Hastelloy-X 427°C – 871°C TMF with 427°C and 871°C isothermal crack growth data as a function of (a) ΔJ^*, (b) $\Delta\hat{J}$, and (c) ΔTp^*.	47
44.	Comparison of Hastelloy-X 427°C – 927°C in-phase TMF with 427°C and 927°C isothermal crack growth data as a function of (a) ΔJ^*, (b) $\Delta\hat{J}$, and (c) ΔTp^*.	48
45.	Comparison of Hastelloy-X 427°C – 927°C out-of-phase TMF with 427°C and 927°C isothermal crack growth data as a function of (a) ΔJ^*, (b) $\Delta\hat{J}$, and (c) ΔTp^*.	49

List of Illustrations (Continued)

Figure		Page
46.	Four-element model used for Alloy 718 stress relaxation analysis.	51
47.	Alloy 718 creep strain versus time at 538°C.	52
48.	Alloy 718 stress relaxation at 538°C with (a) large and (b) small times.	53
49.	Magnitude of Alloy 718 relaxed stress at 538°C for (a) large and (b) small times.	54
50.	Alloy 718 creep strain versus time at 593°C.	55
51.	Alloy 718 stress relaxation at 593°C with (a) large and (b) small times.	56
52.	Magnitude of Alloy 718 relaxed stress at 593°C for (a) large and (b) small times.	57
53.	Alloy 718 creep strain versus time at 649°C.	58
54.	Alloy 718 stress relaxation at 649°C with (a) large and (b) small times.	59
55.	Magnitude of Alloy 718 relaxed stress at 649°C for (a) large and (b) small times.	60
56.	Variation of (a) stress, (b) control displacement, (c) back face displacement, (d) front face displacement with cycles in Alloy 718 specimen N11–32.	61
57.	Hysteresis loops of (a) control displacement, (b) back face displacement, and (c) front face displacement at cycle 16 of Alloy 718 specimen N11–32.	62
58.	Hysteresis loops of (a) control displacement, (b) back face displacement, and (c) front face displacement at cycle 44 of Alloy 718 specimen N11–32.	63
59.	Comparison of Alloy 718 experimental front face displacements with the linear and offset extrapolation of remote displacements.	64

List of Illustrations (Continued)

Figure		Page
60.	Comparison of predicted (a) stress, (b) CMOD, and (c) CMOD range in Alloy 718 with crack length for linear and offset extrapolation of remote displacement boundary conditions.	65
61.	Correlation of Alloy 718 static crack growth data with stress intensity factor at (a) 593°C and (b) 649°C.	67
62.	Schematic of the modeling scheme for Alloy 718 crack growth simulation under static control conditions.	68
63.	Predicted Alloy 718 crack profiles during crack propagation at 649°C under (a) 0.75% constant strain and (b) 706 MPa constant stress.	69
64.	Variation of the average stress with crack length in Alloy 718 static loaded tests at (a) 593°C and (b) 649°C.	70
65.	Variation of CMOD with crack length in Alloy 718 static loaded tests at (a) 593°C and (b) 649°C.	72
66.	Variation of (a) J*, (b) $\hat{J}$, and (c) Tp* with path for Alloy 718 specimen N11–45.	73
67.	Variation of (a) $\dot{J}$*, (b) $\dot{\hat{J}}$, and (c) $\dot{T}$p* with path for Alloy 718 specimen N11–45.	74
68.	Variation of Alloy 718 time dependent crack growth rate at 593°C with (a) J*, (b) $\hat{J}$, and (c) Tp*.	75
69.	Variation of Alloy 718 time dependent crack growth rate at 593°C with (a) $\dot{J}$*, (b) $\dot{\hat{J}}$, and (c) $\dot{T}$p*.	76

List of Illustrations (Continued)

Figure		Page
70.	Variation of Alloy 718 time dependent crack growth rate at 649°C with (a) J*, (b) $\hat{J}$, and (c) Tp*.	77
71.	Variation of Alloy 718 time dependent crack growth rate at 649°C with (a) $\dot{J}$*, (b) $\dot{\hat{J}}$, and (c) $\dot{T}p$*.	78
72.	Comparison of Alloy 718 time-dependent crack growth rates at 593°C and 649°C with (a) $\dot{J}$* and (b) $\dot{\hat{J}}$.	79
73.	Variation of 593°C R_ε=0 Alloy 718 cyclic crack growth rates with (a) K_{max}, (b) ΔK, and (c) ΔK_{eff}.	81
74.	Variation of 649°C Rε=0 Alloy 718 cyclic crack growth rates with (a) K_{max}, (b) ΔK, and (c) ΔK_{eff}.	82
75.	Schematic of the modeling scheme for Alloy 718 crack growth simulation under strain cycling with hold time.	83
76.	Variation of the average stress with crack length for R_ε=0 593°C Alloy 718 hold time tests with Δε of (a) 0.4% and (b) 1.15%.	85
77.	Variation of the average stress with crack length for R_ε=0 649°C Alloy 718 hold time tests with Δε of (a) 0.4% and (b) those greater than 1.00%.	86
78.	Variation of the CMOD range with crack length for R_ε=0 593°C Alloy 718 hold time tests with Δε of (a) 0.4% and (b) 1.15%.	87
79.	Variation of the CMOD range with crack length for R_ε=0 649°C Alloy 718 hold time tests with Δε of (a) 0.4% and (b) those greater than 1.00%.	88
80.	Correlation of Alloy 718 cyclic crack growth data at 593°C, R_ε=0 with (a) ΔJ* and (b) $\Delta\hat{J}$.	89

List of Illustrations (Concluded)

Figure		Page
81.	Correlation of Alloy 718 cyclic crack growth data at 649°C, R_ε=0 with (a) ΔJ^* and (b) $\Delta\hat{J}$.	90
82.	Comparison of experimental and predicted Alloy 718 hold time crack growth data at 593°C using (a) $\Delta J^* - \dot{J}^*$ and (b) $\Delta\hat{J} - \dot{\hat{J}}$ superposition methods.	91
83.	Comparison of experimental and predicted Alloy 718 hold time crack growth data at 649°C using (a) $\Delta J^* - \dot{J}^*$ and (b) $\Delta\hat{J} - \dot{\hat{J}}$ superposition methods.	91
84.	Comparison of experimental and predicted Alloy 718 hold time crack growth data at 593°C using (a) $\Delta J^* - \dot{J}^*$ and (b) $\Delta\hat{J} - \dot{\hat{J}}$ modified superposition methods.	92
85.	Comparison of experimental and predicted Alloy 718 hold time crack growth data at 649°C using (a) $\Delta J^* - \dot{J}^*$and (b) $\Delta\hat{J} - \dot{\hat{J}}$ modified superposition methods.	92
86.	Variation of β in Alloy 718 as a function of hold time and ε_{max} at (a) 593°C and (b) 649°C.	93
87.	Variation of Alloy 718 crack growth rate with K_{max} for continuously cycled $R_\varepsilon = 0$ 427°–649°C TMF tests.	96
88.	Variation of Alloy 718 crack growth rate with K_{max} for in-phase $R_\varepsilon = 0$ 427°–649°C TMF tests with a mechanical strain range of 0.40%.	98
89.	Variation of Alloy 718 crack growth rate with K_{max} for in-phase $R_\varepsilon = 0$ 427°–649°C TMF tests with a mechanical strain range of 1.15%.	99
90.	Variation of Alloy 718 crack growth rate with K_{max} for out-of-phase $R_\varepsilon = 0$ 427°–649°C TMF tests.	100

List of Tables

Table		Page
1.	Hastelloy-X Specimens Evaluated Using FEM Crack Growth Simulation.	30
2.	Creep Constants of Alloy 718.	51
3.	Alloy 718 Crack Growth Test conditions Under Static Control.	66
4.	Strain and Temperature Conditions for Alloy 718 Hold Time Crack Growth Tests.	80
5.	Strain and Temperature Conditions for Alloy 718 TMF/Hold Time Crack Growth Tests.	95

1.0 Introduction

Critical gas turbine engine hot section components such as blades, vanes, and combustor liners tend to develop minute cracks during the early stages of operation. These cracks may then grow under conditions of fatigue and creep to critical size. Current methods of predicting growth rates or critical crack sizes are inadequate, which leaves only two extreme courses of action. The first is to take an optimistic view, with the attendant risk of an excessive number of service failures. The second is to take a pessimistic view and accept an excessive number of "rejections for cause" at considerable expense in parts and downtime. Clearly, it is very desirable to develop reliable methods of predicting crack growth rates and critical crack sizes.

To develop such methods, it is desirable to relate the processes that control crack growth in the immediate vicinity of the crack tip to parameters that can be calculated from the remote field data. The most likely parameters appear to be certain path-independent (P-I) integrals, several of which have already been proposed for application to problems involving inelastic deformation and thermal strains. A thorough analytical and experimental evaluation of these parameters needs to be made under the loading conditions which would include elevated temperature isothermal and thermal-mechanical fatigue, both with and without thermal gradients and hold times.

Previous work during the base program[1] surveyed available P-I integrals[2], used finite element analysis to simulate the growth of fatigue cracks in Alloy 718 experiments, and showed that experimental crack growth rates measured over a wide range of elastic and elastic-plastic cyclic deformation conditions could be correlated using several of the P-I integrals. The finite element analysis of crack propagation and the computation of P-I integrals were based on the assumption of time-independent deformation in the base program.

This program is in many ways an extension of, and has been supported by, several previous NASA programs. The technical approach is built upon a base program which was funded by the NASA HOST (HOt Section Technology) Program. Supporting experimental data was acquired in a pre–HOST NASA program. Funding for the current program was provided by the Earth–To–Orbit Propulsion Technology Program.

The purpose of this program was to extend that work into the regime of time-dependent crack growth under isothermal and thermal mechanical fatigue (TMF) loading, where creep deformation also influences the crack growth behavior. The investigation was performed in a two-year, six-task, combined experimental and analytical program. The six tasks are:

- Review and analytical evaluation of path-independent integrals for time-dependent deformation
- Analytical and experimental evaluation of crack growth under constant strain or stress
- Analytical and experimental evaluation of crack growth under strain cycling with hold time at maximum strain
- Experimental study of crack growth under thermomechanical cycling with hold time at maximum or minimum strain
- Analysis of crack growth data on Hastelloy-X reported by Meyers, et al.[3]
- Report the results of the investigation.

The results obtained in these first five tasks will be described in detail in the following sections. Also included in the report are the results of time-independent deformation analysis on several specimens tested under thermomechanical loading and thermal gradient conditions. These data were obtained in the base program, but not analyzed.

The results in the following sections are highly dependent on the progress made in the base program, so the major results are summarized for completeness.

The path-independent integrals for time-independent deformation were reviewed[2] with emphasis on whether or not the path-independence is maintained for the mechanical and thermal loading conditions used in the program. The physical meaning, the computational aspects and relations among P-I integrals were also examined. The J^*, $\hat{J}$, ΔTp^*, and ΔTp integrals were shown to be path-independent under all combinations of thermoelastic-plastic loading conditions considered including inhomogeneous material properties which can arise from thermal gradients. These P-I integrals were selected for evaluation of their ability to correlate experimentally measured crack growth data.

The material chosen in this program was γ''-strengthened nickel-base Alloy 718. The composition, microstructure, and heat treatment of the Alloy 718 plates used throughout this investigation were described previously[1]. The constitutive properties of this material was measured over the temperature range of 427° to 649°C under monotonic tension, cyclic, and creep deformation.

A button-head single edge notch (SEN) specimen shown in Figure 1 was developed for use in the strain-controlled crack growth tests. This specimen has a short gage length to avoid buckling under fully reversed (R_ε=-1) loading. Analytical and experimental evaluations were performed to define the maximum strain to be applied without buckling and to verify the validity of the boundary conditions to be used during finite element simulation of crack growth and crack closure. It was shown that remote displacements were linear across the width of the test specimen. The Alloy 718 crack growth tests were performed under strain control where the crack length was monitored using a DC potential technique. Extensometers measured the displacements at three locations: (1) center and (2) back face of the specimen at the gage length, and (3) at the crack mouth to measure the crack mouth opening displacement (CMOD) as shown schematically in Figure 2. The measurement at the

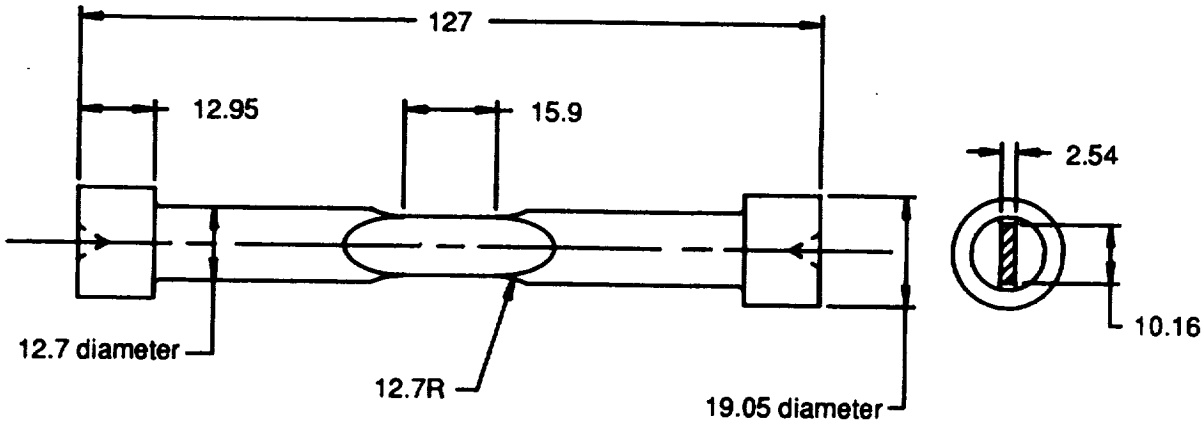

Figure 1. Buttonhead single edge notch (SEN) specimen.

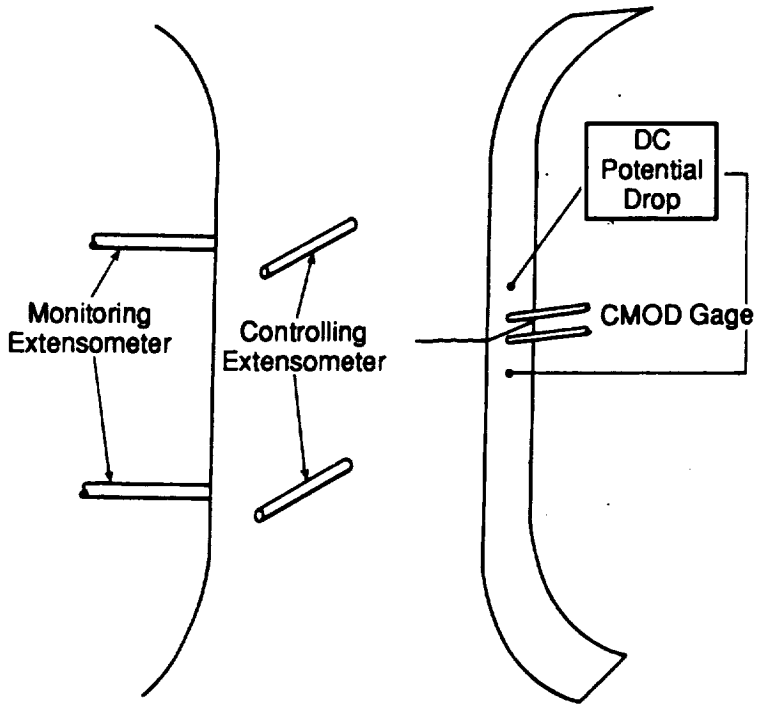

Figure 2. Schematic drawing of triple extensometer buttonhead SEN test method.

center of the specimen was used as the control displacement. The back face displacement along with the center displacement was used to define the boundary conditions at the gage length by linear extrapolation. The load and CMOD were used to verify the accuracy of the finite element analyses of crack growth and crack closure. A typical example of the measured load and displacements are shown in Figure 3.

The finite element analysis of crack propagation and crack closure was performed on three specimens tested at 538°C with strain ranges of 0.5, 1.15 and 1.70%. The finite element model of the gage section is shown in Figure 4. The crack growth was simulated by releasing nodes at the crack tip cycle by cycle. The predicted and experimental load and CMOD agreed reasonably well as shown in Figure 5. The crack closure was modeled using gap elements. The crack closing and opening was predicted closely with the experimental data as shown in Figure 6.

The four selected path-independent integrals were computed along several paths. The results showed path-independence. The range of these P-I integrals from the minimum strain to the maximum strain (approximately equal to the range from the crack opening point to the maximum strain) were used to correlate the crack growth data. It was found that all these integrals correlate the data very well as shown in Figure 7.

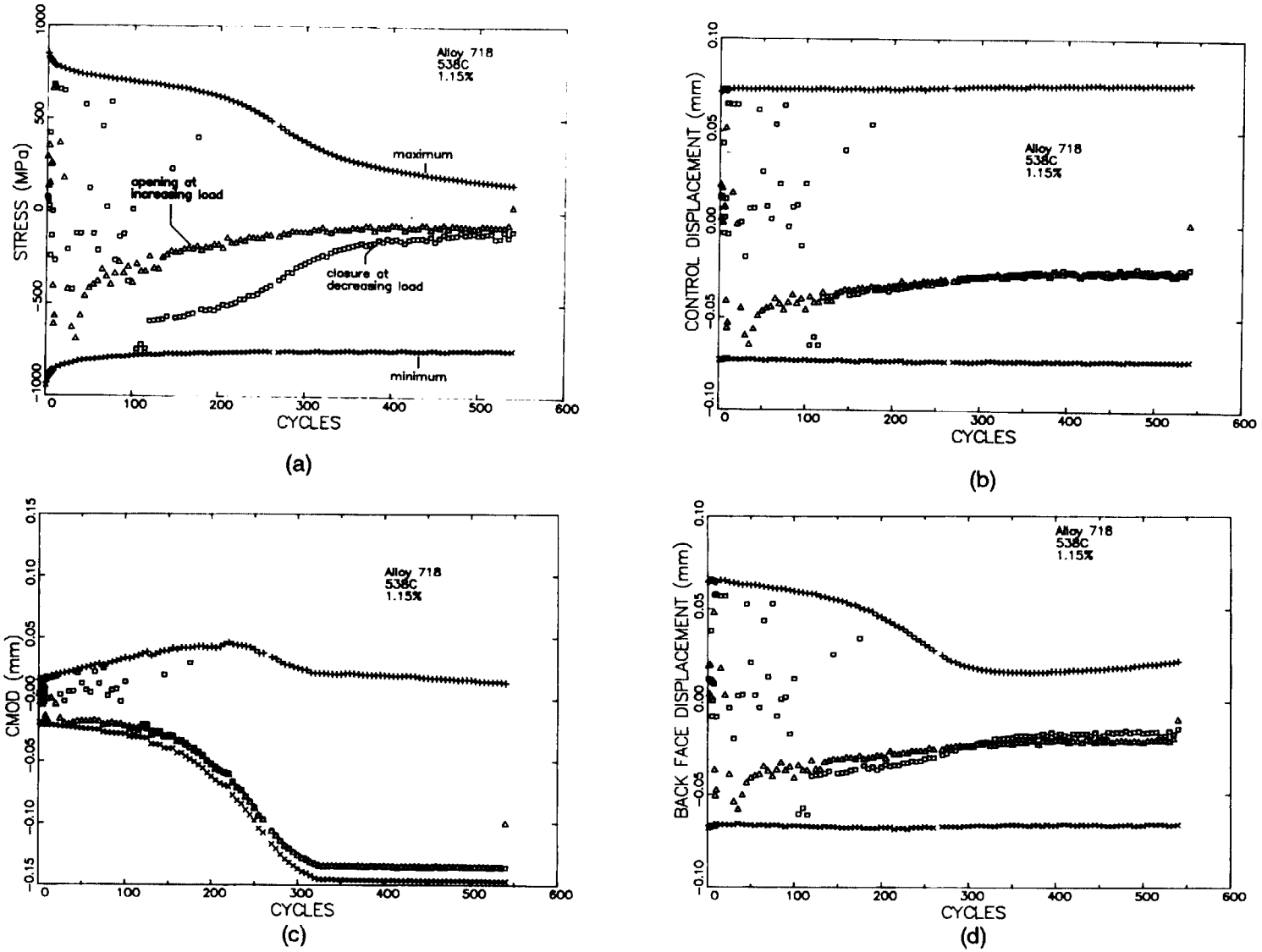

Figure 3. Variation of (a) stress, (b) control displacement, (c) CMOD, (d) back face displacement with cycles at maximum strain, minimum strain, crack closing and opening points of Alloy 718 specimen N4–3.

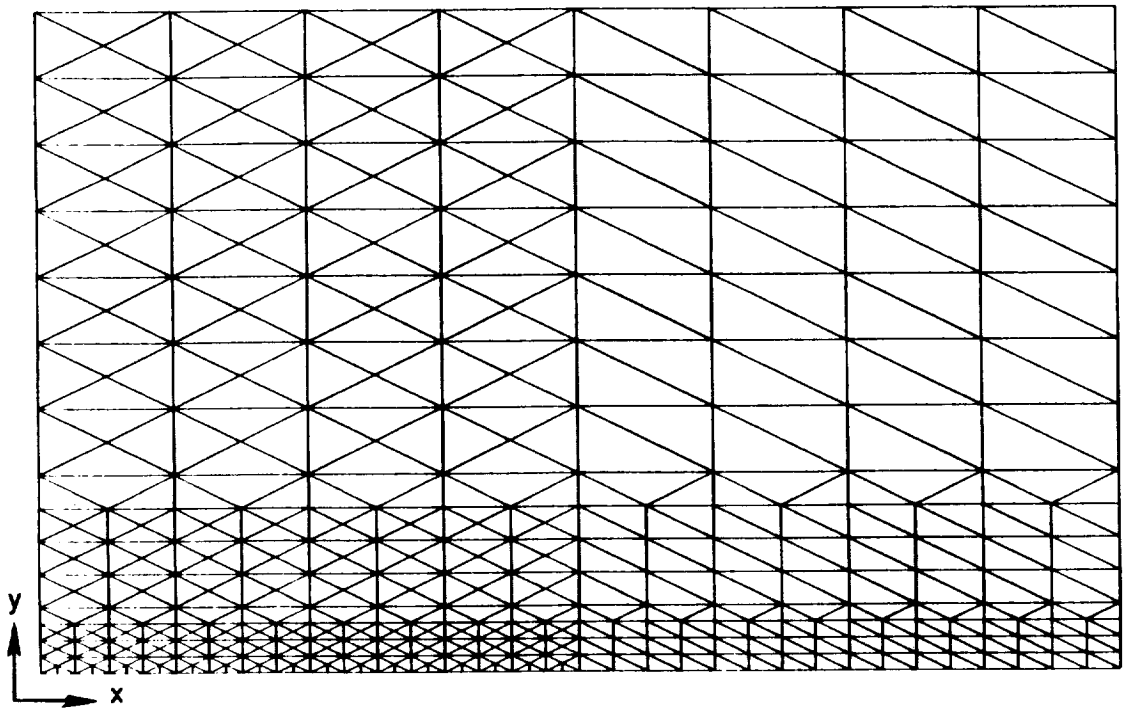

Figure 4. Finite element model of the gage section of single edge notch specimen.

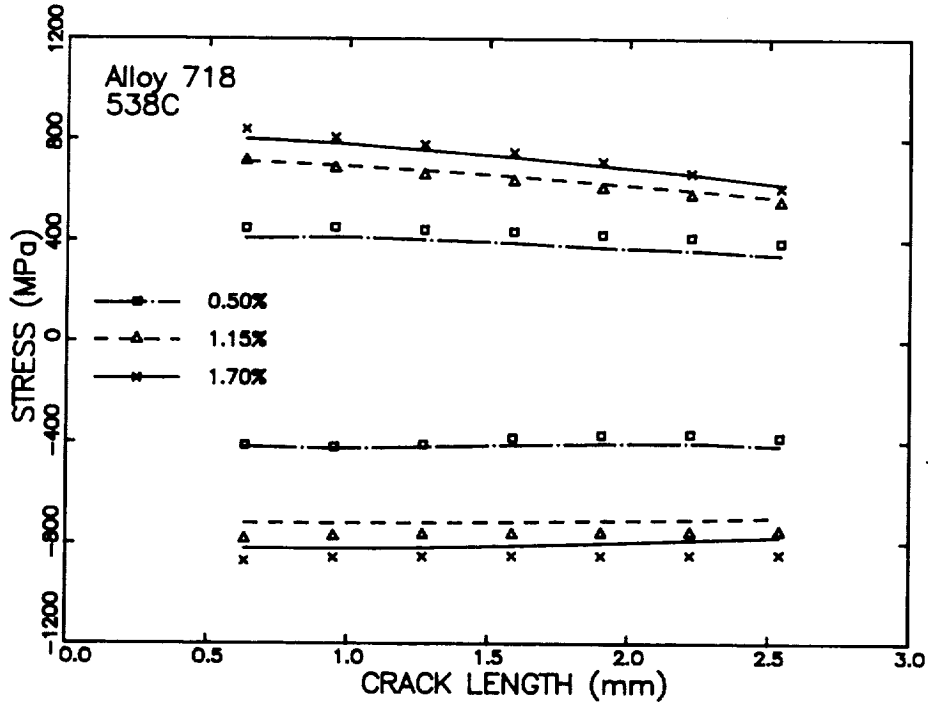

(a)

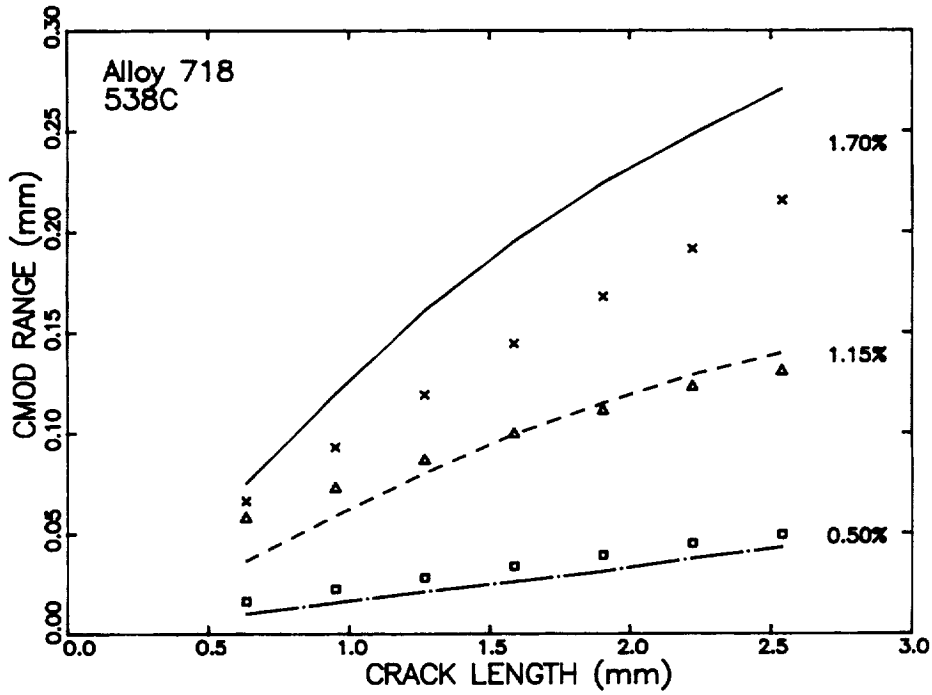

(b)

Figure 5. Variation of the predicted and experimental (a) average stress and (b) CMOD range with crack length for Alloy 718 specimen N4–3.

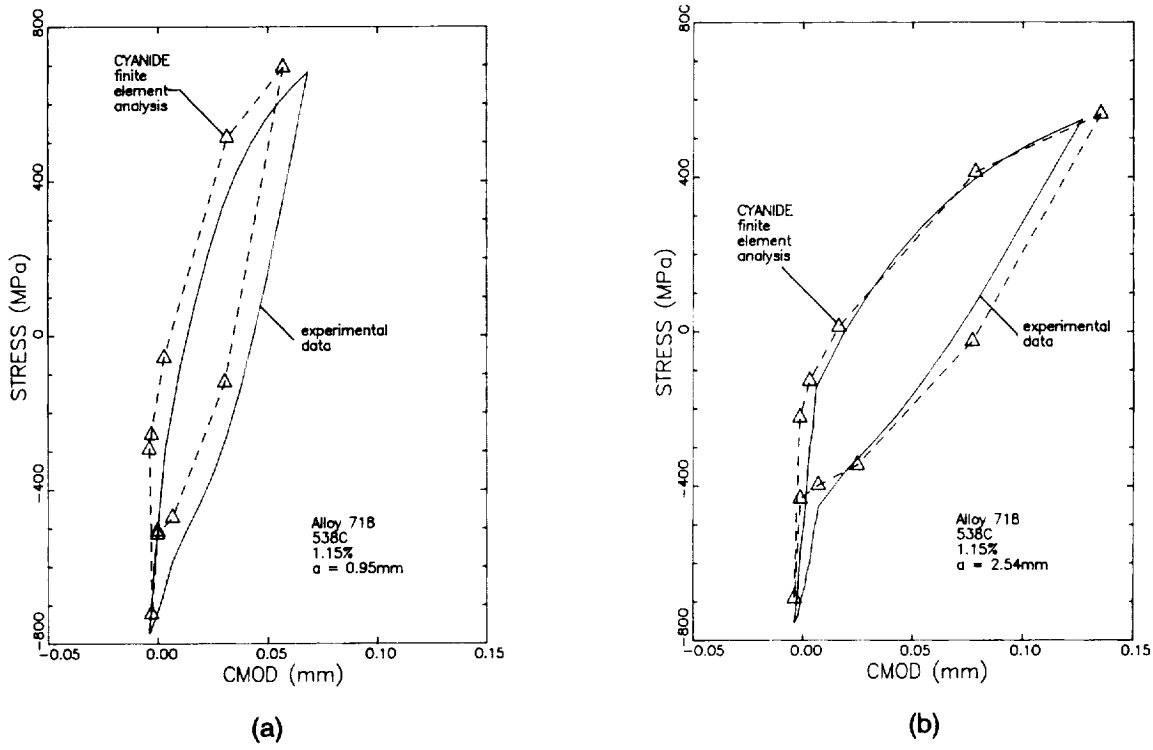

Figure 6. Comparison of predicted and experimental stress – CMOD hysteresis loops at crack length (a) 0.95 mm, (b) 2.54 mm for Alloy 718 specimen N4–3.

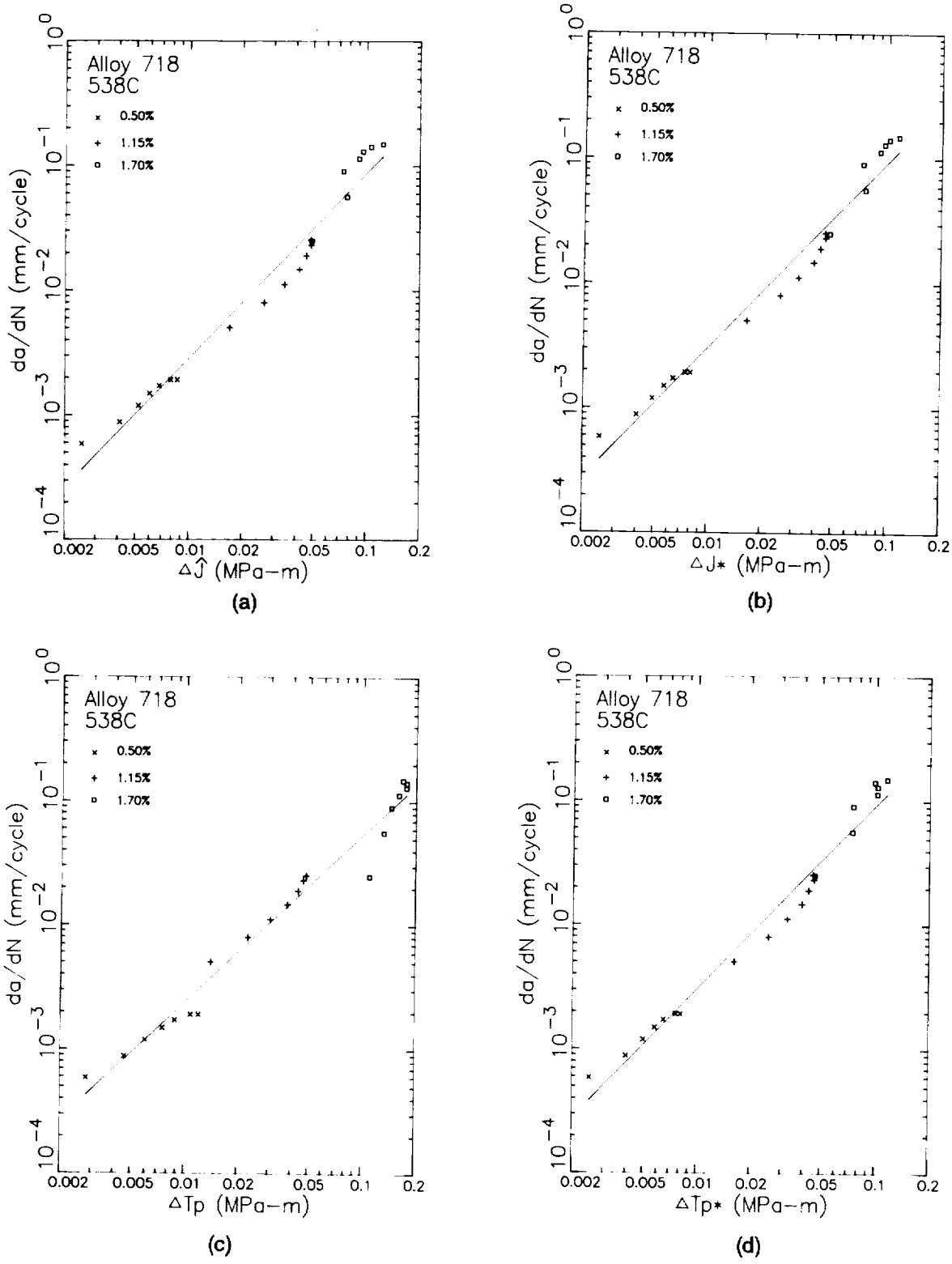

Figure 7. Correlation of Alloy 718 cyclic crack growth data at 538°C with (a) $\Delta\hat{J}$, (b) ΔJ^*, (c) ΔTp, and (d) ΔTp^*.

2.0 Review of Path-Independent Integrals for Time-Dependent Deformation

The J-integral[4] has been widely used in elastic-plastic fracture mechanics. Its application includes determining the stress intensity factors using the stress and strain fields away from the crack tip, predicting ductile crack propagation under monotonic tensile loading[5], and predicting fatigue crack growth using operational definitions of the range of the J-integral[6,7]. The theoretical basis of the J-integral, however, does not permit its application to crack growth prediction in many circumstances including cyclic loading with significant plasticity, thermomechanical loading, and thermal gradients. In efforts to remove these barriers, researchers have proposed new path-independent (P-I) integrals. Most of these new P-I integrals are, however, not given in the form of a conservation law like the J-integral. They include area integrals in addition to line integrals. Thus, the path-independence must be interpreted in a nonclassical sense; that the sum of a line integral along a path surrounding the crack tip and an area integral over the area enclosed by the path is independent of the path. These new P-I integrals proposed for application to the elastic-plastic fracture mechanics were reviewed in the base program[2]. Although the physical meanings of these integral parameters are not as clearly defined as the J-integral, these can be related to known crack tip parameters such as K and J in certain loading conditions[2] and therefore can be considered as candidate parameters for crack growth prediction. In fact, the results of the base program for isothermal cases indicated that these integrals might be useful parameters.

The previous review[2] limited itself to elastic-plastic (time-independent) deformation. One purpose of this program was to extend the review to time-dependent deformation. The time-dependent deformation concerned in this report is the viscoplastic (creep) deformation, which can occur in metallic components operating at elevated temperatures. The review will cover the utility of the P-I integrals in this category under realistic conditions including cyclic loading with substantial inelastic deformation, thermomechanical loading, temperature gradients, and material inhomogeneities. The inertia effects, the body force, and large deformation were not considered in the review.

A few example analyses were carried out for the stress and deformation field of a single edge notch specimen subject to different loading and temperature conditions. The in-house elastic-inelastic finite element code, CYANIDE, was used for these evaluations. The P-I integrals were computed and the path-independence of the numerical results was examined.

2.1 Review of Path-Independent Integrals

Some of the P-I integrals reviewed in the base program[2] are obviously inapplicable to time-dependent deformation. These are the J-integral[4], two thermoelastic integrals by Wilson and Yu[8], and by Gurtin[9], and Ainsworth et al. integral[10]. These integrals were not considered further in this review. The P-I integrals considered were:

- The C*-integral[11,12]
- The J*-integral[13] and its rate form
- The $\hat{J}$ -integral[14] and its rate form[15]
- The ΔT-integrals[16] and T* integral[17]

These integrals are reviewed individually in the following sections. For nomenclature pertinent to the integration path and area, the reader is referred to Figure 8.

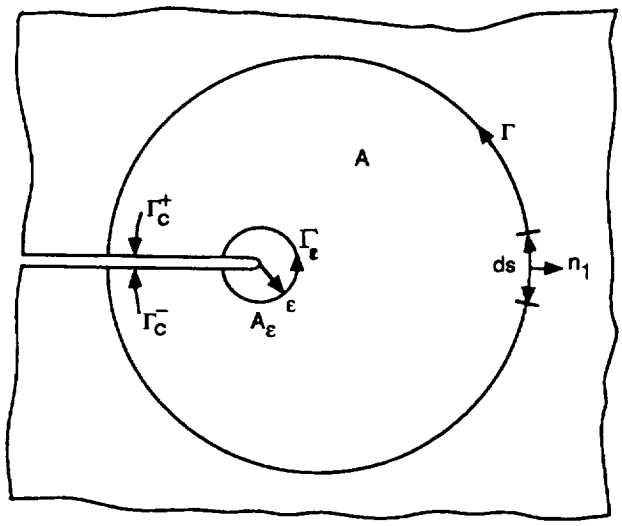

Figure 8. Integration paths and areas.

2.1.1 The C*-integral

Using the similarity of the constitutive relations between the Ramberg-Osgood equation for elastic-plastic deformation and the power law steady state creep equation, one can readily infer that the J-integral[4] can hold for creep deformation if the strains and displacements in the integral are replaced by their rates and the energy density is replaced by a rate potential. This was noticed by Goldman and Hutchinson[11]. Landes and Begley[12] used the term C* to designate the rate integral thus generated, and utilized it to correlate their crack growth data. The C*-integral is defined by

$$C^* = \int_\Gamma (W^* n_1 - t_i \dot{u}_{i,1}) ds \tag{1}$$

where n_1 is the x_1-component of the outward unit normal on the contour, t_i is the traction vector, u_i is the displacement vector, s is the arc length, $\cdot$ is for the time derivative, and the comma indicates partial differentiation with respect to the following coordinate. The repeated indices, unless otherwise stated, imply summation as in the usual index notation.

$$W^* = \int^{\dot{\varepsilon}_{ij}} \sigma_{ij} d\dot{\varepsilon}_{ij} \tag{2}$$

where σ_{ij} and $\dot{\varepsilon}_{ij}$ are the components of stress and strain rate, respectively.

The existence of an energy rate function (W*) gives a major restriction on the applicability of this integral. Such a function can be found only if the material response follows the secondary or steady-state creep law:

$$\dot{\varepsilon}_{ij} = \alpha(\sigma/\sigma_o)^n \tag{3}$$

where α and n are material constants, σ_o is the reference stress.

The generalization of equation (3) to multiaxial state is given by

$$\dot{\varepsilon}_{ij}/\varepsilon_o = (3/2)\alpha(\sigma_e/\sigma_o)^{n-1}s_{ij}/\sigma_o \tag{4}$$

where the deviatoric stress, s_{ij}, and the effective stress, σ_e, are defined by

$$s_{ij} = \sigma_{ij} - 1/3\ \sigma_{kk}\delta_{ij} \tag{5}$$

$$\sigma_e = (3/2\ s_{ij}s_{ij})^{1/2} \tag{6}$$

The energy rate function is easily obtained as

$$W^* = \alpha(n/n+1)\sigma_e^{n+1} \tag{7}$$

For a nonpropagating crack under the above deformation condition, C* is a single parameter characterizing the crack tip field[11];

$$\sigma_{ij} = \sigma_o(C^*/\alpha\sigma_o\varepsilon_o I_n)^{1/(n+1)}r^{-1/(n+1)}\widetilde{\sigma_{ij}}(\theta) \tag{8}$$

$$\varepsilon_{ij} = \alpha\varepsilon_o(C^*/\alpha\sigma_o\varepsilon_o I_n)^{n/(n+1)}r^{-n/(n+1)}\widetilde{\varepsilon_{ij}}(\theta) \tag{9}$$

Within the classical inelastic theory, the deformation can be represented by addition of the instantaneous elastic-plastic response, creep, and thermal deformation. The deformation condition given by equation (3) represents only the steady-state creep term and excludes the instantaneous response, primary creep and thermal deformation. For the C* integral to be path-independent, this deformation condition must be satisfied at every point in the domain surrounded by the contour of integration excluding the crack tip. Precisely speaking, this state of deformation cannot be achieved even in the simplest case, as in the body with a stationary crack subject to a constant remote stress at a constant temperature. However, the path-independence of the C*-integral can be approximately attained at long times where the strain increment is mainly due to steady state creep.

It has been an issue among researchers if C* is a useful parameter for crack growth prediction under constant loads. Although the remote stress is constant, the crack tip field becomes complicated due to the competing effects between the stress elevation due to crack growth and the stress relaxation due to constrained creep as described by Hawk and Bassani[18]. The problem can be treated as a steady-state case if the crack growth is sufficiently slow and the development of the secondary creep is fast enough. It is generally known that C* is a viable parameter for crack growth prediction in this circumstance[19].

The path-independence of C* is also limited by the restrictions similar to those imposed on the J-integral. They are as follows:

1. The material must be homogeneous (uniform α and n) at least in the crack direction.
2. No body force is acting on the material.
3. The temperature is uniform in space.
4. The crack surface is traction free.

The last condition can evidently be removed if the contour includes the crack surface. As for a crack located at the straight interface of a bi-material, C* is path-independent provided both materials satisfy the constitutive conditions mentioned above. This can be proved in the manner similar to Smelser and Gurtin[21]. If the interface is inclined to the crack, we will see a term with the jump of the integrand across the interface integrated along the interface. The C* is interpreted

as the power (or energy rate) difference between two identically loaded bodies having incrementally differing crack lengths, i.e.,

$$C^* = -\frac{dU^*}{da} \tag{10}$$

where U* is the power defined by

$$U^* = \int_B W^* dV - \int_{S_t} t_i u_i dA \tag{11}$$

and B is the volume of the body, S_t is the boundary where traction is given, dV and dA are the infinitesimal volume and area, respectively. From the standpoint of equation (10), C* can be interpreted as the power release rate as the crack advances in the material.

The C* can be determined approximately by the experiments in the manner given by Landes and Begley[12].

2.1.2 The $\hat{J}$-Integral and Its Rate Form

The $\hat{J}$-integral proposed by Kishimoto et al.[14] can also be applied to the time-dependent deformation as well as to the time-independent deformation, since no constitutive relations were used in the formulation. It can also be used with thermomechanical cycling, temperature gradients and the associated material inhomogeneity. The near field and far field expressions of this integral are given by

$$\hat{J} = -\int_{\Gamma_\varepsilon} t_i u_{i,1} dx_1 \tag{12}$$

$$= -\int_{\Gamma} t_i u_{i,1} dx_1 + \int_A \sigma_{ij} \varepsilon_{ij,1} dA \tag{13}$$

where the notation $\lim \varepsilon \to 0$ in the near field expression was omitted intentionally. This notational scheme was also used for other integrals. In the cases where the area of integration includes the boundary of dissimilar materials (a case of material inhomgeneity where the properties change discontinuously), a line integral with integrand $[t_i u_{i,1}]$, where the bracket implies the jump of the quantity in the bracket across the line of material discontinuity, must be added to the right side of equation (13). This integral is carried out along the line of material discontinuity. However, if the interface is parallel to the crack, this additional term vanishes.

This integral implies that the work done to the crack tip by the surrounding medium is independent of the crack length.

This integral was examined as a possible parameter for crack growth prediction in the time-independent regime[1] and some positive results were obtained for isothermal cyclic loading.

The rate form of this integral was proposed by Liu and Hsu[15] without reference to Kishimoto et al.[14]. For a self-similar crack growth in the x_1 direction, the rate form is obtained by simply

replacing the strain and displacements by their time rates

$$\dot{\hat{J}} = -\int_{\Gamma_\varepsilon} t_i \dot{u}_{i,1} dx_1 \tag{14}$$

$$= -\int_{\Gamma} t_i \dot{u}_{i,1} dx_1 + \int_A \sigma_{ij} \dot{\varepsilon}_{ij,1} dA \tag{15}$$

This rate integral is again applicable to all loading and temperature conditions. It is noted that the notation C_g^* used by Liu and Hsu[15] was replaced by $\hat{J}$ to elucidate its relationship to $\hat{J}$. Notice that $\hat{J}$ is not $d\hat{J}/dt$. Liu and Hsu[15] showed some examples of creep crack growth prediction using this integral.

For the steady state creep condition given by equation (3), the following relation can be easily obtained in the manner given in Appendix A of Kim and Orange[2]:

$$\dot{\hat{J}} = h(n) C^* \tag{16}$$

where h is a function of the hardening exponent only. This relation indicates that $\dot{\hat{J}}$ and C^* have equivalent crack growth predictive capability at steady state creep conditions, since they are related only through a multiplicative constant for a given material.

2.1.3 The J*-Integral and Its Rate Form

Another path-independent integral which does not require constitutive restrictions is the J*-integral[13]. This integral was discussed in the previous review[2] for elastic-plastic deformation. The near field and far field expressions of this integral are given by

$$J^* = \int_{\Gamma_\varepsilon} (1/2\sigma_{ij} u_{i,j} dx_2 - t_i u_{i,1} ds) \tag{17}$$

$$= \int_{\Gamma} (1/2\sigma_{ij} u_{i,j} dx_2 - t_i u_{i,1} ds) + \int_A (1/2\sigma_{ij} u_{i,j1} - 1/2\sigma_{ij,1} u_{i,j})\, dA \tag{18}$$

This integral does not carry a physical meaning unless the deformation is elastic or thermoelastic as discussed in Kim and Orange[2].

The rate form of this integral is defined by replacing the displacements and the strains by their rates, i.e.,

$$\dot{J}^* = \int_{\Gamma_\varepsilon} (1/2\sigma_{ij} \dot{u}_{i,j} dx_2 - t_i \dot{u}_{i,1} ds) \tag{19}$$

$$= \int_{\Gamma} (1/2\sigma_{ij} \dot{u}_{i,j} dx_2 - t_i \dot{u}_{i,1} ds) + \int_A (1/2\sigma_{ij} \dot{u}_{i,j1} - 1/2\sigma_{ij,1} \dot{u}_{i,j})\, dA \tag{20}$$

It is noted that $\dot{J}^*$ does not imply dJ^*/dt. The passage from equation (19) to equation (20) makes use of the equilibrium equation and the divergence theorem, hence this rate integral may be utilized

regardless of constitutive relations, loading, and temperature conditions. This rate integral was never proposed, but it will be considered in this study because other non-rate integrals being considered in this program have their corresponding rate integrals.

For deformation conditions of the type of equation (3), direct substitution of equations (4) and (5) furnishes the relation between J* and C* (Appendix A of[2]);

$$\dot{J}^* = g(n)C^* \tag{21}$$

The function g(n) is again constant if a material is given, thus it is expected that $\dot{J}^*$ can predict the creep crack growth as well as C* when deformation is dominantly of the steady-state type.

The integrands of the second terms of the equations (18) and (20) have singularities of r^{-2} at the crack tip. The existence of these terms necessitates a special angular distribution of field quantities around the crack tip. This was described by Kim and Orange[2].

2.1.4 The ΔT-Integrals

Atluri, Nishioka and Nakagaki[16] proposed the following two integrals for elastic-plastic materials:

$$\Delta Tp^* = \int_{\Gamma_\varepsilon} |n_1 \Delta W - (t_i + \Delta t_i)\Delta u_{i,1} - \Delta t_i u_{i,1}| ds \tag{22.a}$$

$$= \int_{\Gamma} |n_1 \Delta W - (t_i + \Delta t_i)\Delta u_{i,1} - \Delta t_i u_{i,1}| ds + \int_A |\Delta\sigma_{ij}(\varepsilon_{ij,1} + 1/2\Delta\varepsilon_{ij,1}) - \Delta\varepsilon_{ij}(\sigma_{ij,1} + 1/2\Delta\sigma_{ij,1})| dA \tag{22.b}$$

$$\Delta Tp = \int_{\Gamma_\varepsilon} |n_1 \Delta W - (t_i + \Delta t_i)\Delta u_{i,1} - \Delta t_i u_{i,1}| ds \tag{23.a}$$

$$= \int_{\Gamma} |n_1 \Delta W - (t_i + \Delta t_i)\Delta u_{i,1} - \Delta t_i u_{i,1}| ds - \int_A |\Delta\sigma_{ij}(\varepsilon_{ij,1} + 1/2\Delta\varepsilon_{ij,1}) - \Delta\varepsilon_{ij}(\sigma_{ij,1} + 1/2\Delta\sigma_{ij,1})| dA \tag{23.b}$$

where

$$\Delta W = \sigma_{ij}\Delta\varepsilon_{ij} + \Delta V \tag{24}$$

$$\Delta V = 1/2\Delta\sigma_{ij}\Delta\varepsilon_{ij} \tag{25}$$

The incremental potential ΔV must satisfy the following condition for the two integrals to have physical meanings:

$$\Delta\sigma_{ij} = \partial\Delta V/\partial\Delta\varepsilon_{ij} \tag{26}$$

Such an incremental potential exists for isothermal proportional elastic-plastic deformation, however it is not possible to find one if the deformation condition includes nonproportional plasticity, time-dependency, nonuniform temperature distribution and thermomechanical loading. The path-independence of these integrals, however, does not require the existence of the incremental

potential. With equations (24) and (25), one can easily see that the passage from equation (22.a) to (22.b) and the passage from equation (23.a) to (23.b) utilize only the equilibrium equation and the divergence theorem, but not equation (25). Therefore, these integrals should be applicable to time-dependent deformation, thermomechanical cyclic loading and thermal gradient cases.

The area integral in the ΔTp^*-integral exhibits a r^{-2} type singular behavior; thus the angular distribution of the stresses and strains must satisfy the condition that the angular integral vanish near the crack tip when the integral is written in terms of polar coordinates.

The physical meaning for the time-dependent deformation exists only in the situation where the total deformation can be approximated by the steady-state creep deformation. In this case, these integrals represent the rate of the incremental potential per unit difference in crack length. As was discussed in[2], the ΔTp^*-integral is a direct measure of the crack tip deformation , but the ΔTp-integral is not. For this reason, a recent paper by Brust and Atluri[17] considers only the ΔTp^*-integral for creep deformation. In this paper[17], they take the time rate by dividing the ΔTp^*-integral by time increment and taking the limit. The second order terms of the incremental quantities were dropped and the equation becomes

$$\dot{T}p^* = \int_{\Gamma_\varepsilon} (n_1 \dot{W} - n_j \sigma_{ji} \dot{u}_{i,1}) ds \tag{27.a}$$

$$= \int_{\Gamma} (n_1 \dot{W} - n_j \sigma_{ji} \dot{u}_{i,1} - n_j \dot{\sigma}_{ji} u_{i,1}) ds + \int_A (\dot{\sigma}_{ij} u_{i,j1} - \sigma_{ij,1} \dot{u}_{i,j}) dA \tag{27.b}$$

It is noted that Brust and Atluri[17] denotes this integral " $\dot{T}^*$" instead of " $\dot{T}p^*$". We use here the latter for notational consistency with the incremental integrals.

The relation of this parameter to the crack tip stress and strain field for steady-state creeping solids of the power-law type can be expressed as

$$\sigma_{ij} = (\dot{T}p^*/\alpha I^*)^{1/(n+1)} r^{-1/(n+1)} \tilde{\sigma}_{ij}(\theta) \tag{28}$$

where

$$I^* = I_n + 1/(n+1) \int_{-\pi}^{\pi} [\tilde{\sigma}_{eq}(\theta)]^{(n+1)} \cos\theta d\theta \tag{29}$$

This parameter can also be related to the stress and strain field of a growing crack following Hui and Riedel[20] for the elastic-creeping solids. However, these kinds of relations, including the above equations, can also be established for $\dot{J}^*$ and $\dot{\hat{J}}$ as described previously for a steady-state creep case. Other than these relations to the crack tip field it is not clear what physical meaning Tp*given by equation (27) carries. The ΔTp^* integral as given by equation (22) is related to the energy release rate for the constitutive relationship given by equation (26). The Tp^* integral does not contain the incremental potential, thus the physical significance becomes ambiguous.

Brust and Atluri[17] reported numerical examples for a single edge notch specimen subject to constant stress and constant velocity on the remote boundary.

2.2 Computation of Path-Independent Integrals

The details of the computation of non-rate P-I integrals have been described in the final report of the base program[1]. In computation of the rate integrals, the rate quantities in the integrand were

computed by dividing the differences of the quantities by the creep time between two relevant load cases. The average values between the two load cases were taken for the non-rate quantities. Therefore, the resulting values of the rate P-I integrals represent those at the half of the creep time associated. Software developed in the base program for computation of the non-rate P-I integrals was revised to accommodate the subroutines for computing the rate integral.

The verification of the code was made by considering three example boundary and temperature conditions on the single edge notch specimen model (Figure 4) used in the base program; (1) uniform strain of 1% on the upper boundary at 649°C, (2) uniform stress of 345 MPa on the upper boundary at 649°C and (3) uniform stress of 345 MPa on the boundary and a linear temperature gradient from 649°C on the front face to 538°C on the back face. An example of the load cases and creep times is shown in Figure 9 for the constant strain case. The integrals were computed at times (t) of 0.1, 1.0, 10.0, and 100.0 hours. The rate quantities were computed by dividing their increments between two adjacent load cases by the creep time. The average values of the two load case data were used for the non-rate quantities. The crack was a stationary crack with the length of 2.54mm (a/W = 0.25). The Alloy 718 stress-strain curves determined in the base program [1] were used in the analysis. The creep properties obtained in the base program were not analyzed at the time of this verification, so the creep properties of a similar material were used according to the following five-term power-law creep equation:

$$\varepsilon_c = K(\sigma/\sigma_o)^n t^m + q(\sigma/\sigma_o)^r t \qquad (30)$$

The constants for equation 30 are:

Temperature, °C	K	n	m	q	r
538	1.53×10^{-4}	2.037	0.200	3.400×10^{-9}	20.1
649	2.27×10^{-4}	0.574	0.563	2.325×10^{-4}	9.73

The numerical results showed that these integrals are indeed path-independent for all three problems. Typical examples are shown in Figures 10 and 11 for $\hat{J}$ and $\hat{J}$. The C* integral was path-dependent at small times but it became nearly path-independent at large times (Figure 12). Notice also that all these integrals diminish to zero under constant strain as time becomes large. This is not expected to occur for a growing crack. Figure 13 shows the redistribution of the crack ligament stress with time for a constant strain condition.

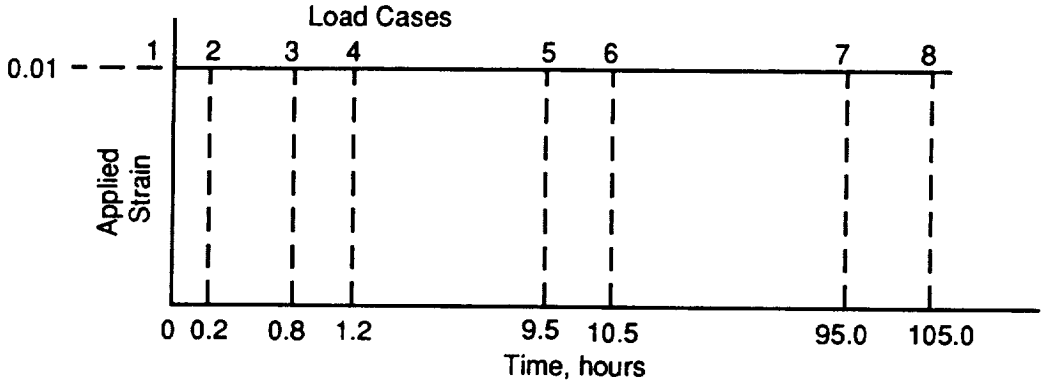

Figure 9. Load cases and creep times for constant strain analysis of rate integrals.

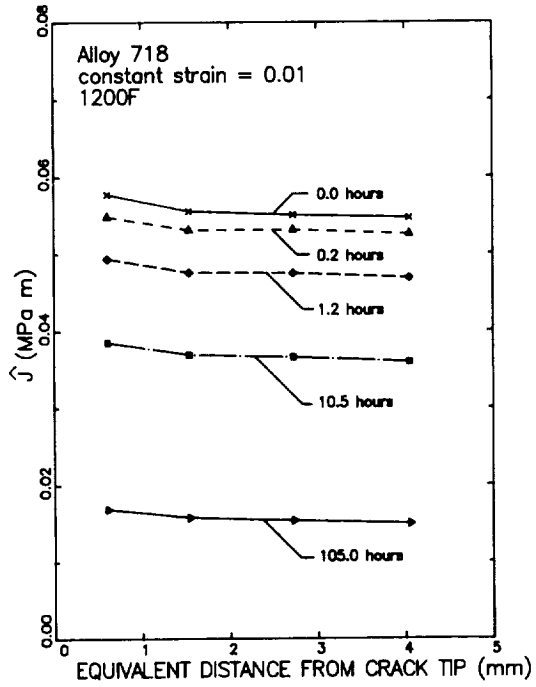

Figure 10. Variation of $\hat{J}$ with path (ε=0.01).

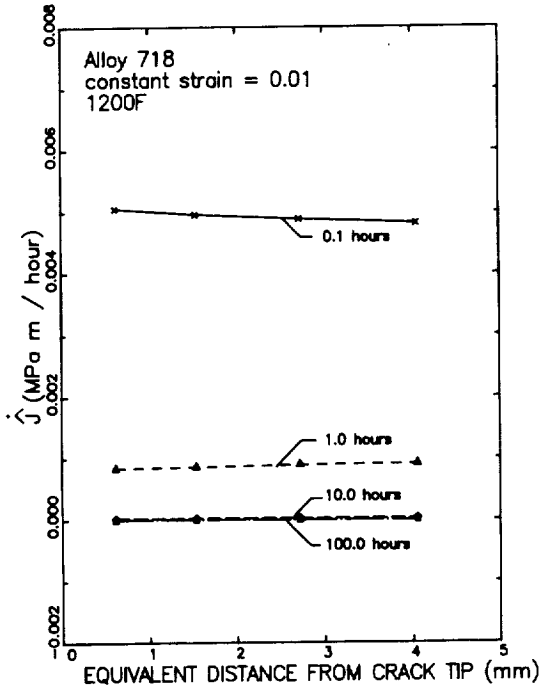

Figure 11. Variation of $\dot{\hat{J}}$ with path (ε=0.01).

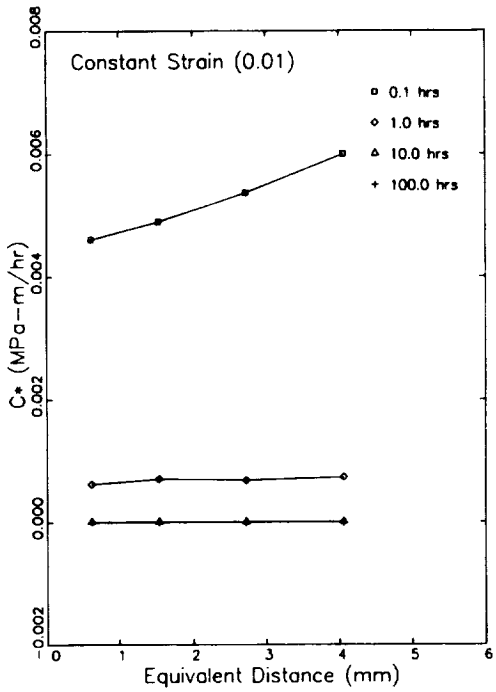

Figure 12. Variation of C* with path (ε=0.01).

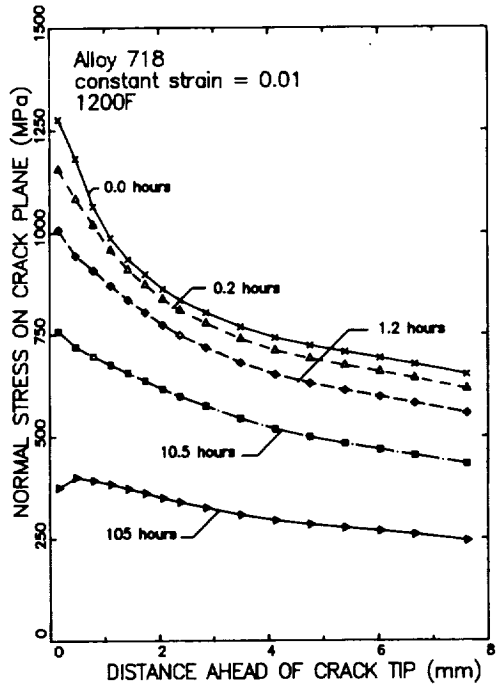

Figure 13. Relaxation of the normal stress ahead of the crack tip (ε=0.01).

2.3 Conclusions

The review of the path-independent integrals for time-dependent deformation leads to the following conclusions:

- The C*-integral can be applied only when the secondary creep deformation is dominant in the body.

- The non-rate path-independent integrals (J^*, $\hat{J}$, ΔTp^* and ΔTp) selected in the base program for further evaluation are also path-independent for inelastic time-dependent deformation including unloading and nonproportional loading.

- The rate integrals ($\dot{J}^*$, $\dot{\hat{J}}$, and $\dot{T}p^*$) are path-independent for inelastic time-dependent deformation including unloading and nonproportional loading.

- The non-rate integrals (J^*, $\hat{J}$, ΔTp^* and ΔTp) and the rate integrals ($\dot{J}^*$, $\dot{\hat{J}}$, and $\dot{T}p^*$) are applicable to time-dependent deformation with spatial and temporal temperature variation. The material may be inhomogeneous. However, the mechanical field variables must have some degree of smoothness to avoid additional terms including jump discontinuities.

3.0. Crack Growth Under Thermomechanical Loading and Temperature Gradients

The objective of this task was to investigate the ability of the P-I integrals to correlate the crack growth data under thermomechanical loading and temperature gradient conditions. The experimental data for these loading conditions were reported in Sections 8 and 9 of the base program report[1].

3.1 Finite Element Analysis of Crack Growth

The strain in the cracked body during a thermomechanical cycle can be decomposed into the mechanical strain and thermal strain. The thermal strain is uniform throughout the body at a fixed time point in a cycle, thus it does not contribute to the stress field. Furthermore, the thermal strain is not singular at the crack tip, and therefore its contribution to the P-I integrals vanishes. This implies that the finite element analysis can be performed with boundary conditions due to the mechanical part only. However, the thermal strain must be included in the thermal gradient analysis because the thermal gradient produces a singular thermal stress field around the crack tip.

The finite element analysis for TMF crack growth was performed in a manner similar to the isothermal analysis in the base program[1]. The maximum strain is applied on the model in the first load case, two nodes at the crack tip are released in the second load case, and the minimum strain is applied on the boundary in the third load case. The temperature of the model changes from the maximum (minimum) value at the maximum strain to the minimum (maximum) value at the minimum strain for the in-phase (out-of-phase) cycle. This cycle of analysis is repeated until the crack length increases to a fourth (2.54mm) of the width of the specimen. The variation of the crack length and control strain with the load cases in the analysis is shown schematically in Figure 14. The total load cases are 22.

The crack growth analysis under temperature gradients and mechanical strain cycling were performed in a manner similar to the isothermal strain cycling analysis. The temperature gradient shown in Figure 15 is applied to the model, and this distribution of temperature remains unchanged during strain cycling.

3.2 Results of Analysis

The specimens and test conditions analyzed in this study are:

TMF:

1. Specimen N5-43 (427°C – 649°C in-phase, $\Delta\varepsilon$=0.5%)
2. Specimen N4-36 (538°C – 649°C out-of-phase, $\Delta\varepsilon$=0.75%)
3. Specimen N5-29 (427°C – 649°C in-phase, $\Delta\varepsilon$=1.15%)
4. Specimen N5-25 (427°C – 649°C out-of-phase, $\Delta\varepsilon$=1.15%)

Temperature Gradient:

1. Specimen N5-5 (649°C – 482°C, $\Delta\varepsilon$=0.5%)
2. Specimen N4-39 (649°C – 482°C, $\Delta\varepsilon$=1.70%)

All of the TMF and thermal gradient specimens were tested at the same frequency (0.01 Hz) as the isothermal specimens.

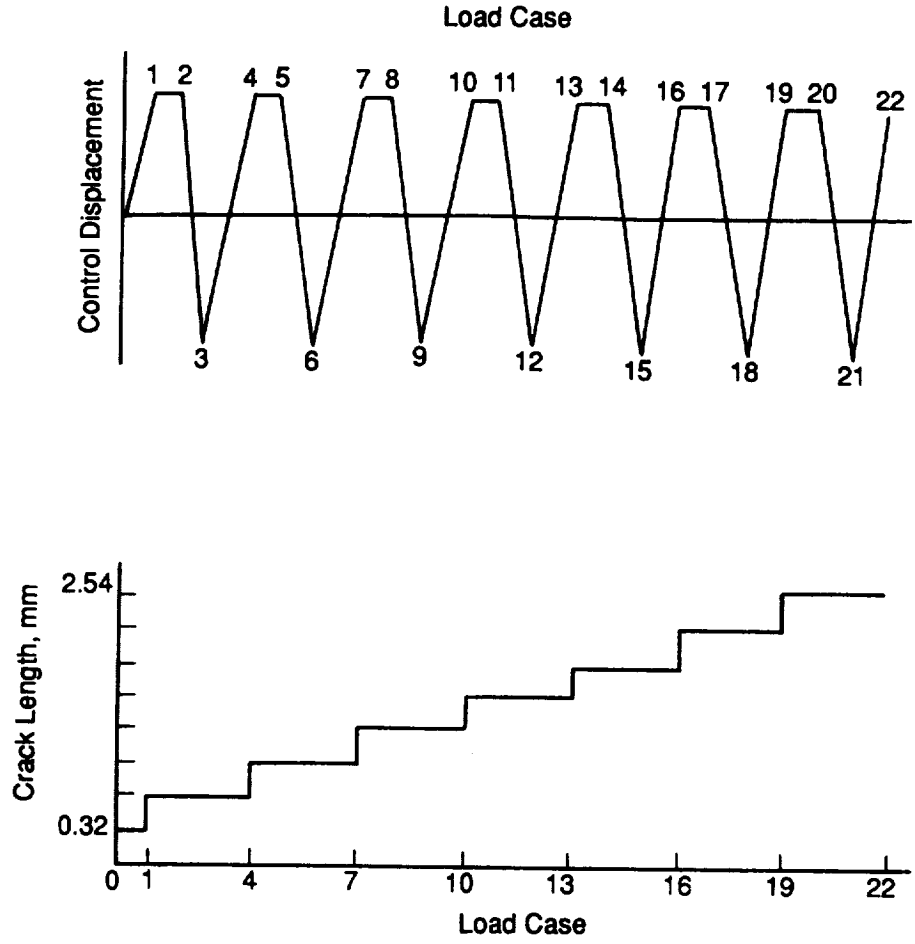

Figure 14. Schematic of loading steps and crack lengths in crack growth simulation without hold time for SEN specimen.

The calculated and experimental average stress during crack propagation are plotted in Figures 16 and 17 for the TMF and temperature gradient test specimens, respectively. The corresponding calculated and experimental CMOD ranges for these specimens are presented in Figures 18 and 19. The degree of correlation varied from specimen to specimen. The average stress data was reasonably good other than specimen N5-43 for which the calculated maximum and minimum stresses were substantially lower in magnitude than the experimental data. The predicted CMOD range was smaller in most cases, and in particular the deviation was fairly large for thermal gradient cases.

The four path-independent integrals used for the isothermal crack growth analysis (J*, $\hat{J}$, Tp* and Tp) were computed for all specimens. The results showed path independence. Typical results are shown in Figure 20 for a TMF cycling and in Figure 21 for temperature gradient crack propagation.

The crack growth rates for the TMF and thermal gradient loading were plotted in Figures 22 through 25 for the four P-I integrals. The 538°C isothermal data are also included in these figures. It appears from Figure 15 that the crack growth rates of the thermal gradient specimens would be close to those of 649°C, because the crack path in the analysis (the maximum crack length = 2.54

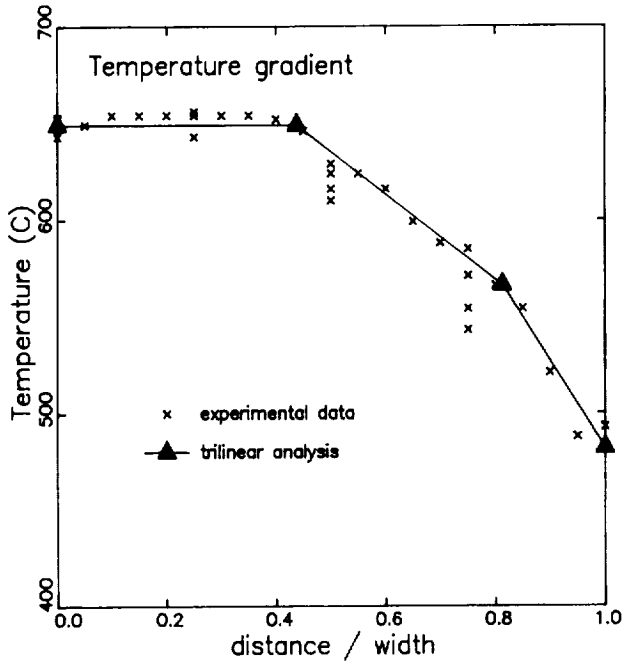

Figure 15. Comparison of trilinear approximation and experimental data in Alloy 718 temperature gradient tests.

mm) is contained within the 649°C region. These crack growth rates are consistent with the isothermal data at 649°C obtained in the base program.

The crack growth rates of the 538°C-649°C 0.75% OP specimen are between the 538°C data and the thermal gradient data, but very close to the 538°C data. The 427°C-649°C TMF data show that the in-phase crack growth rates are greater than the out-of-phase crack growth rates. Unfortunately, the 427°C isothermal data are not available at this time, thus the locations of these TMF data relative to the 427°C isothermal data are unknown. However, it appears that even the in-phase crack growth rates are significantly lower than the 649°C isothermal rates when the data were correlated with ΔJ^*, $\Delta \hat{J}$ or ΔTp^*. This may be due to the fact that the crack paths of thermal gradient specimens were subjected to higher temperatures than those of TMF specimens for the whole cycle except at the maximum strain point. Therefore, it is expected that the time-dependent crack growth and/or the environmental effect becomes more significant for the thermal gradient specimens. This is also manifested in Figure 26 where the crack growth rates of the thermal gradient specimens (which would represent the case of R_ε=-1, 0.6cpm, 649°C) were compared with isothermal crack growth data. In these figures the 538°C data are from the base program, and the R_ε=0, 10cpm data at 593°C and 649°C are from Section 7 of this report. It is apparent that the frequency effect is significant at 649°C even if the influence of R_ε (Figure 88 of[1]) is taken into account. This implies that the time-dependent behavior and/or the environmental effect is significant in crack growth at 649°C. Similar observations can also be found for Alloy 718 at 649°C in Van Stone et al.[22], and in Nicholas and Ashbaugh[23]. Finally, it is noted that the correlation of the TMF and thermal gradient crack growth data with ΔTp, Figure 25, appears somewhat different. While the quality of correlation is

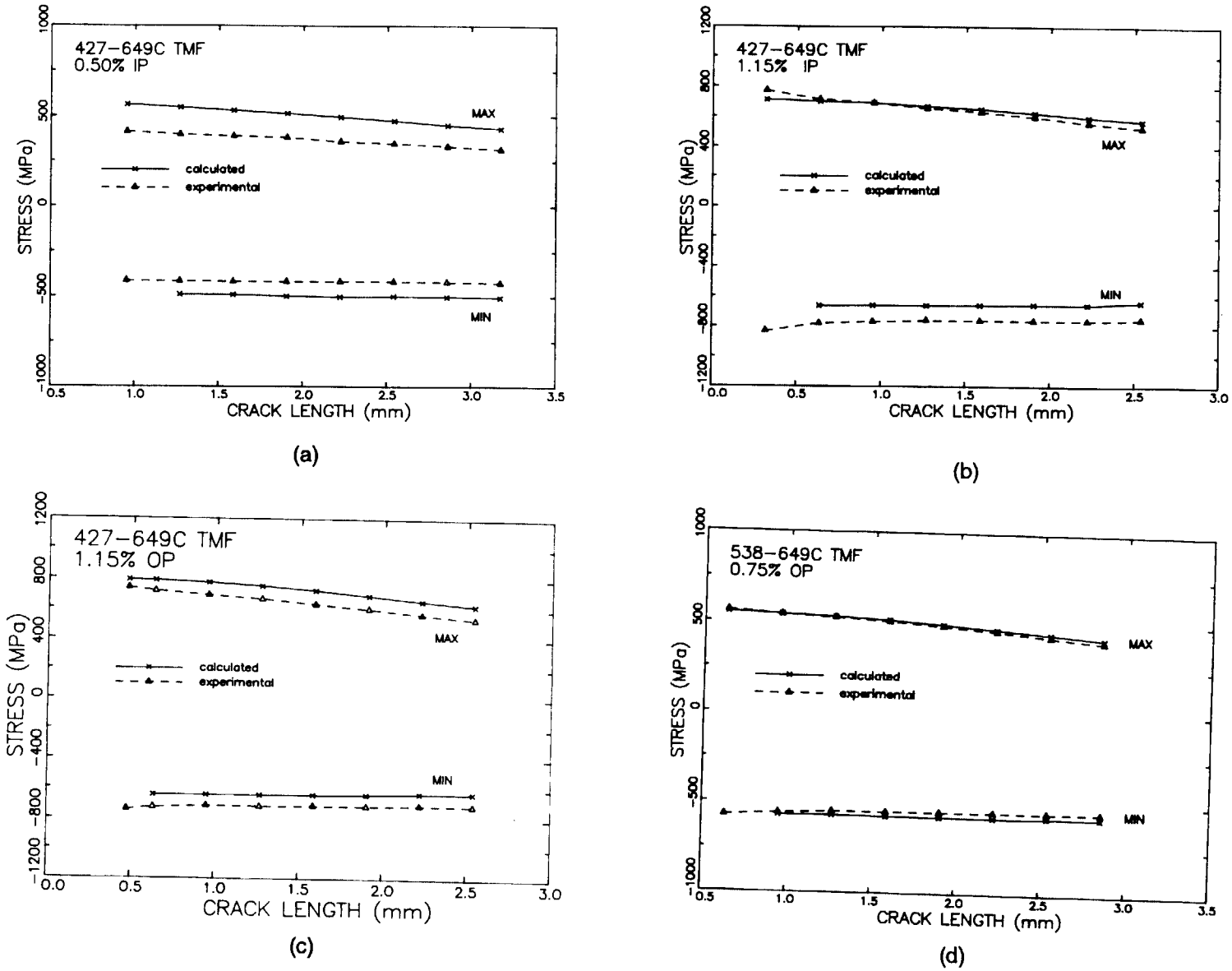

Figure 16. Variation of the average stress with crack length for Alloy 718 TMF specimens (a) N5–43, (b) N5–29, (c) N5–25, and (d) N4–36.

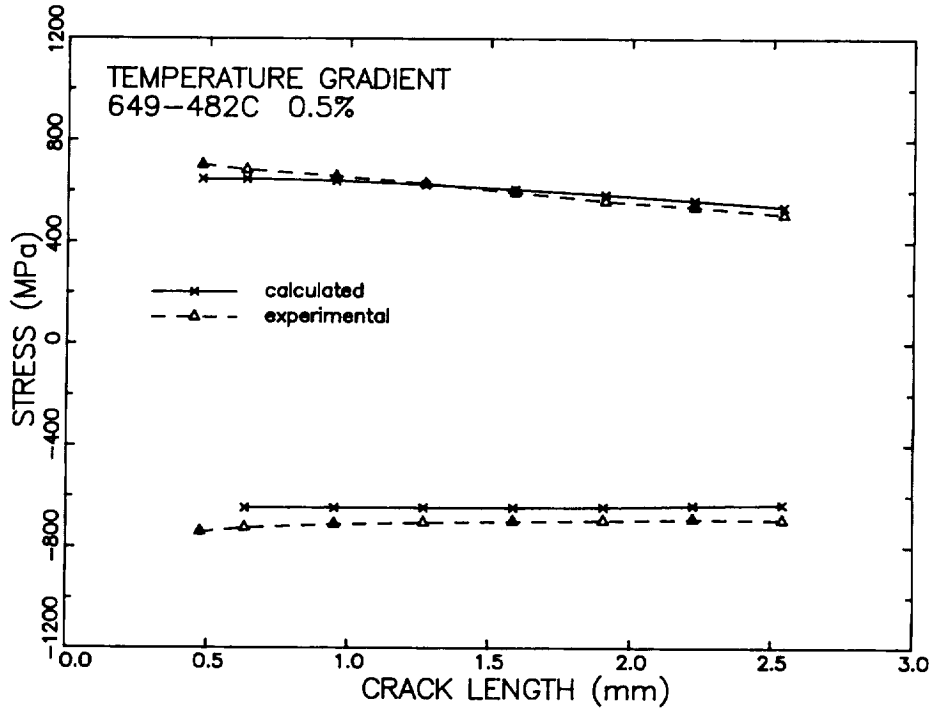

(a)

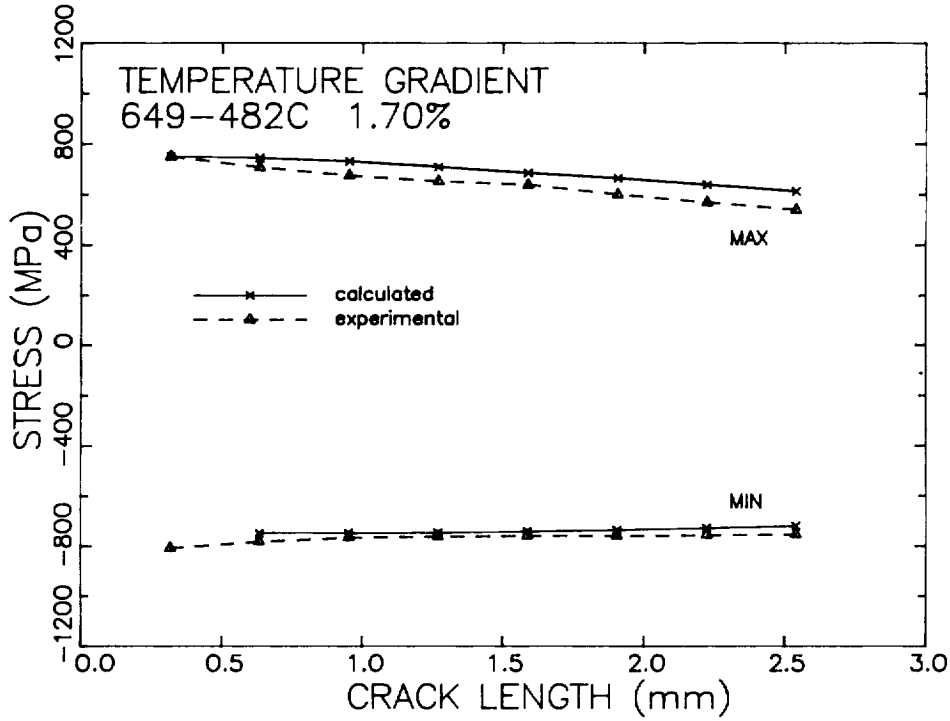

(b)

Figure 17. Variation of the average stress with crack length for Alloy 718 temperature gradient specimens (a) N5–5 and (b) N4–39.

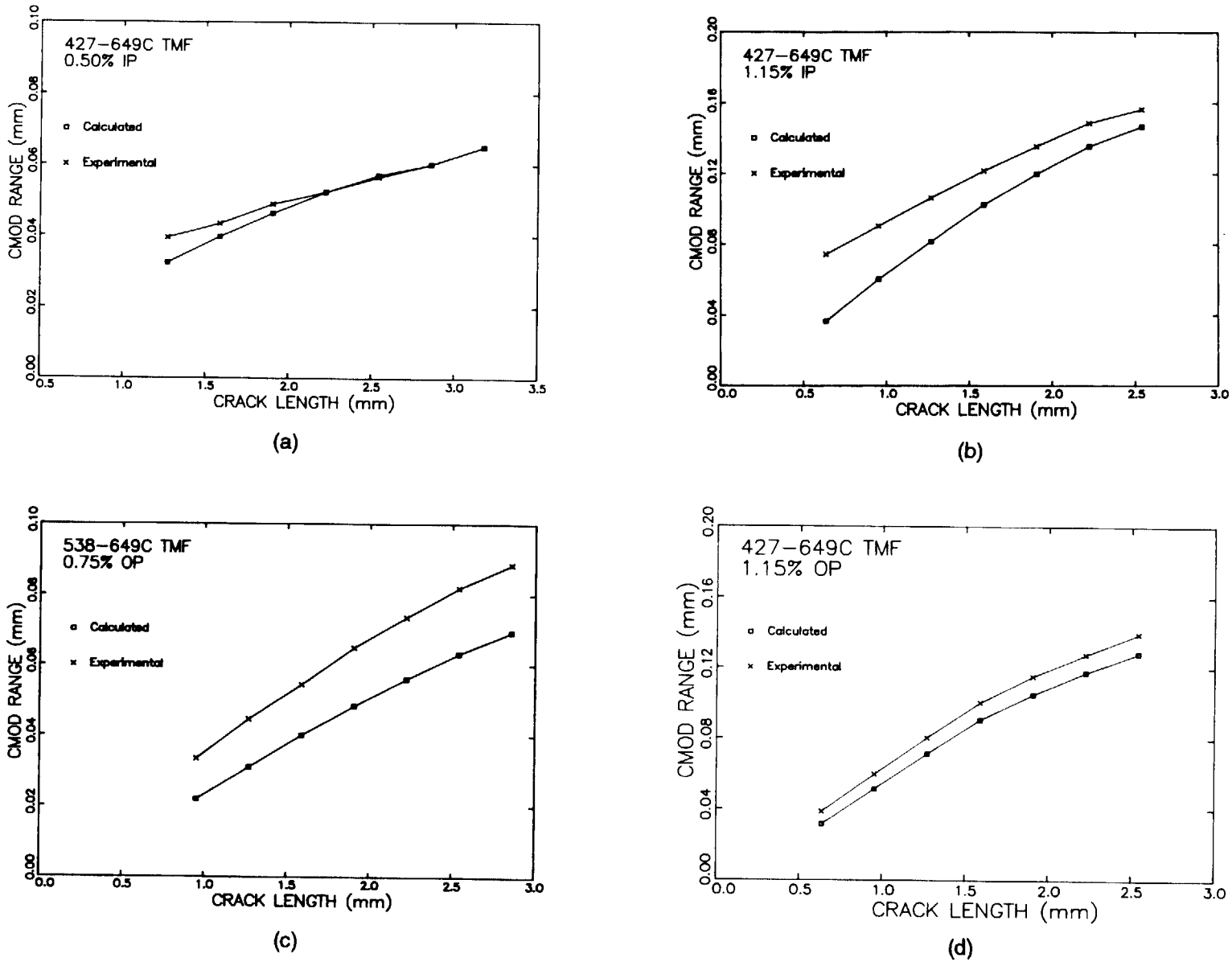

Figure 18. Variation of the CMOD with crack length for Alloy 718 TMF specimens (a) N5–43, (b) N5–29, (c) N5–25, and (d) N4–36.

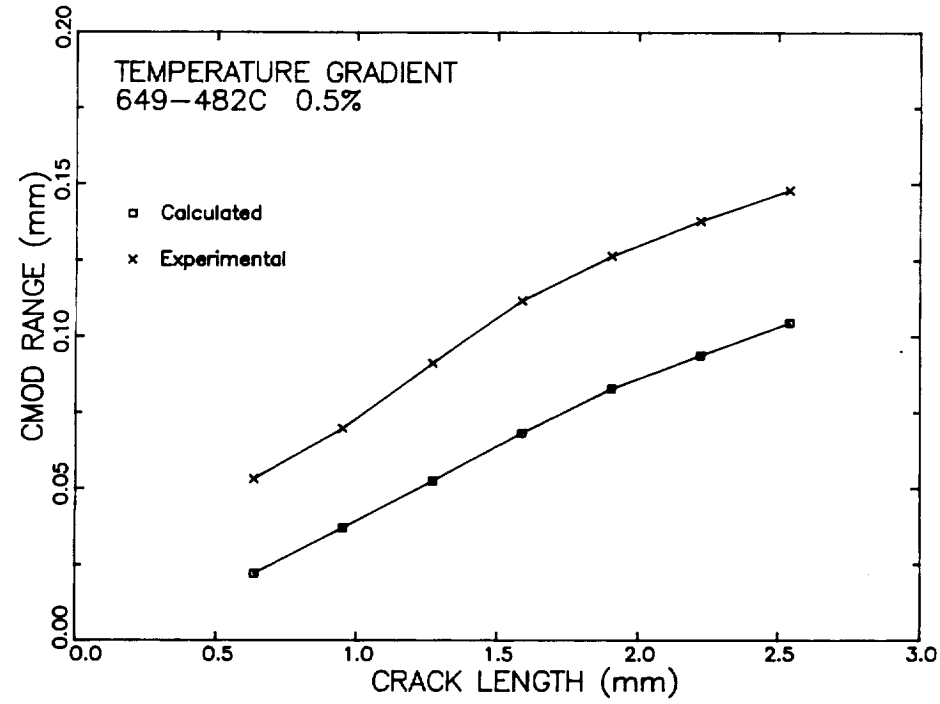

(a)

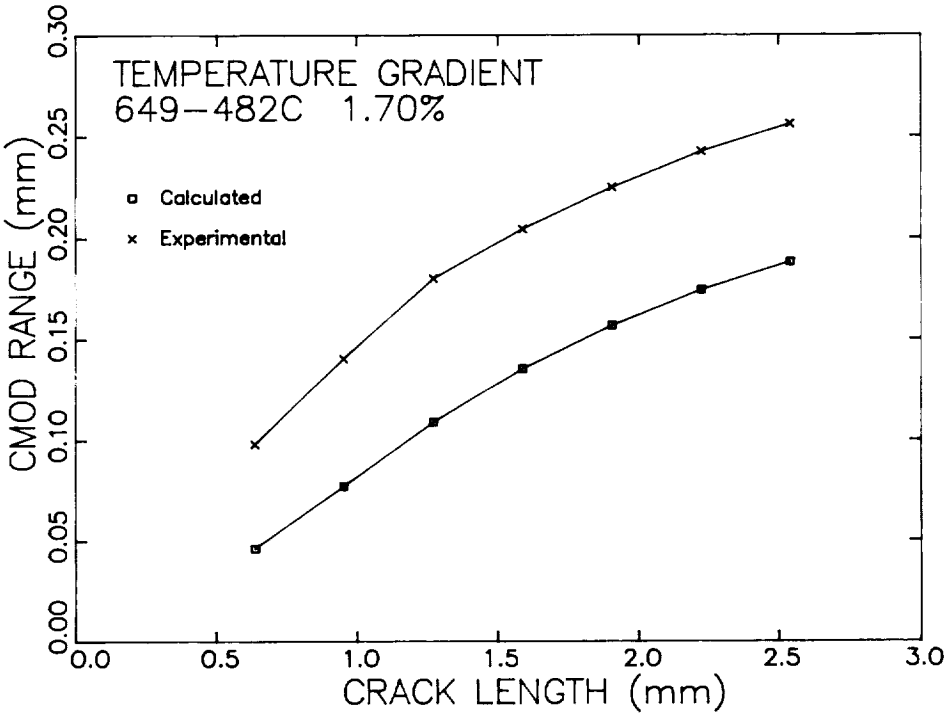

(b)

Figure 19. Variation of the CMOD with crack length for Alloy 718 temperature gradient specimens (a) N5–5 and (b) N4–39.

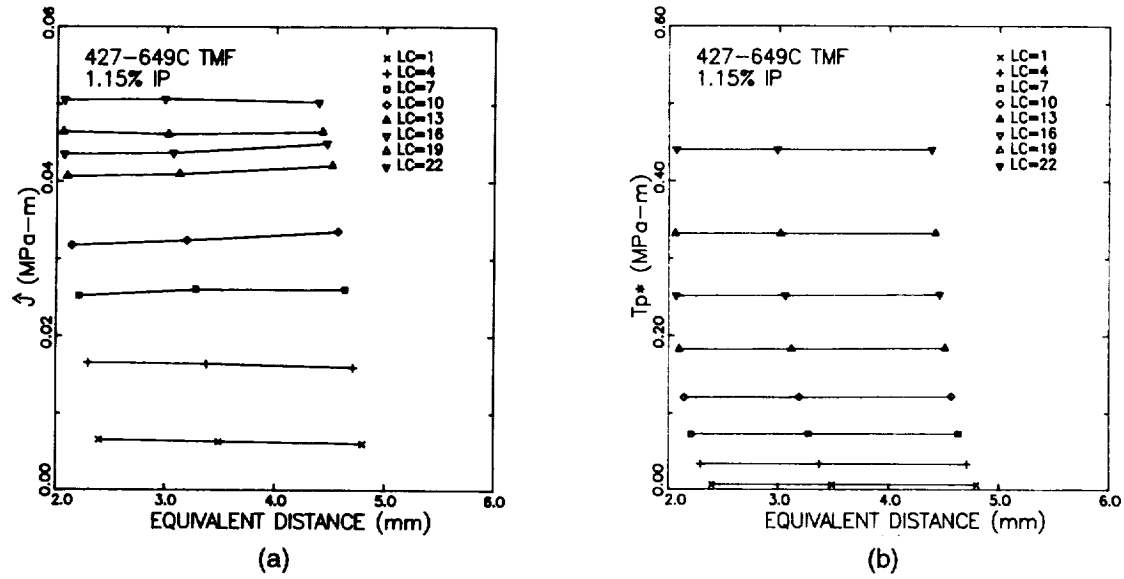

Figure 20. Variation of (a) $\hat{J}$ and (b) Tp* with path for Alloy 718 specimen N5–29.

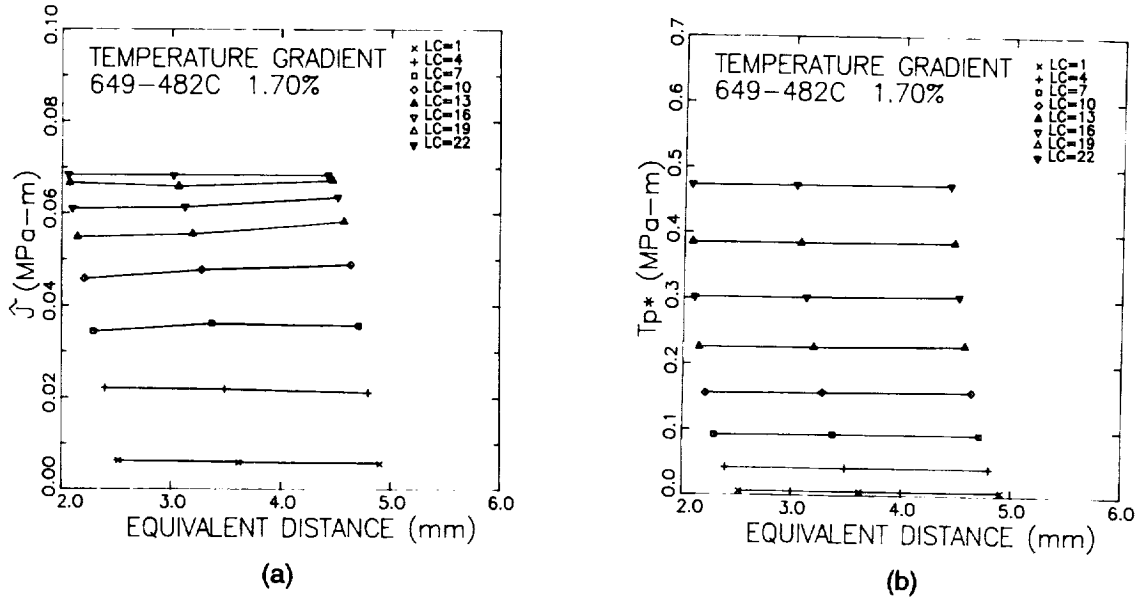

Figure 21. Variation of (a) $\hat{J}$ and (b) Tp* with path for Alloy 718 specimen N4–39.

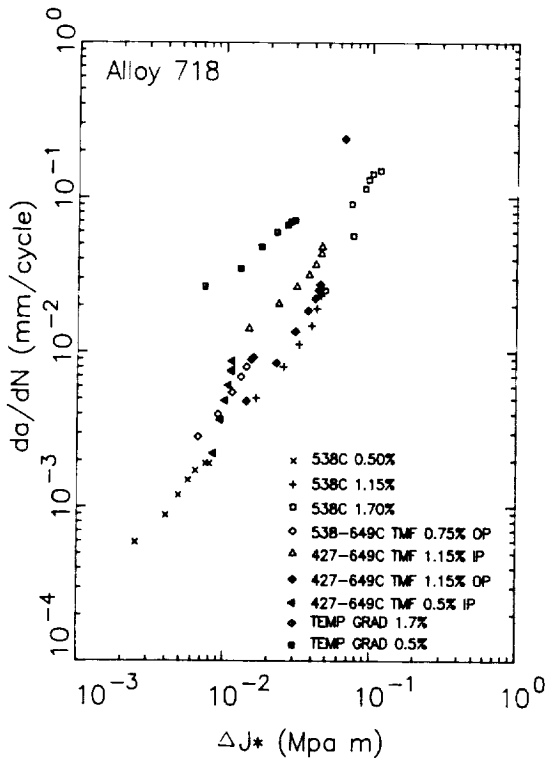

Figure 22. Correlation of Alloy 718 cyclic thermomechanical and temperature gradient crack growth data with ΔJ*.

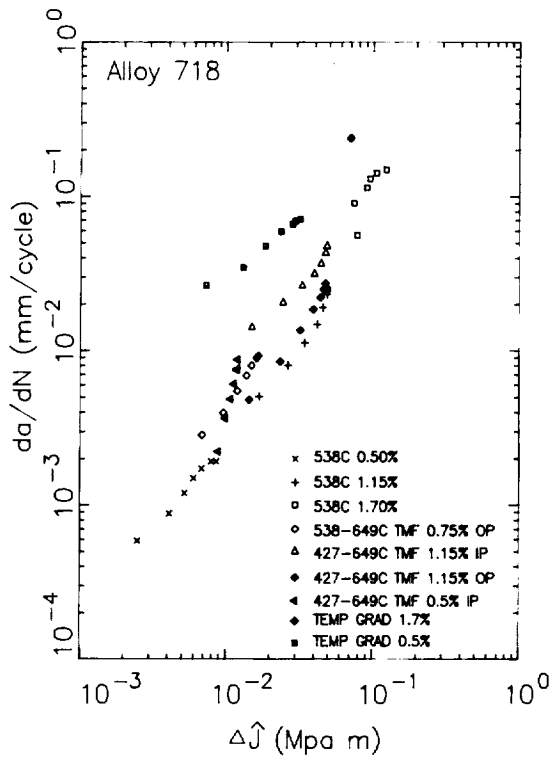

Figure 23. Correlation of Alloy 718 cyclic thermomechanical and temperature gradient crack growth data with ΔĴ.

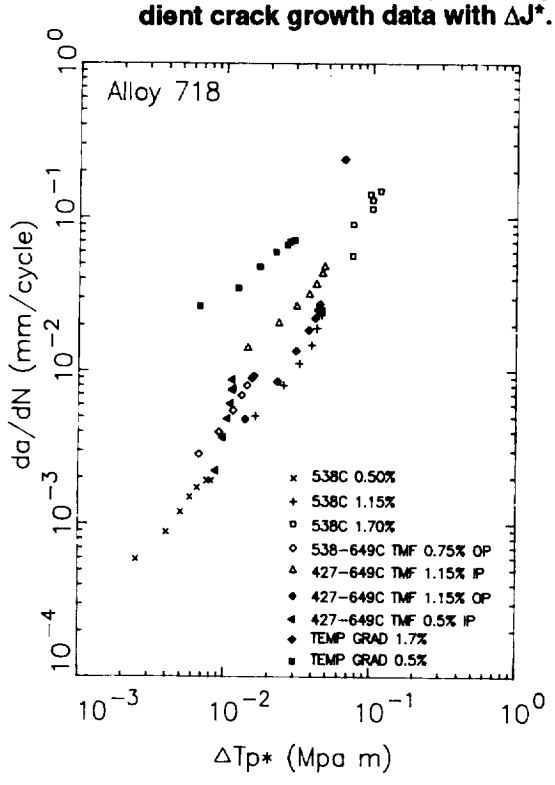

Figure 24. Correlation of Alloy 718 cyclic thermomechanical and temperature gradient crack growth data with ΔTp*.

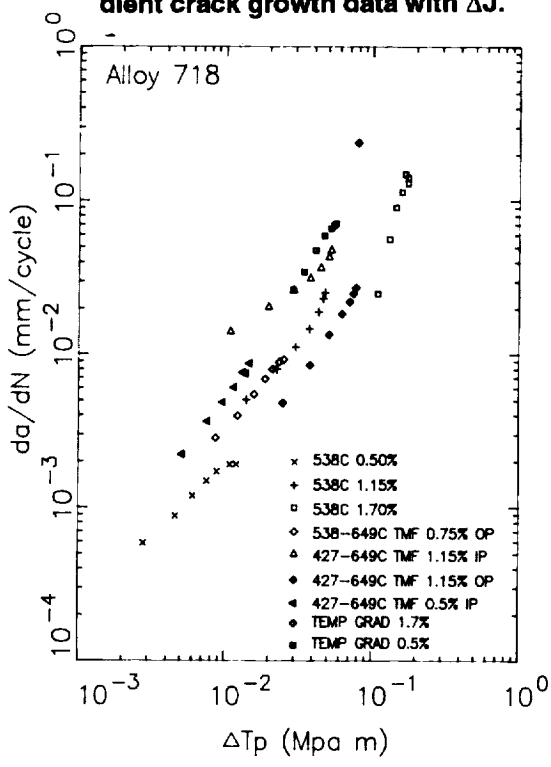

Figure 25. Correlation of Alloy 718 cyclic thermomechanical and temperature gradient crack growth data with ΔTp.

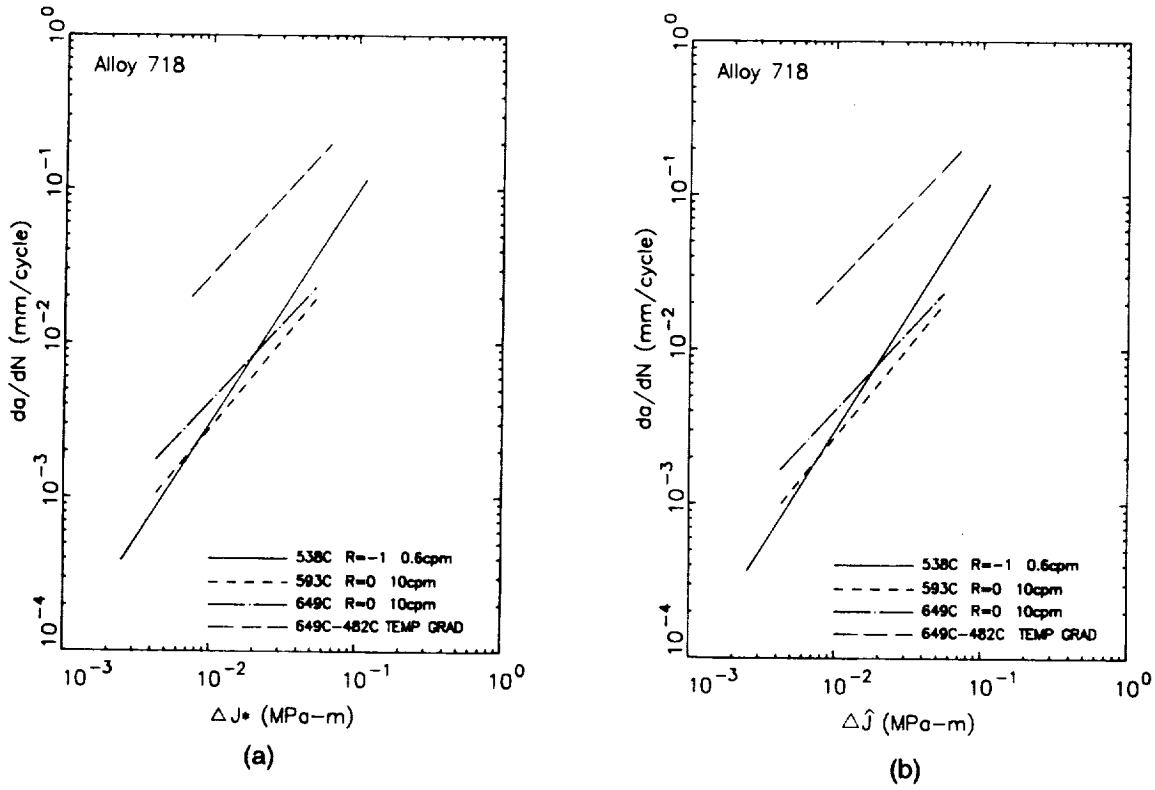

Figure 26. Comparison of temperature effects on the Alloy 718 crack growth data correlation with (a) ΔJ^* and (b) $\Delta \hat{J}$.

seemingly comparable to other parameters, it does not reveal the time-dependency and the environmental effect discussed above. Further investigation is needed to verify this.

3.3 Conclusions

The results of the analyses of four TMF specimens and two thermal gradient specimens were correlated with ΔJ^*, $\Delta \hat{J}$, ΔTp^* and ΔTp. In the analyses of thermal gradient specimens, the crack propagated through the region where the temperature was uniformly 649°C. The crack growth rates of these specimens were consistent with those of the isothermal specimens tested at 649°C[1]. The TMF crack growth data appear to be correlated with these parameters. However, further analysis of isothermal data (427°C, 593°C, 649°C) and TMF data obtained in the base program would be needed for further verification. There is an indication that ΔTp does not represent the time-dependent behavior of crack growth and/or the environmental effect properly. This also requires further verification.

4.0 Crack Growth Analysis on Hastelloy-X

The objective of this task was to analyze the crack growth data obtained by Meyers[3] on Hastelloy-X in a pre-HOST program and investigate whether or not the path-independent integrals selected in the base program correlate the crack growth data. The outcome of this task was the verification of the applicability of these P-I integrals for a geometry and material different from those used in this program.

The specimen used by Meyers[3] had a tubular geometry as shown in Figure 27. This specimen was subjected to various strain cycling under isothermal, TMF, and combinations of cyclic and time dependent deformation. The majority of data were obtained for R_ε=-1 loading. This program performed FEM crack growth simulation of the 13 isothermal and 6 TMF specimens shown in Table 1. All of these cases were for R_ε=-1 without hold time. The TMF analyses included 5 out-of-phase cycles and 1 in-phase cycle. Details on the material, test method, etc. are available in[3],[26], and[27].

4.1 Method of Analysis

The finite element analyses were performed with the assumption of time-independent deformation. The elastic moduli, Poisson ratios, thermal expansion coefficients and cyclic stress-strain curves were needed as input to the finite element analysis. These data were obtained from published sources[3,24,25]. The cyclic stress-strain curves used in these analyses are shown in Figure 28. This

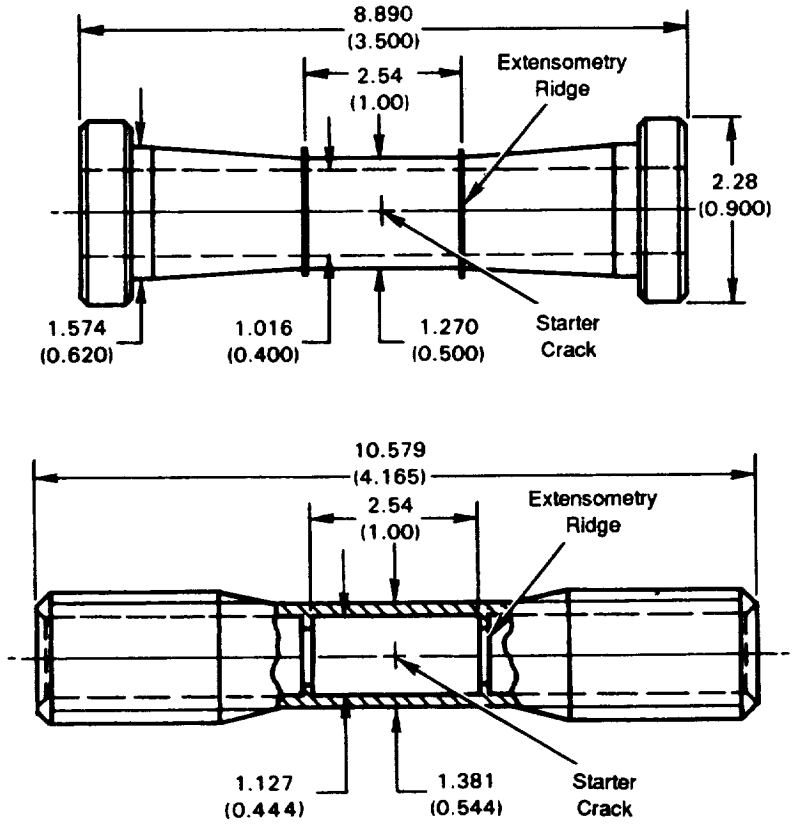

Dimensions are Nominal Values, Given in Centimeters (Inches)

Figure 27. Tubular crack growth test specimen of Hastelloy-X.

Table 1. Hastelloy-X specimens evaluated using FEM crack growth simulation.

Test Number	Temperature, °C	Strain Range, %	Mean Strain, %	Cyclic Rate (cpm)	Additional Description
I-1	427	0.15	-0.25	60.0	
I-2	427	0.40	-0.25	10.0	
I-4	427	0.25	-0.25	10.0	
I-6	649	0.15	+0.25	2.0	
I-7	649	0.40	+0.25	1.0	
I-14	871	0.15	0.0	1.0	
I-15	871	0.175	0.0	1.0	
I-16	871	0.40	0.0	0.5	
I-18	871	0.15	0.0	1.0	
I-19	927	0.25	0.0	1.0	
I-20	927	0.40	0.0	0.5	
I-23	982	0.15	0.0	0.5	
I-25	982	0.40	0.0	0.5	
T-1	427-927	0.15	0.0	0.83	out-of-phase
T-2	427-927	0.25	0.0	0.83	out-of-phase
T-3	427-927	0.40	0.0	0.44	out-of-phase
T-4	427-927	0.25	0.0	0.83	in-phase
T-8	427-871	0.25	0.0	0.83	out-of-phase
T-12	427-871	0.40	0.0	0.44	out-of-phase

material exhibits considerable strain rate sensitivity at temperatures above 649°C and some reverse strain rate sensitivity at lower temperatures[24]. These curves represent the stabilized cyclic stress-strain behavior approximately at the rates of applied strains shown in Table NO TAG. One may observe some variation in the applied strain rates from specimen to specimen. Significant scatter in the stress-strain behavior at the same strain rate may also be found for this material as demonstrated previously[24,25]. Therefore, engineering judgement was exercised to determine the stress-strain curves in Figure 28. It must also be noted that the strain rate varies from location to location within the specimen due to the existence of a crack. The strain rates near the crack tip will be much higher than elsewhere. For an accurate analysis, the rate sensitivity of the stress-strain curves must be accounted for. Unfortunately, this capability did not exist with the classical constitutive theory used in the CYANIDE finite element code employed in this investigation. Thus, the stress-strain curves in Figure 28 were assumed to be applicable everywhere in the specimen.

Another simplification of the problem occurs with the finite element modeling of the specimen. Since the specimen is tubular with a through crack, the model must be three-dimensional to be precise. In this investigation, we will consider an in-plane model generated by expanding the tubular specimen. The width of the in-plane model is equivalent to the circumferential length of the mid-thickness plane of the tube. The length of the model is identical to the gage length. We will take

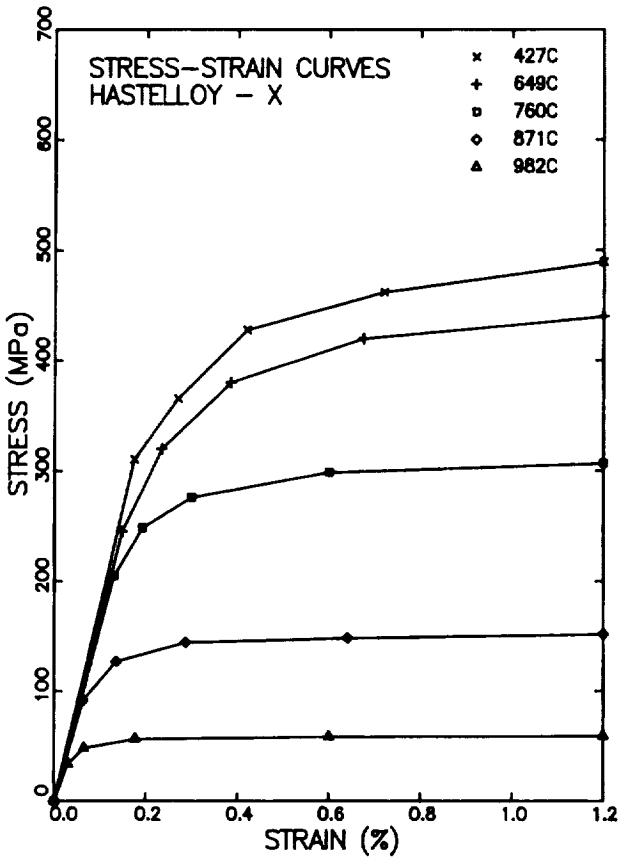

Figure 28. The cyclic stress – strain curves of Hastelloy-X used for finite element analysis of crack growth.

only a quarter of this model for the finite element model considering the symmetry. The finite element model is shown in Figure 29. This model was actually generated by multiplying constant factors on the nodal coordinates of the SEN model used in other tasks (Figure 4), so the two models are identical other than nodal coordinates. This facilitated the application of pre- and post-processors used for analyzing SEN specimens.

The tube specimen is rather short, as with the SEN specimen, to avoid buckling in the compressive part of the applied strain cycle. The distribution of the displacement on the boundary at the gage length would deviate somewhat from uniformity due to the bending effect of the specimen. However, this deviation, and also the unknown lateral boundary conditions at the gage length, would not affect the values of the P-I integrals to a significant extent[1]. The x-directional boundary conditions on the side boundary are not known; however,they must satisfy the conditions that the x-directional displacement must be uniform and that the x-directional resultant force must vanish. An iterative solution scheme may be used to satisfy these conditions, but the effect of the lateral stresses is believed to be insignificant. The final problem, with zero stresses for the unknown boundary conditions, is reduced to a center-cracked plate subjected to uniformly distributed cyclic strain. The errors introduced by the geometric simplification and assumptions of the boundary conditions are conjectured to be rather small from the perspective of the crack driving force and crack growth rate[27,1].

The crack propagation was simulated in a manner similar to the isothermal and thermomechnical crack propagation analysis performed on the SEN specimens. The initial crack tip was located at the third node from the center of the model on the crack plane. The simulation proceeds in three steps in each analysis cycle (representing more than one experimental cycle); (1) the model is loaded to the maximum strain, (2) two nodes are released at the crack tip, (3) the model is reverse loaded to the minimum strain. As in the SEN specimen analyses, the release of two nodes instead of one was used to reduce the computational time. The analysis continues until the crack length reaches a quarter of the plate width, that being the approximate termination point of the test. The total number of cycles is 7. Then the model is reloaded to the maximum strain and the analysis is terminated, so the total number of load cases is 22. This scheme is exactly identical to the case of the SEN specimen shown in Figure 14.

The computation of the P-I integrals were carried out along three rectangular paths used in the crack propagation simulation in the base program[1]. The crack growth rates at the crack lengths

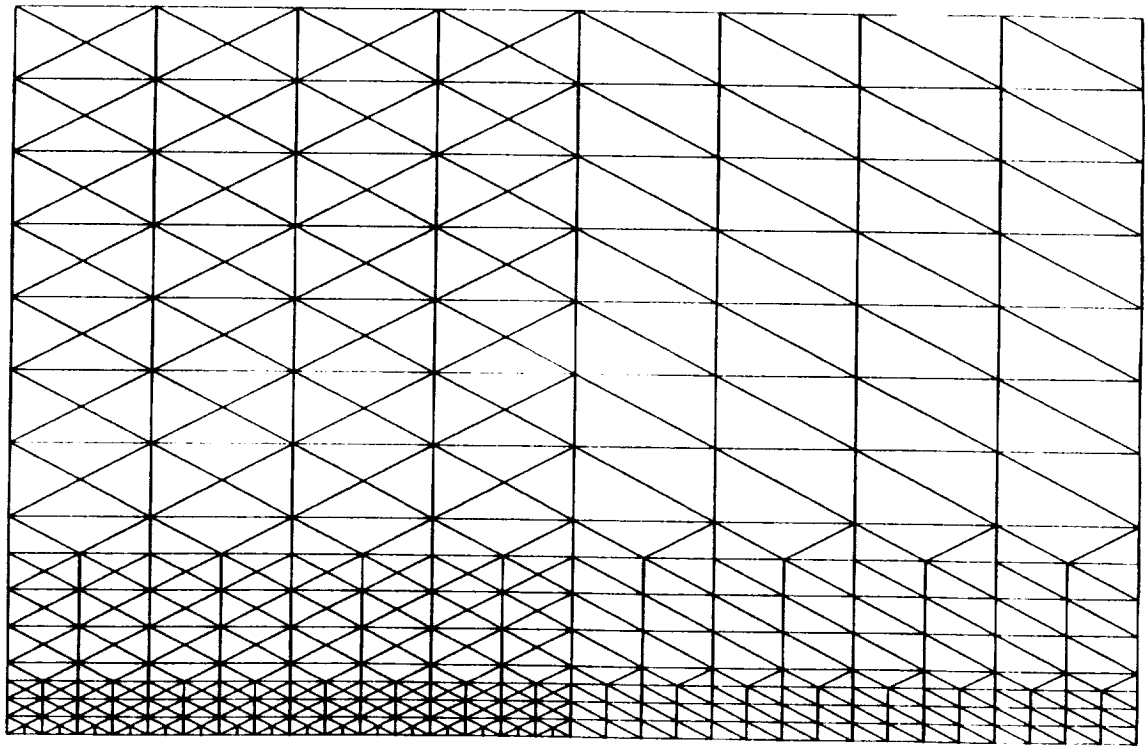

Figure 29. The CCP finite element model of Hastelloy-X.

in the analysis cycles were determined from the da/dN versus K_ε data of Myers[3] by approximating the correlation by linear or bilinear curves. The values of K_ε were determined using formula described elsewhere[28].

4.2 Results of Analysis

The range of the degree of plastic deformation in the specimens subject to various strain and temperature conditions can be found in the contour plots of the effective stress for the extreme cases. Two extreme cases are shown in Figure 30. Figure 30(a) shows the results for a crack at 427°C with a 0.15% strain range where the plastic zone (σ_y=310 MPa) is in the realm of small scale yielding. Figure 30(b) shows the case at 982°C with a 0.4% strain range (σ_y=34 MPa) where the plastic zone covers much of the model (the whole area on the right side of the leftmost contour). Thus, the utility of the P-I integrals to correlate behavior from the LEFM domain to the highly nonlinear domain is being investigated.

The calculated maximum and minimum average stresses (load/cross section area of the uncracked specimen) were plotted in Figure 31 against the crack length at the stain range of 0.4% for the lowest and highest temperatures. The experimental data were not reported in[3], so comparison was not possible. Some decrease of the maximum stress is seen at 427°C but the variation was minimal at 982°C. The minimum stresses stayed nearly constant due to contact of the crack surfaces in compression. The predicted crack profiles at 0.4% are shown in Figure 32 for these two temperatures. Notice the marked difference in the shapes of the profile at larger crack lengths. The opening in the vicinity of the crack tip is much larger at 982°C.

The path-independence of the integrals in the numerical results was achieved to an acceptable degree. Typical examples are shown in Figure 33 for $\hat{J}$ and Tp* at 0.4% for 427°C and 982°C.

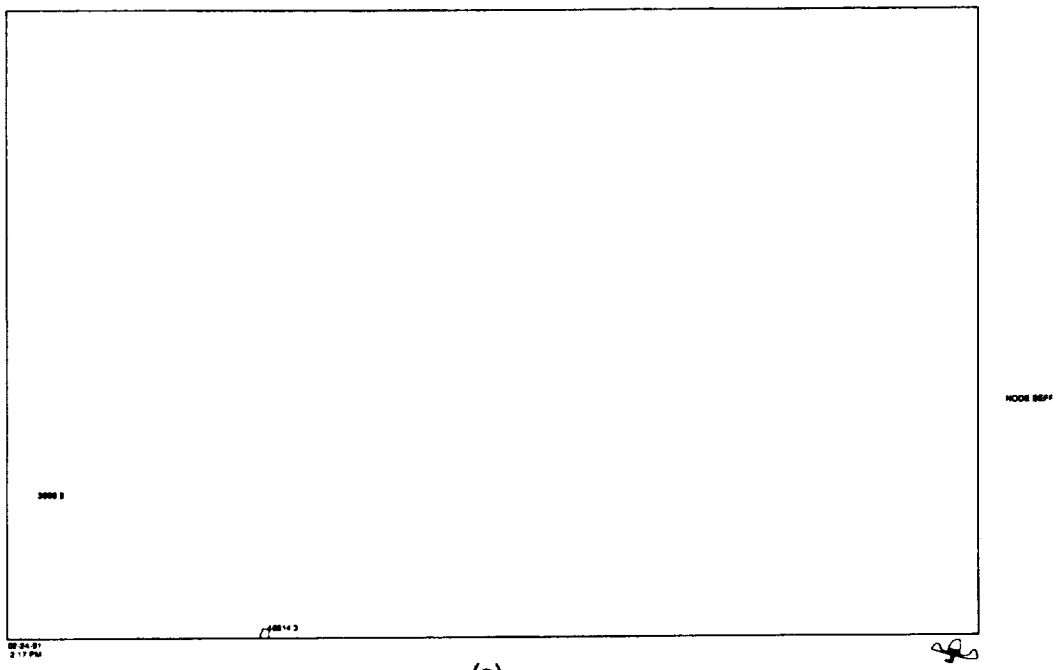

(a)

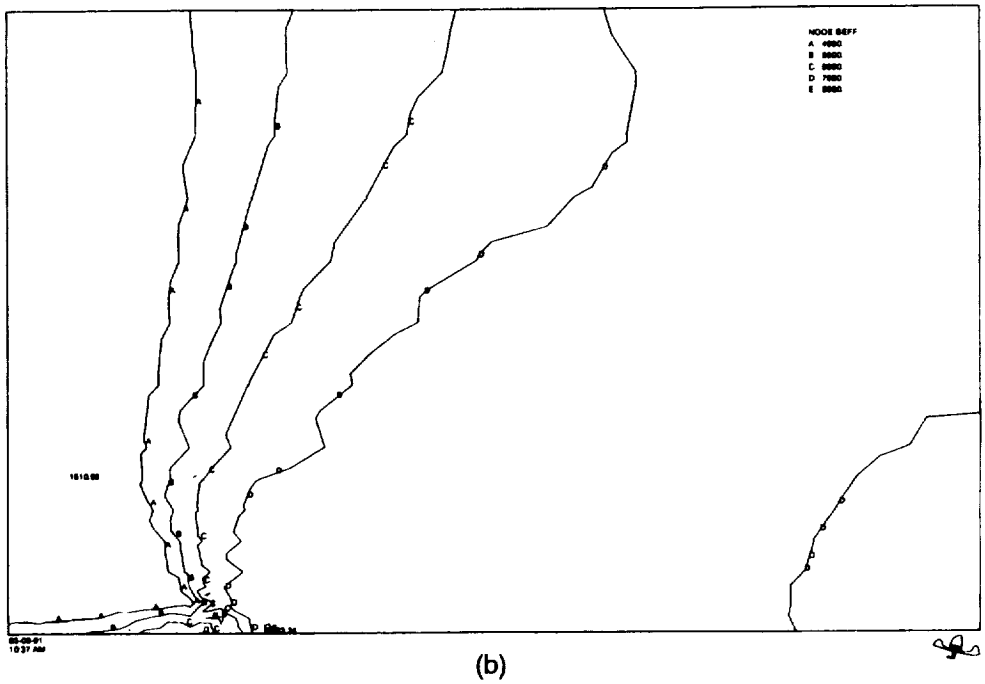

(b)

Figure 30. The predicted plastic zone size in Hastelloy-X at (a) 427°C, $\Delta\varepsilon$=0.15% and a/W=0.25 and (b) 982°C, $\Delta\varepsilon$=0.40% and a/W=0.25.

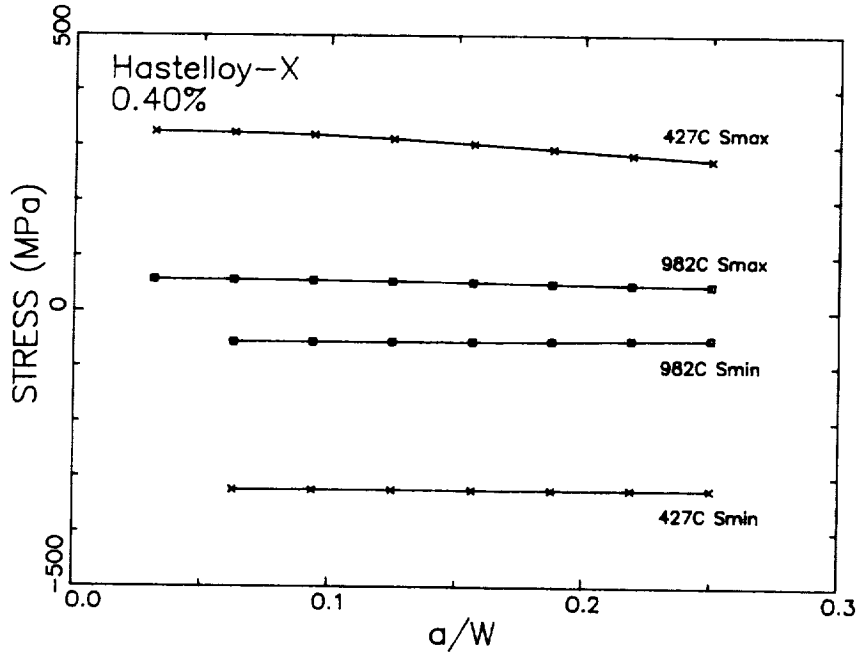

Figure 31. Variation of predicted Hastelloy-X average stress with crack length at various temperatures and $\Delta\varepsilon$=0.40%.

The equivalent distance is the average distance from the crack tip to the nodes on the path of integration.

The correlation of Hastelloy-X crack growth rates with the four P-I integrals (ΔJ^*, $\Delta\hat{J}$, ΔTp^* and ΔTp) at 427°C, 649°C, 871°C, 927°C and 982°C are shown in Figures 34, 35, 36, 37, and 38, respectively. The range was computed from the minimum to the maximum applied strain. This is approximately equivalent to the range from the crack opening point to the maximum strain, since the values of the P-I integrals at the closing point, opening point, and the minimum strain are very small compared with those at maximum strain for R_ε=-1 loading[1]. The data points in the figures were chosen such that they are within or near the bounds of da/dN in the test data, although data points in the analysis were obtained for 7 crack lengths in all cases. Therefore, some of the strain ranges do not have as many data points as others. Another point to note is that the distribution of data points for a given strain range is concave downward for most cases. This results from the relatively small increase, and in some cases decreases in the values of the P-I integrals with increasing crack length. At the same time, the crack growth rate increased significantly with crack length. This may be an artifact introduced by neglecting the curvature of the specimen and by the assumption of uniform displacement distribution at the boundary. Despite this undesirable concave distribution of data points, which increases the standard deviation, almost all data points in the figures of da/dN versus ΔJ^*, $\Delta\hat{J}$ and ΔTp^* fell within the bounds of a factor 2 from the straight lines obtained by regression analyses. The ΔTp integral did not correlate the data as well. For this reason we will not consider this integral any further in subsequent efforts. In order to see the temperature-dependent changes of the crack growth rates, the power law representing the isothermal crack growth correlations (Figures 34 through 38) are collectively shown in Figure 39. It is seen that the slope of the line decreases with temperature (with exception of 982°C), while the crack growth rate is always higher

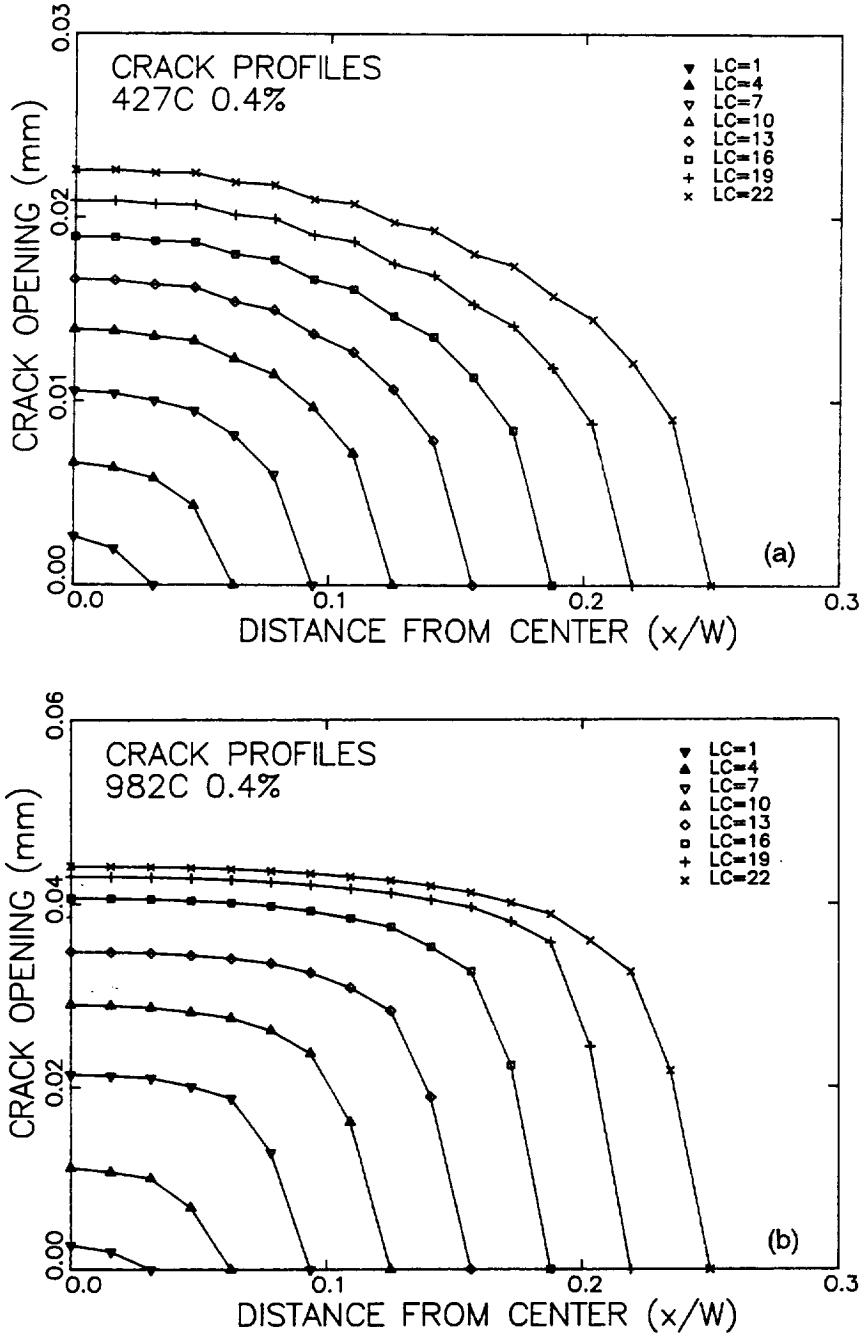

Figure 32. Predicted Hastelloy-X crack profiles at various crack lengths at (a) 427°C and Δε=0.40% and (b) 982°C and Δε=0.40%.

at higher temperatures over the range of the integrals obtained. The temperature dependency appears to diminish if the parameter becomes sufficiently large.

The TMF data are plotted in Figure 40 for 427°C – 871°C out-of-phase specimens, in Figure 41 for the 427°C – 927°C in-phase and out-of-phase specimens, and in Figure 42 for 427°C – 927°C out-of-phase specimens only. It appears that the out-of-phase data (Figures 40 and 42) can be corre-

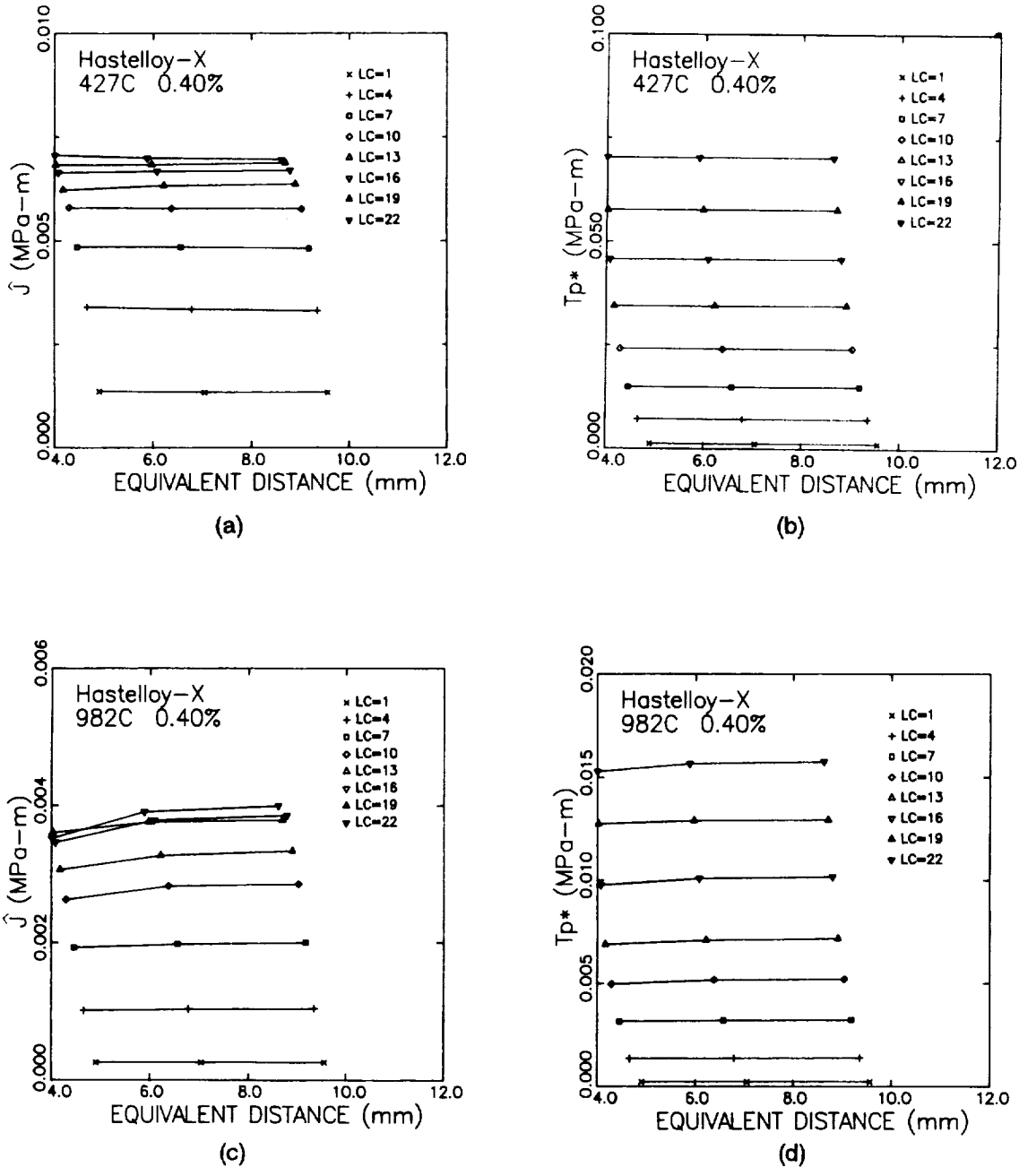

Figure 33. Influence of path on the variation of (a) $\hat{J}$ at 427°C and $\Delta\varepsilon$=0.4%, (b) Tp* at 427°C and $\Delta\varepsilon$=0.4%, (c) $\hat{J}$ at 982°C and $\Delta\varepsilon$=0.4%, and (d) Tp* at 982°C and $\Delta\varepsilon$=0.4%.

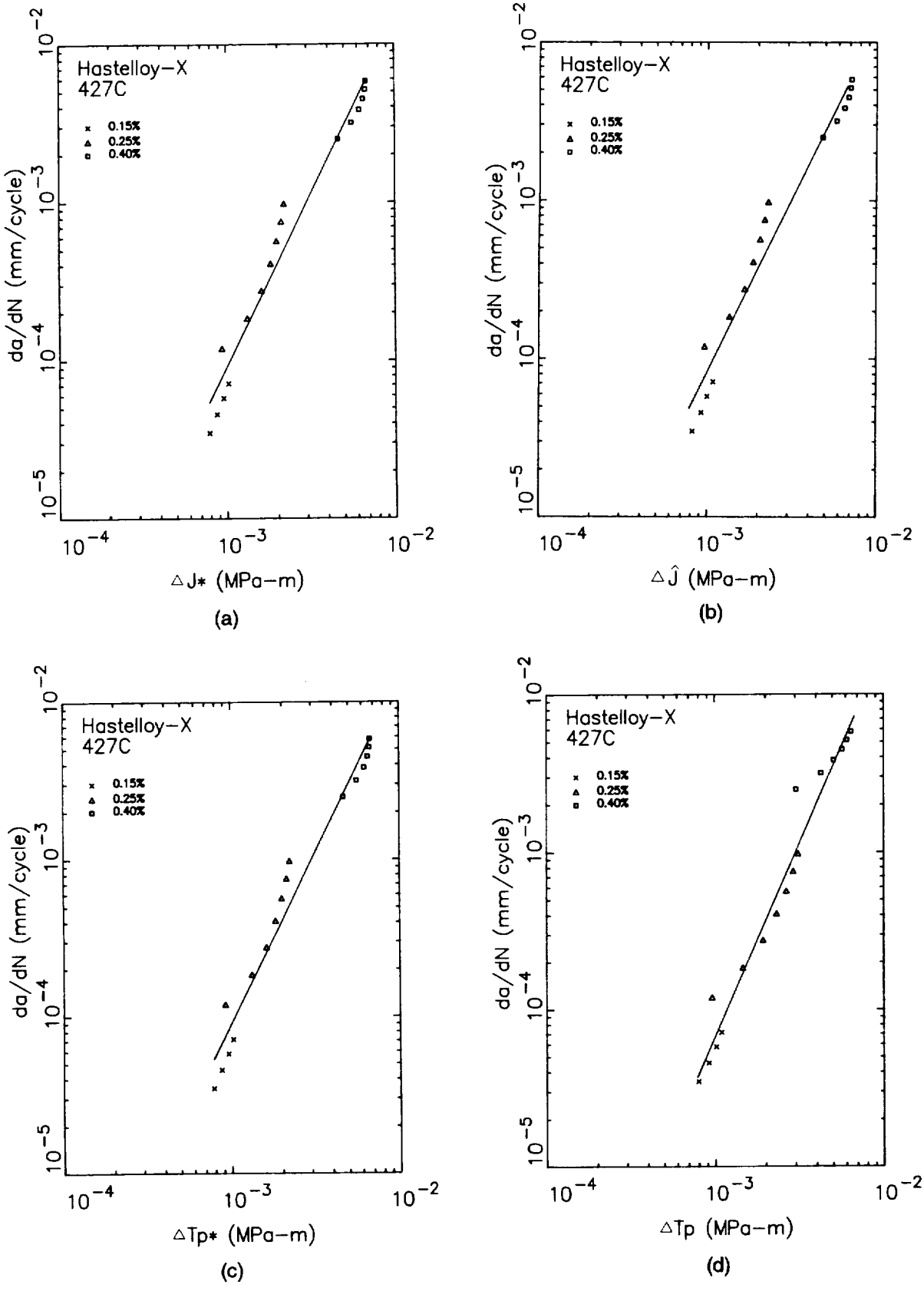

Figure 34. Correlation of Hastelloy-X 427°C isothermal crack growth data with (a) ΔJ^*, (b) $\Delta \hat{J}$, (c) ΔTp^*, and (d) ΔTp.

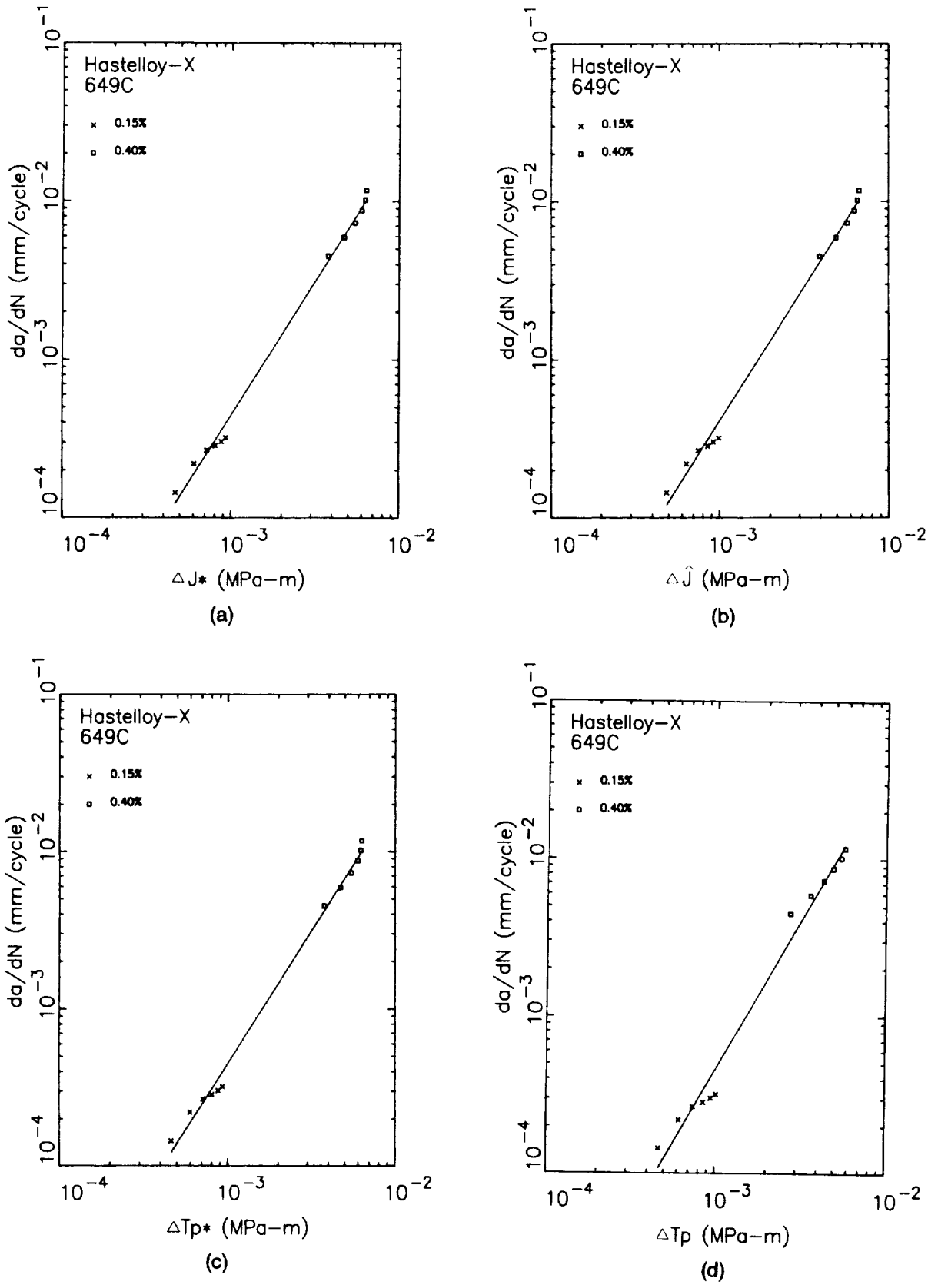

Figure 35. Correlation of Hastelloy-X 649°C isothermal crack growth data with (a) ΔJ^*, (b) $\Delta\hat{J}$, (c) ΔTp^*, and (d) ΔTp.

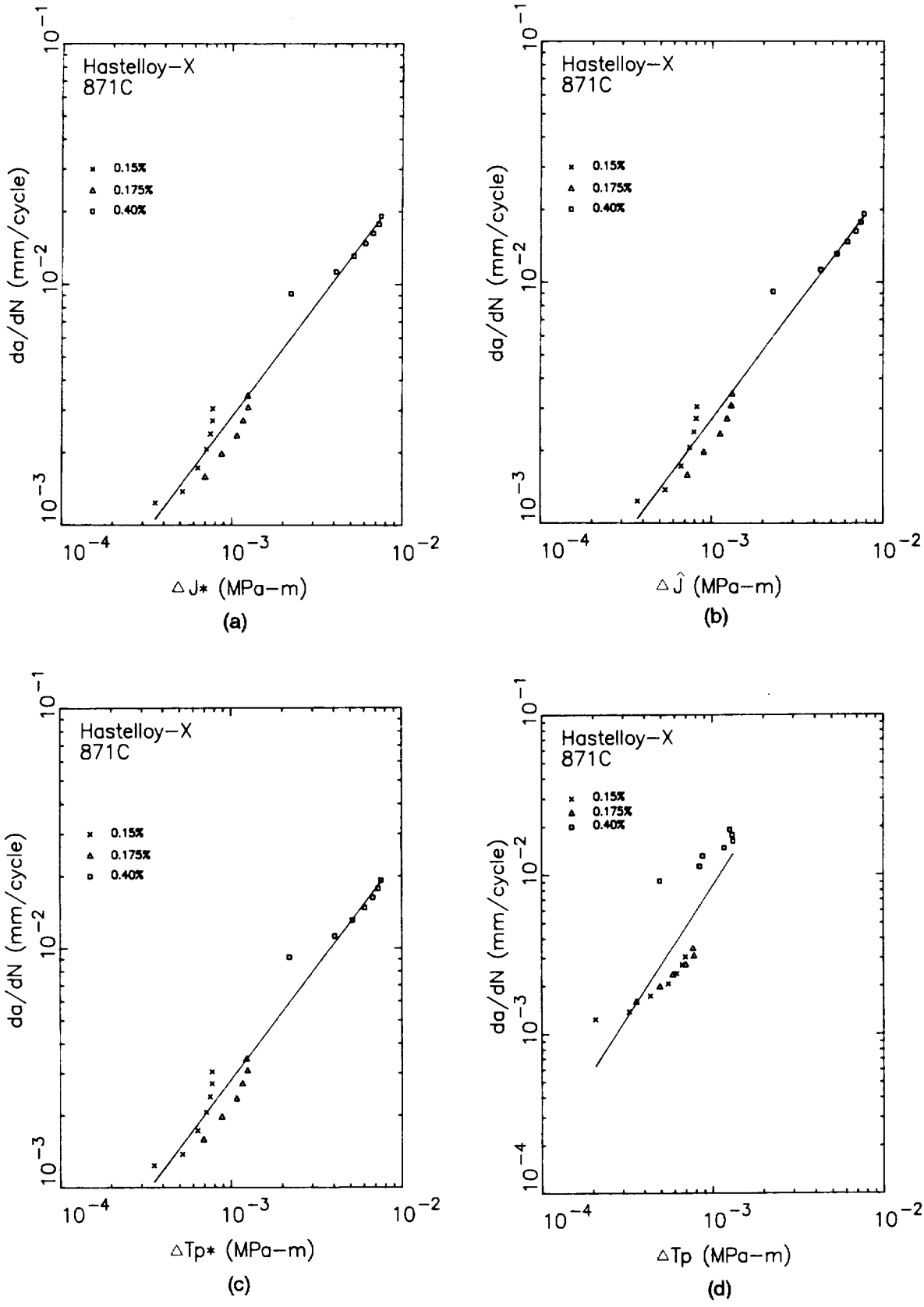

Figure 36. Correlation of Hastelloy-X 871°C isothermal crack growth data with (a) ΔJ^*, (b) $\Delta \hat{J}$, (c) ΔTp^*, and (d) ΔTp.

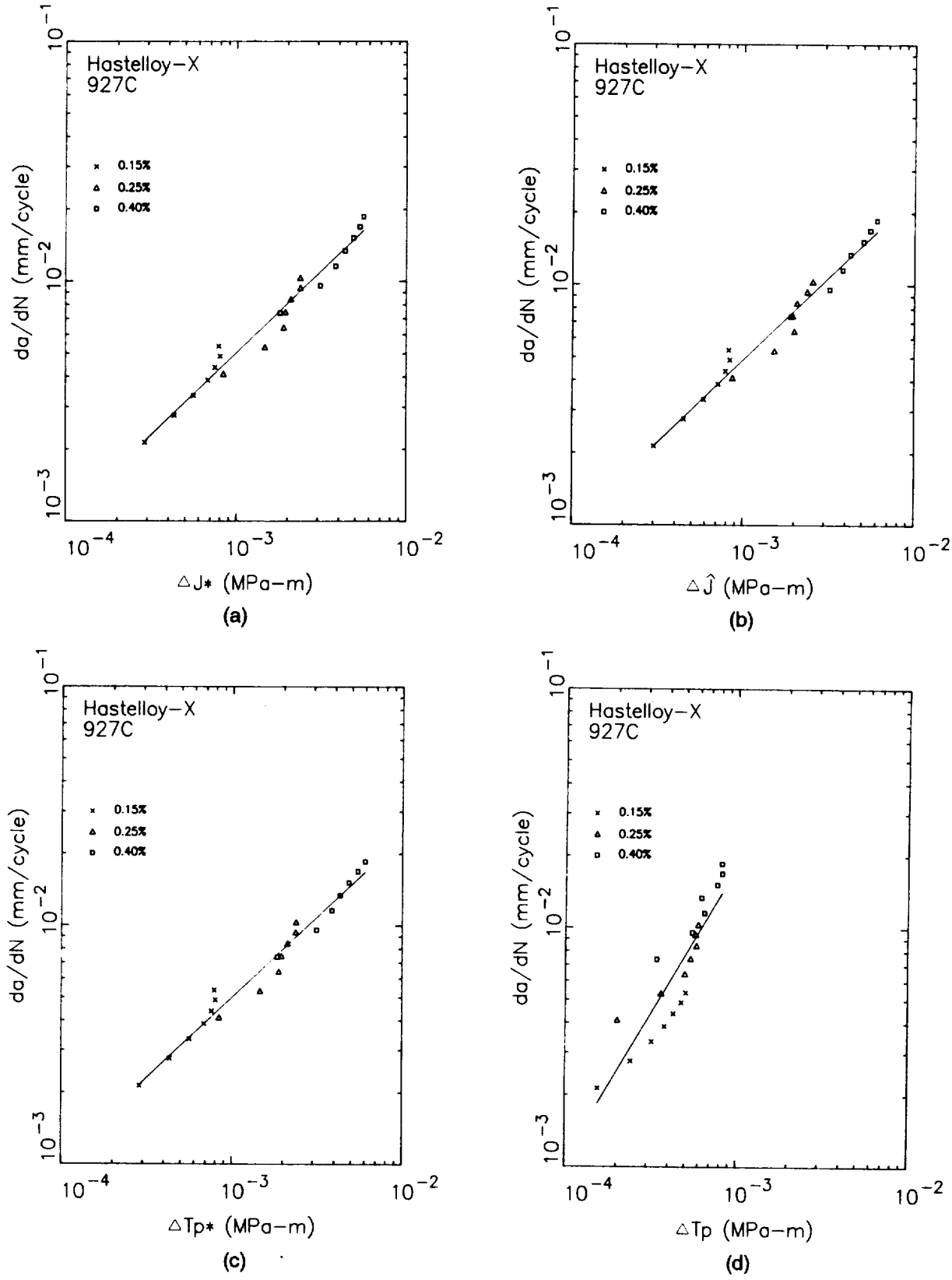

Figure 37. Correlation of Hastelloy-X 927°C isothermal crack growth data with (a) ΔJ*, (b) $\Delta\hat{J}$, (c) ΔTp*, and (d) ΔTp.

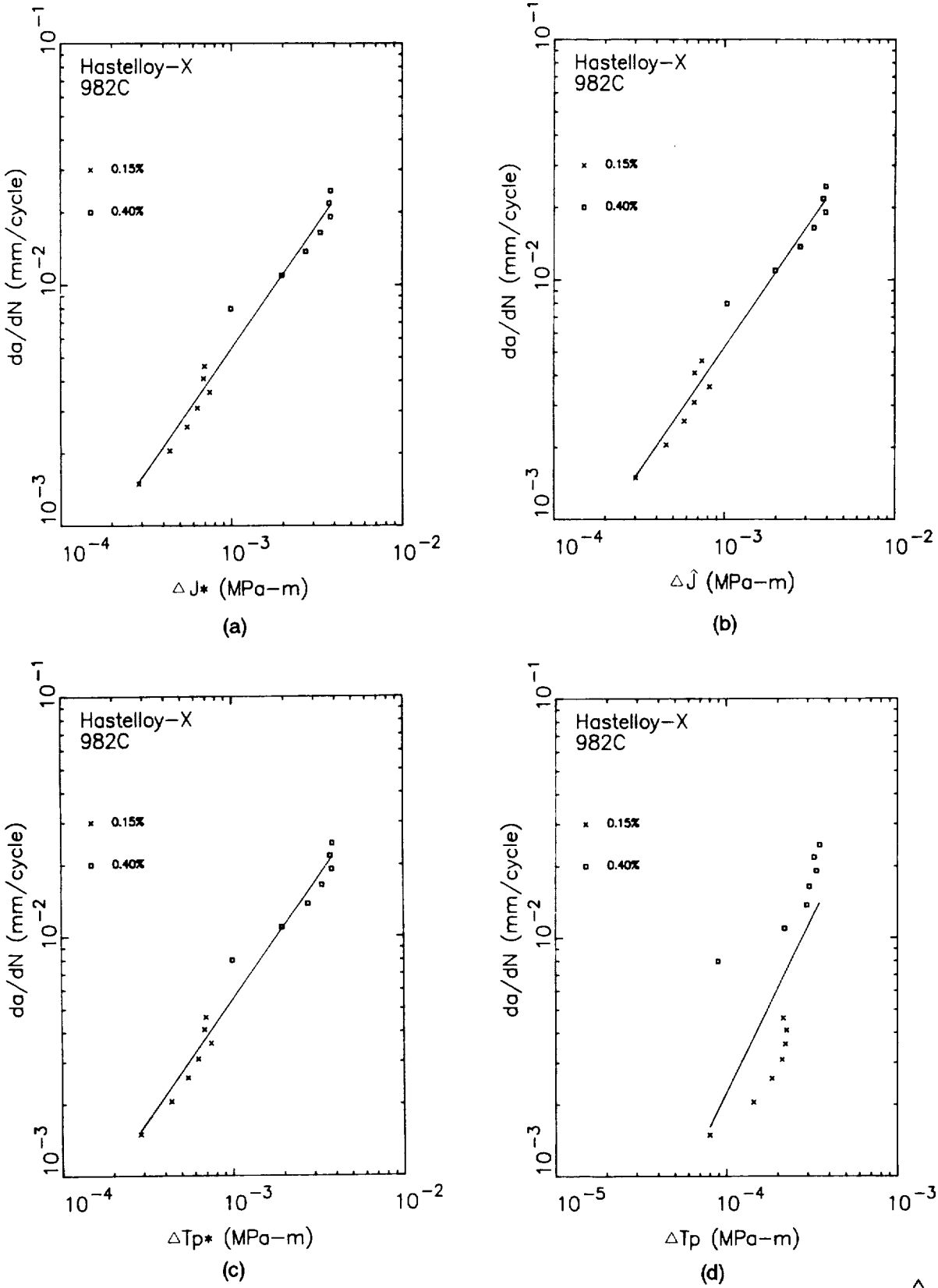

Figure 38. Correlation of Hastelloy-X 982°C isothermal crack growth data with (a) ΔJ^*, (b) $\Delta \hat{J}$, (c) ΔTp^*, and (d) ΔTp.

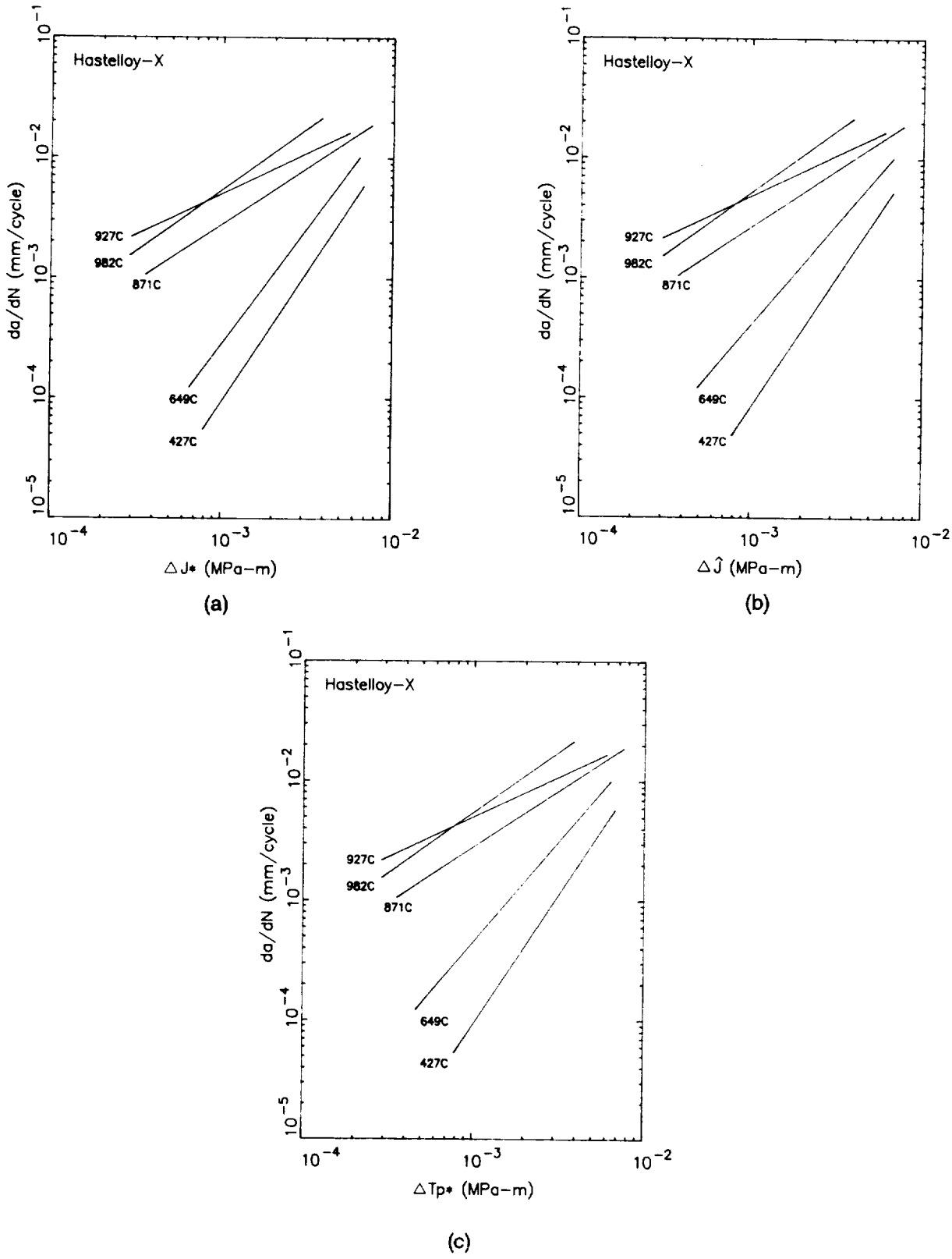

Figure 39. Comparison of Hastelloy-X isothermal crack growth rates as a function of (a) ΔJ*, (b) Δ$\hat{J}$, and (c) ΔTp*.

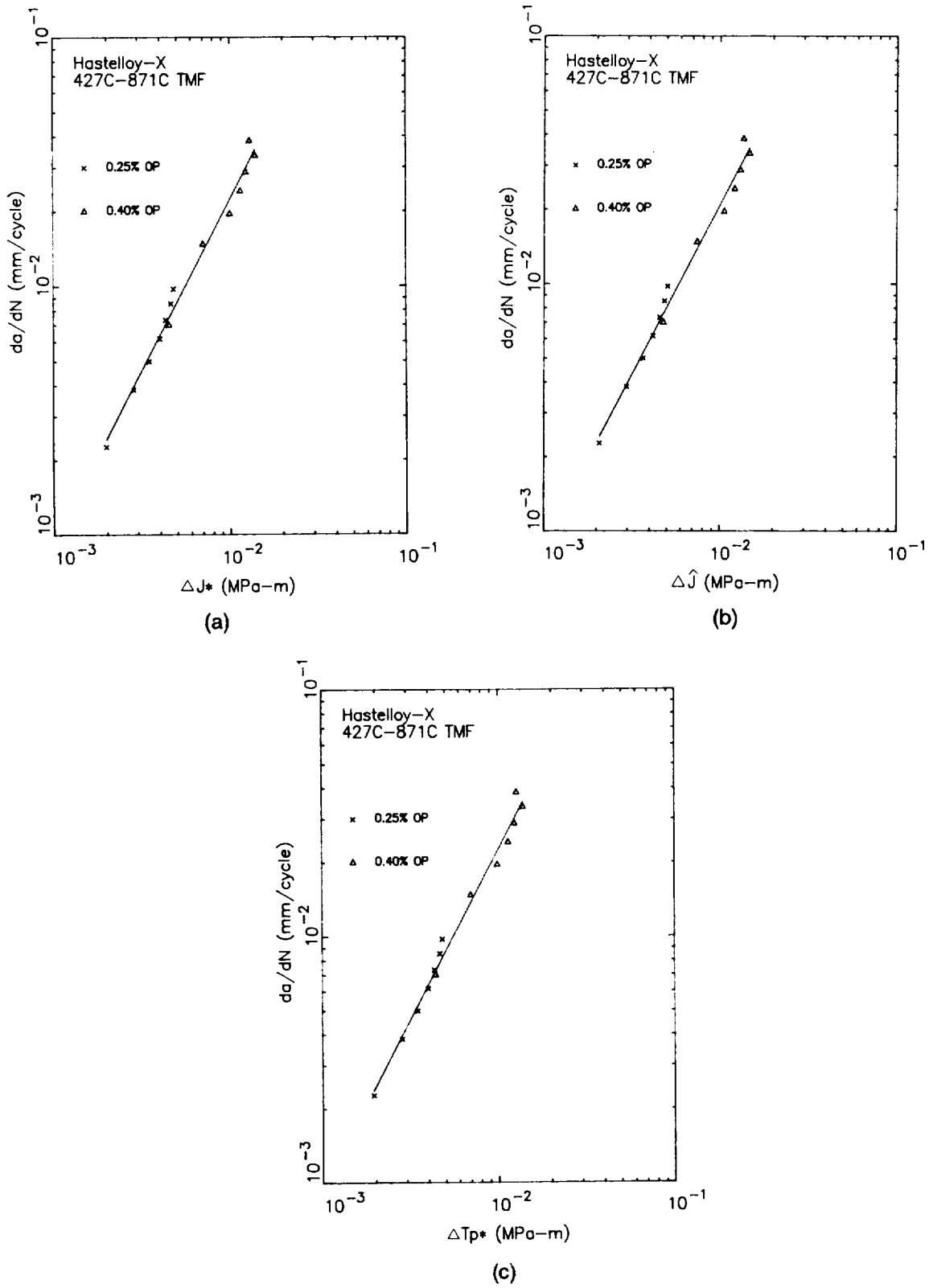

Figure 40. Correlation of Hastelloy-X out–of–phase 427°C – 871°C TMF crack growth data with (a) ΔJ^*, (b) $\Delta \hat{J}$, and (c) ΔTp^*.

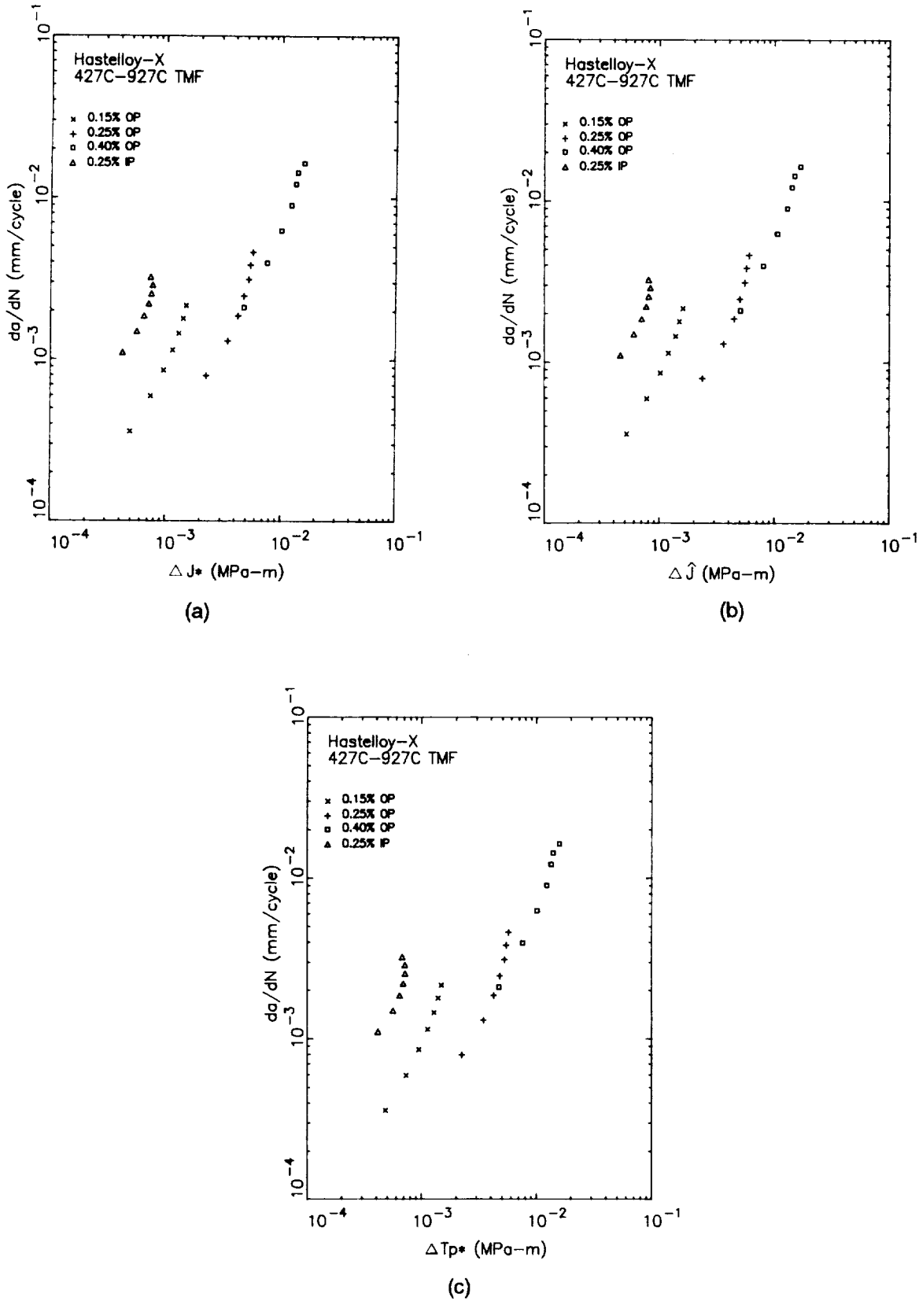

Figure 41. Correlation of Hastelloy-X 427°C – 927°C TMF crack growth data with (a) ΔJ^*, (b) $\Delta \hat{J}$, and (c) ΔTp^*.

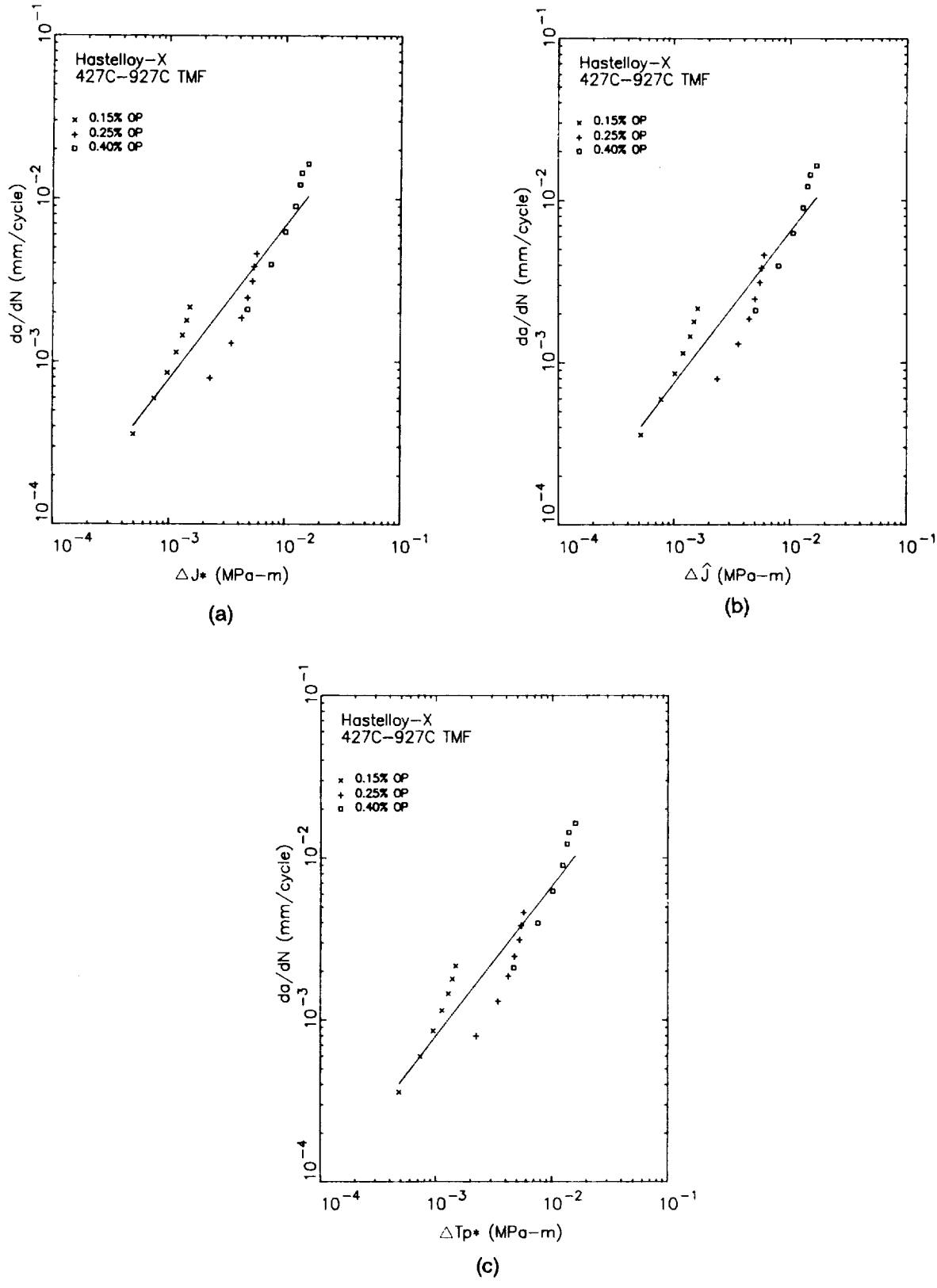

Figure 42. Correlation of Hastelloy-X out–of–phase 427°C – 927°C TMF crack growth data with (a) ΔJ^*, (b) $\Delta \hat{J}$, and (c) ΔTp^*.

lated with ΔJ^*, $\Delta \hat{J}$, and ΔTp^*, although the slopes of the data set for the individual specimen are not always in accord with the slope of the straight line. However, the 427°C-927°C data in Figure 41 show that the in-phase crack growth rates are significantly higher than the out-of-phase data. Therefore, the data of the different phases can not be correlated with a single straight line. These TMF data were also plotted with the isothermal data at the lowest and highest temperatures in the cycle (Figures 43 through 45). It is seen that the TMF data fall between the isothermal data for both temperature ranges. It is also found that the in-phase data for 427°C – 927°C TMF (Figure 44) are closer to 927°C isothermal data compared with the corresponding out-of-phase data (Figures 45).

4.3 Conclusion

The results of this task indicate that ΔJ^*, $\Delta \hat{J}$ and ΔTp^* are good parameters for prediction of crack growth rates at elevated temperatures. The ΔTp integral did not correlate the crack growth data as well. The deformation condition ranged from small scale yielding to large scale yielding wherein most of the area within the gage section deformed plastically. Simplifications made in the analysis such as the stress-strain behavior, the geometry of the model, and the boundary conditions would have some influence on the results. However, it is not expected that different conclusions will be drawn if more precise analyses are performed.

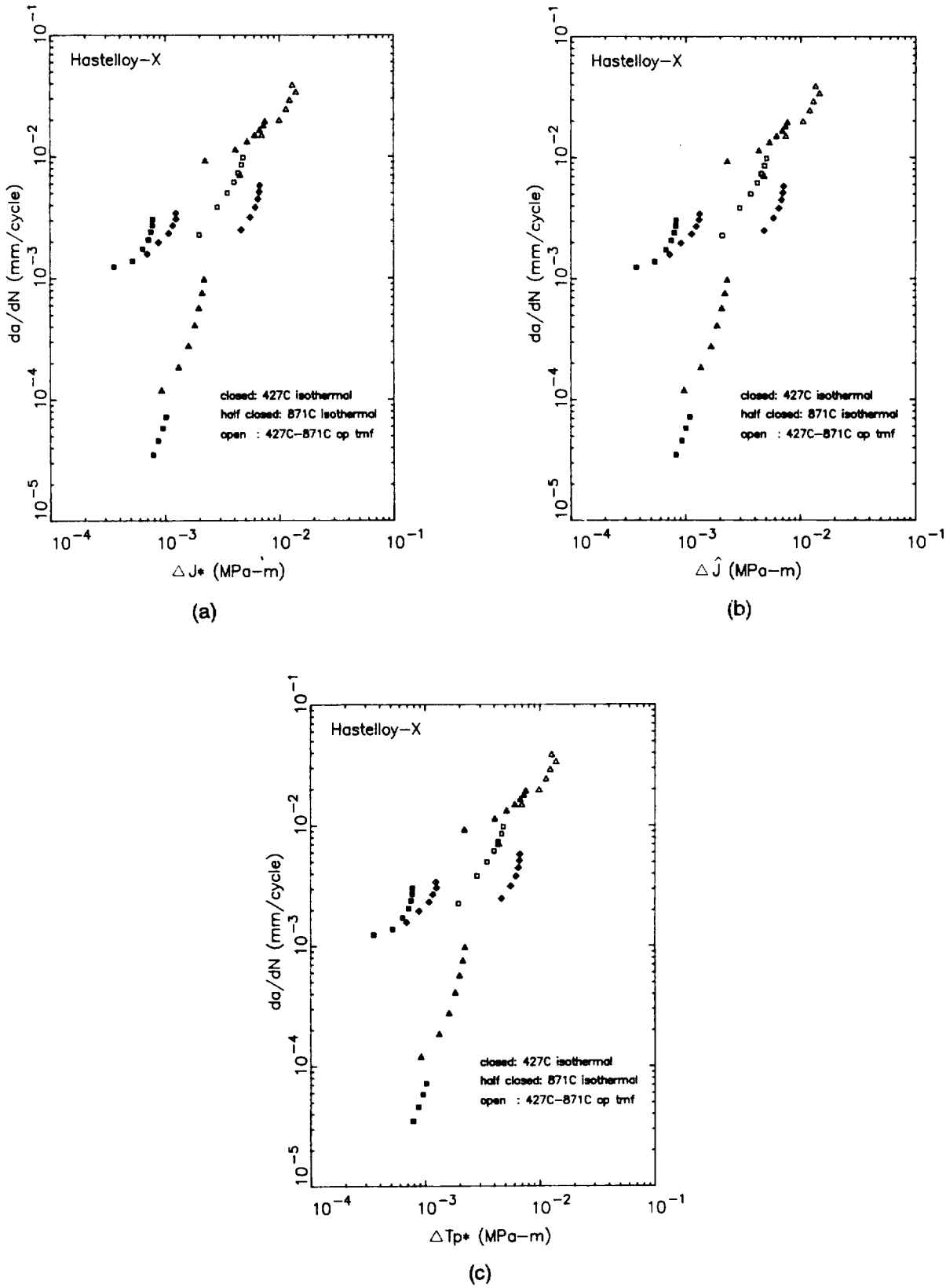

Figure 43. Comparison of Hastelloy-X 427°C – 871°C TMF with 427°C and 871°C isothermal crack growth data as a function of (a) ΔJ*, (b) $\Delta\hat{J}$, and (c) ΔTp*.

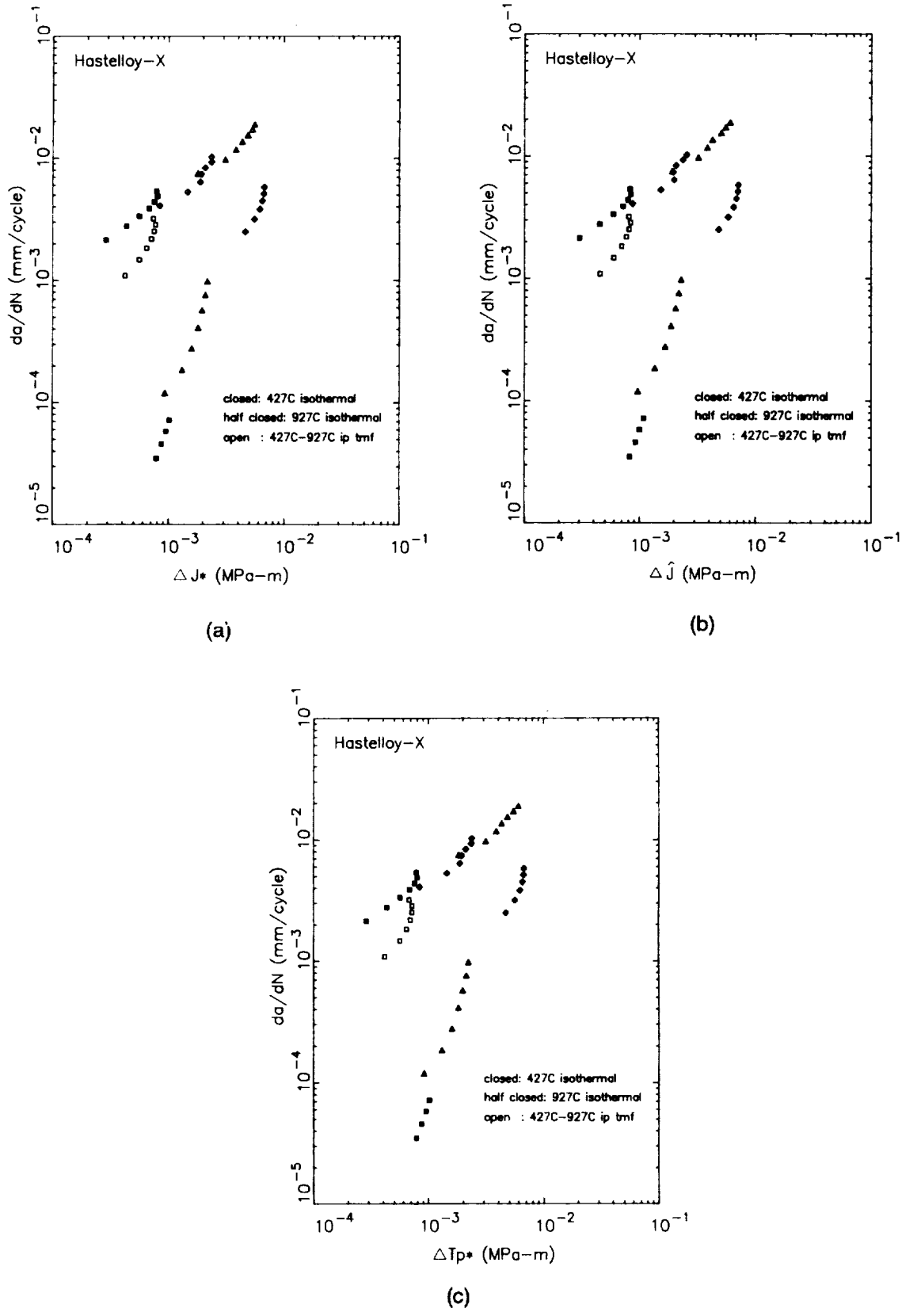

Figure 44. Comparison of Hastelloy-X 427°C – 927°C in-phase TMF with 427°C and 927°C isothermal crack growth data as a function of (a) ΔJ^*, (b) $\Delta\hat{J}$, and (c) ΔTp^*.

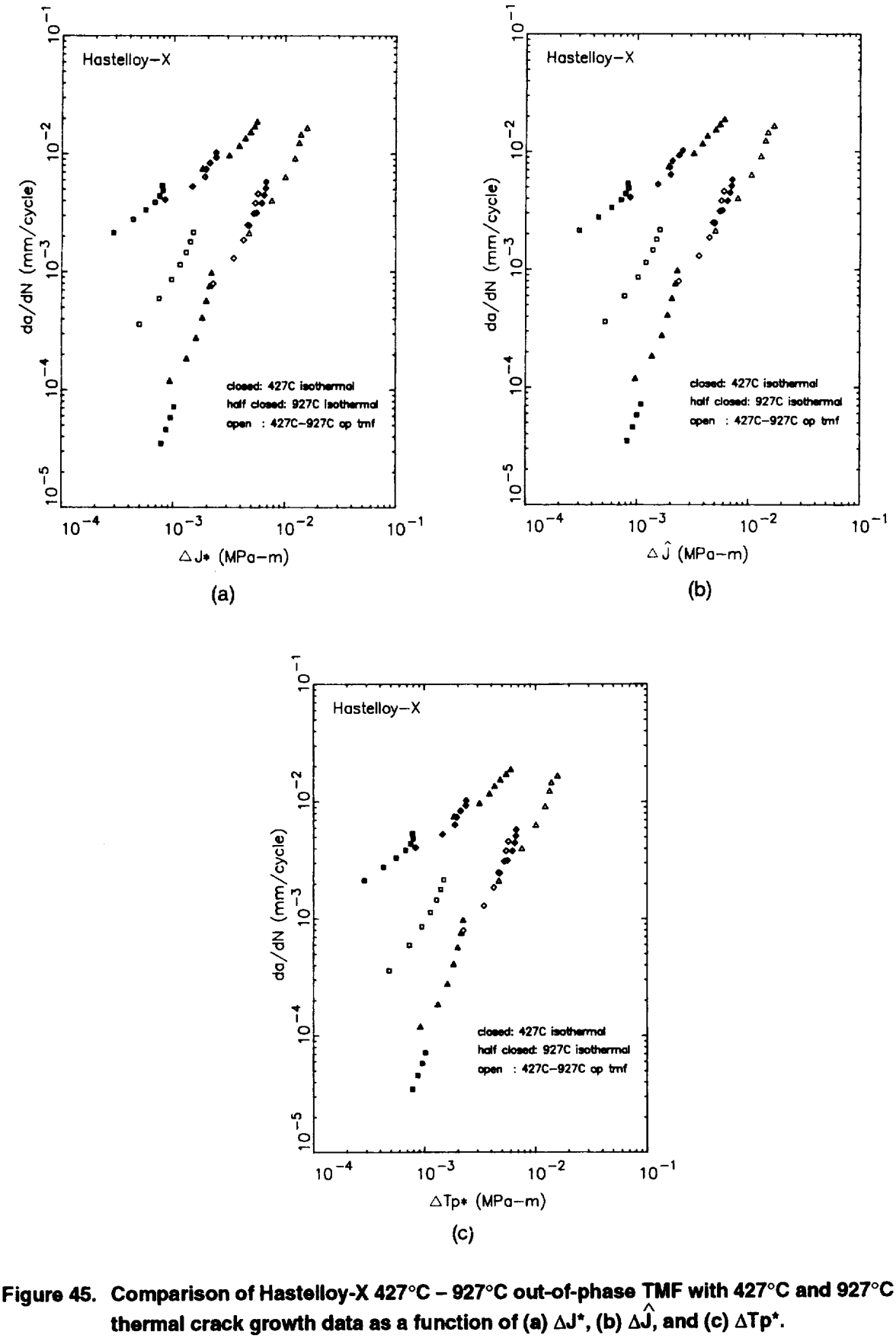

Figure 45. Comparison of Hastelloy-X 427°C – 927°C out-of-phase TMF with 427°C and 927°C isothermal crack growth data as a function of (a) ΔJ^*, (b) $\Delta \hat{J}$, and (c) ΔTp^*.

5.0 Input for Finite Element Analysis of Time-Dependent Crack Growth

This section discusses the constitutive theory used in the crack growth analysis and how the boundary conditions were generated for the analysis. The finite element code used in this program is CYANIDE[29], which is a GEAE in-house code for cyclic nonlinear analysis. The general numerical scheme used in this program is described elsewhere[30].

5.1 Constitutive Theory

The constitutive theory used for the time-dependent analysis in this program is the classical theory where the time-independent and time-dependent inelastic deformations are uncoupled and separately considered. The time-independent plasticity is based on the Besseling's theory[31] wherein the material is assumed to consist of a number of elastic-perfectly plastic materials which follows the Prandtl-Reuss flow rule, the Von Mises yield criteria and the kinematic flow rule in the strain space. The time-dependent deformation is based on a power-law creep equation:

$$\varepsilon_c = K(\sigma/\sigma_o)^n t^m + q(\sigma/\sigma_o)^r t \qquad (31)$$

where K, n, m, q, and r are material constants and σ_o is a reference stress. For the varying stress amplitudes the strain hardening scheme is used. For a tensorial representation of the strain components and for other details, the reader is referred to the work of Krause[32]. The constitutive properties of Alloy 718 other than the creep properties have been fully discussed in the final report of the base program[1].

5.1.1 Creep Data Analysis

The creep tests on Alloy 718 were conducted at 538°C, 593°C and 649°C in the base program. The total inelastic strain versus time data were presented in the final report of the base program[1]. The elapsed time when the constant stress was established on the specimen from the start of the test was 24 seconds. The strain recorded up to this time was assumed to be the instantaneous response. The creep strain was obtained by subtracting the instantaneous response from the total strain. The creep strain at 538°C showed spurious oscillation with time. It is not known what caused the problem. This oscillation was not observed for 593°C and 649°C data. The creep data showed considerable scatter as usually observed for this material. It is highly unlikely that a regression analysis would provide meaningful information on this data with large scatter obtained from a limited number of samples. Consequently, the creep constants were obtained manually using the data on two representative stress levels at each temperature. The results yielded enormously large exponents on the stress. Similar trends were experienced in other tests on Alloy 718 conducted in inhouse programs. The large exponents on the stress give rise to numerical problems in the finite element analysis of the time-dependent deformation, as verified with a four-element model (Figure 46). Furthermore, the exponent n determined from two levels of stress overpredicted the creep strain at higher stresses to a large extent. It was concluded that the current power law model for the creep deformation is not the best model for this material in load control test which are preceded by large amounts of plasticity.

Many of the time-dependent crack growth tests performed in this program experienced significant amounts of stress relaxation, particularly those at elevated temperatures. As a result, a series of stress relaxation tests were conducted at three strain levels (4.5%, 1.15% and 0.4%) at the three temperatures and also at 427°C. The stress relaxation data showed that there was no significant

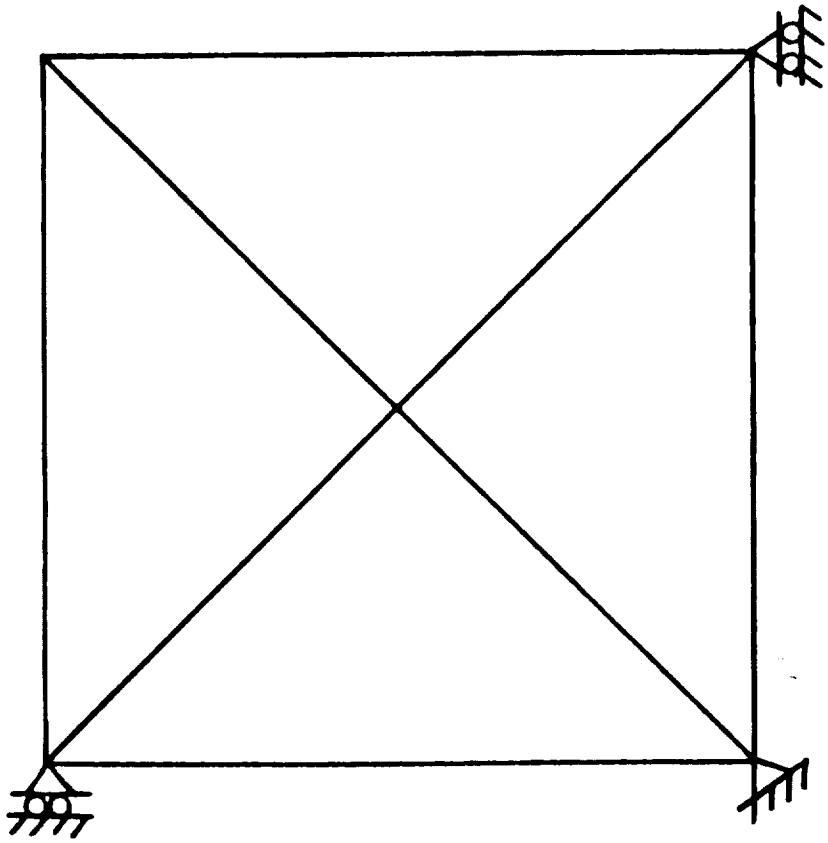

Figure 46. Four-element model used for Alloy 718 stress relaxation analysis.

time-dependent deformation at 427°C. Thus, only the higher temperature data were analyzed. The creep constants were determined by trial and error by comparing the experimental data with the calculated creep strain and stress relaxation obtained using the four-element model. The final values of the constants are given in Table 2.

Table 2. Creep constants of Alloy 718.

	538°C	593°C	649°C
k	0.3×10^{-4}	0.18×10^{-3}	$1. \times 10^{-2}$
m	0.08	0.09	0.10
n	6.0	3.6	1.2
q	0.5×10^{-6}	0.53×10^{-5}	0.5×10^{-4}
r	12	12	12

Note: σ_0 = 689.5MPa in equation (31)
Units: σ (MPa), t (hours), ε (m/m)

Figure 47 shows the comparison of the predicted and measured creep strain with time at 538°C. Figure 48 shows the predicted and measured stress relaxation in the 538°C stress relaxation tests. Figure 49 shows a similar comparison for ΔS, the amount of stress relaxation, i.e. $\sigma(0)-\sigma(t)$. Figures 50 through 52 show similar comparisons for test performed at 593°C and Figures 53 through 55 compare the predicted and observed creep behavior in the 649°C tests.

An inspection of the predicted and test data reveals the following aspects:

- The stress relaxation is overpredicted at 0.4% strain and underpredicted at 4.5% strain, except for very small times at 593°C and 649°C. This would lead to less stress relaxation in the vicinity of the crack tip in the strain control crack growth tests.
- The crossover of the relaxation curves of 4.5% and 1.15% strains at small times (Figures 51b and 54b) cannot be predicted with the power law equation.
- The selected constants predict much faster relaxation of the stress at very small times for 593°C and 649°C compared with experimental data.
- The creep data at 593°C do not appear to compare well between the test and prediction. The creep constants for this temperature were calculated by linear interpolation for m, n and r and by log-linear interpolation for k and q, using the constants obtained at 538°C and 649°C. This was done because of excessive scatter in the creep data at this temperature[1].

Despite these discrepancies, the overall comparison appears to be reasonably acceptable considering the amount of scatter normally found in the creep data for this material.

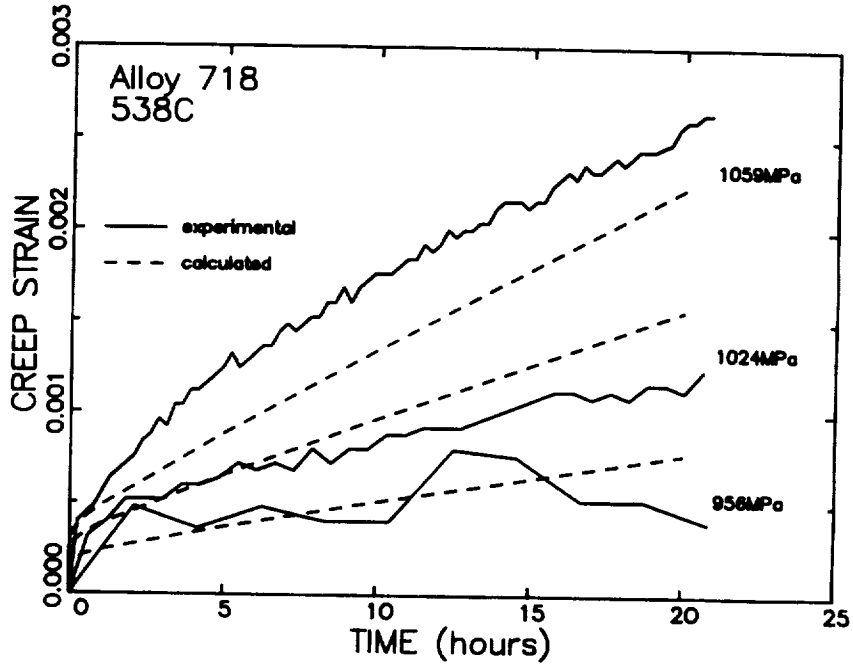

Figure 47. Alloy 718 creep strain versus time at 538°C.

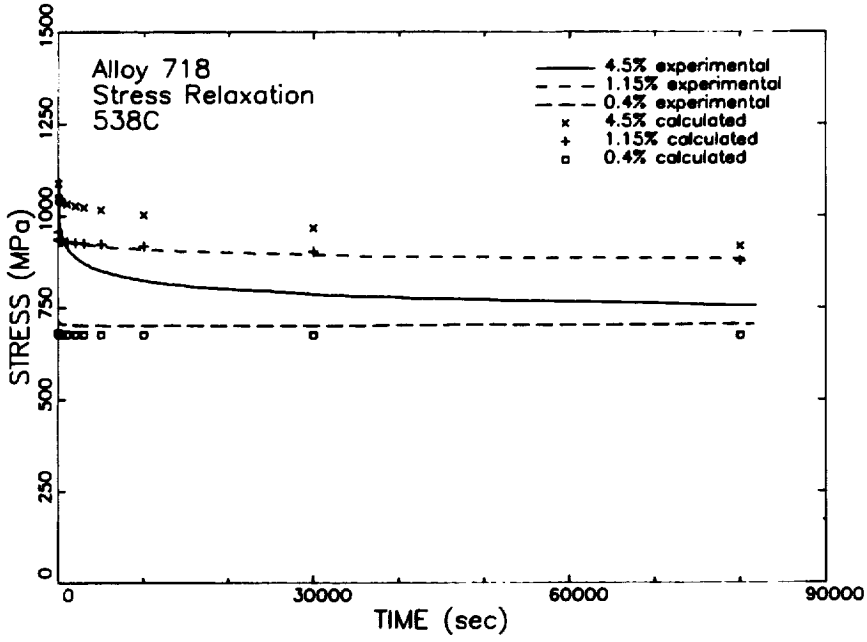

(a)

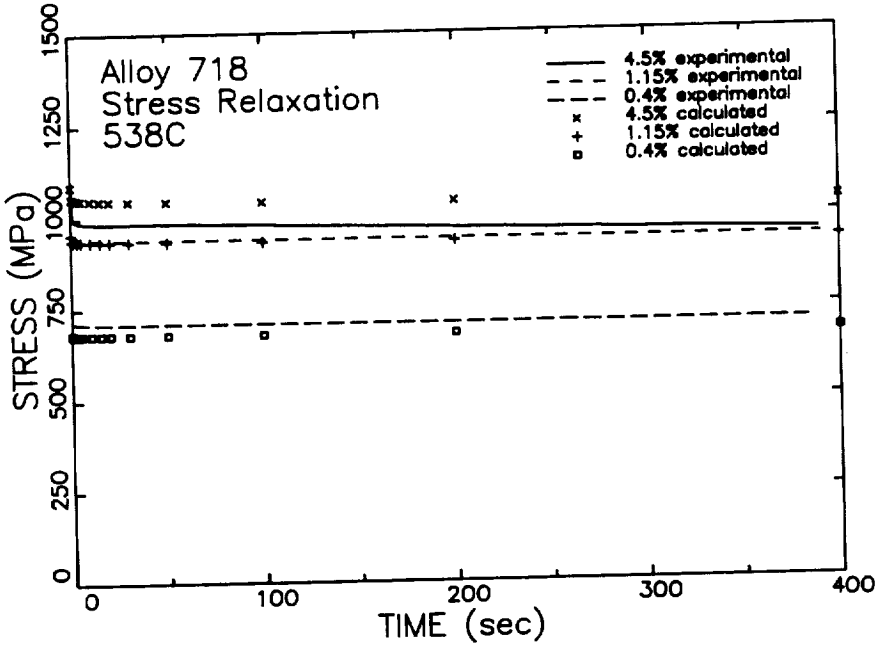

(b)

Figure 48. Alloy 718 stress relaxation at 538°C with (a) large and (b) small times.

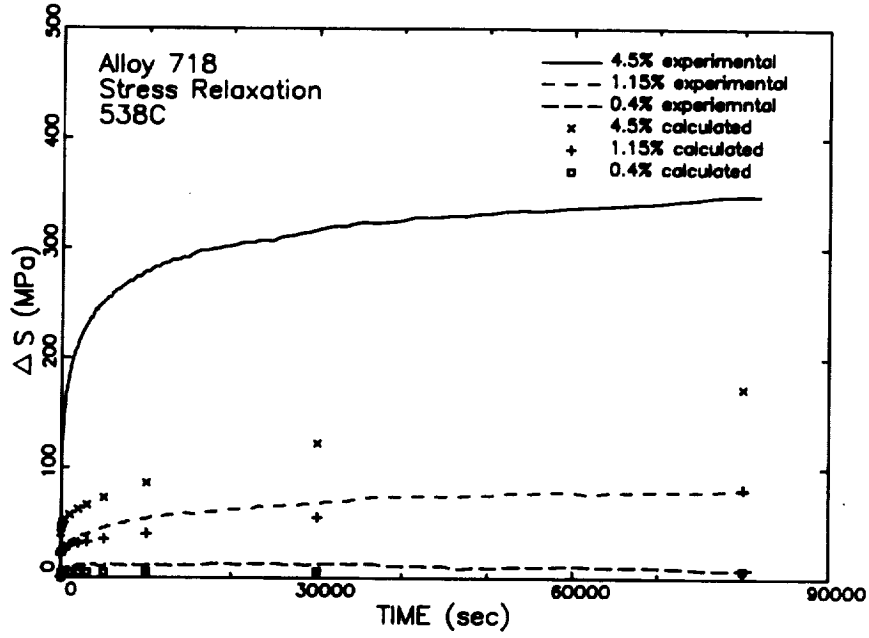

(a)

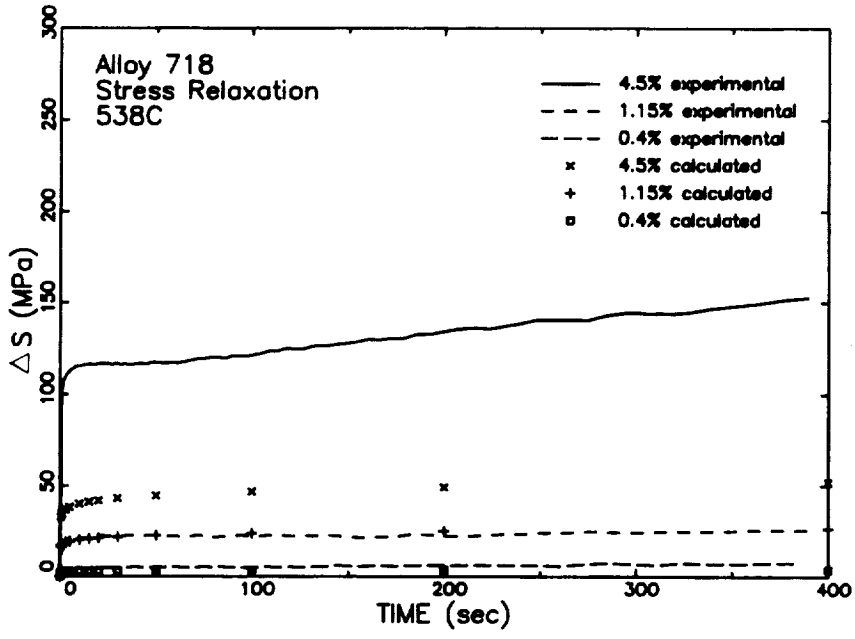

(b)

Figure 49. Magnitude of Alloy 718 relaxed stress at 538°C for (a) large and (b) small times.

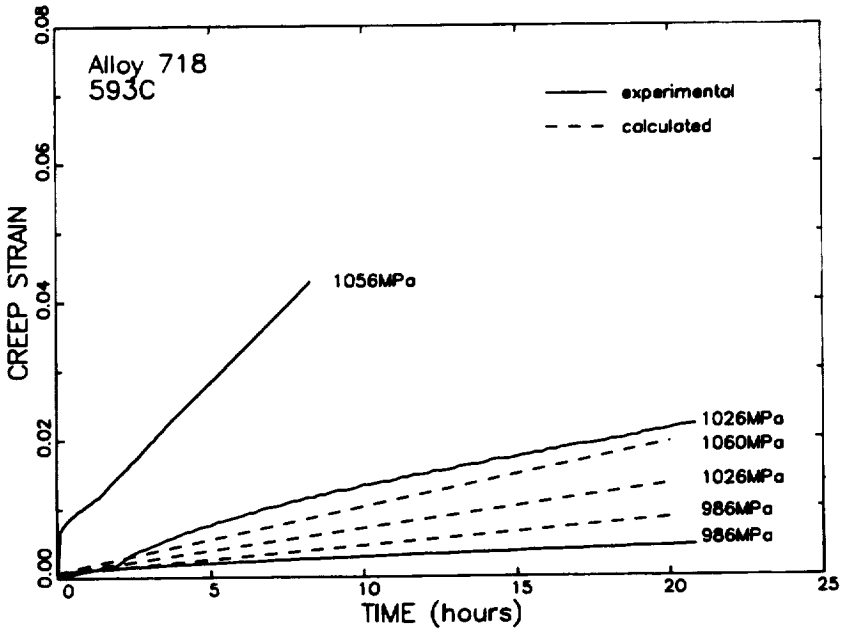

Figure 50. Alloy 718 creep strain versus time at 593°C.

5.2 Boundary Conditions

The boundary displacements at the gage length of the SEN specimen analyzed in the base program were approximated by linear interpolation and extrapolation of the control displacement and back face displacement. The validity of the linear extrapolation to estimate the front face displacement from the control and back face displacements was substantiated analytically and experimentally. It was not obvious that this scheme is accurate for the time-dependent crack growth tests. In order to evaluate the accuracy of this approach, a total of three 649°C, R=0, 30 second hold time tests have been performed in strain control with strain ranges of approximately 1%. All three tests were performed with three 12.7 mm gage length extensometers to simultaneously monitor the control, back face, and front face deflections.

The first 30 second hold time test (specimen N11-12) was cycled with 1.5 second ramps (1.5-30-1.5). The data from this test clearly demonstrated the bending that occurs in the specimen as the crack grows. The displacements on the front face were slightly smaller than those predicted by linear extrapolation of the control and back face displacements. The gain setting between the command and the feedback signals of the control extensometer were not optimized which led to a small increase in the mean strain level. The difference in this level correlated with the amount of error between the experimentally measured and linearly interpolated front face displacements.

The second test (specimen N11-15) experienced serrated yielding during the loading in the first cycle which resulted in shutting the test down. Yielding of the test specimen occurred during the first cycle, however, the amount of inelastic deformation at the three extensometer locations was not known. The initial cycle was performed with 1.5 second ramps. Comparison of this loading rate (0.67%/sec) with the observations of serrated yielding in the tensile tests from the base program[1] indicated that reducing the strain rate would reduce the probability of serrated yielding. As a result, the remainder of this test was run with 3-second ramps (3-30-3) without any evidence of serrated

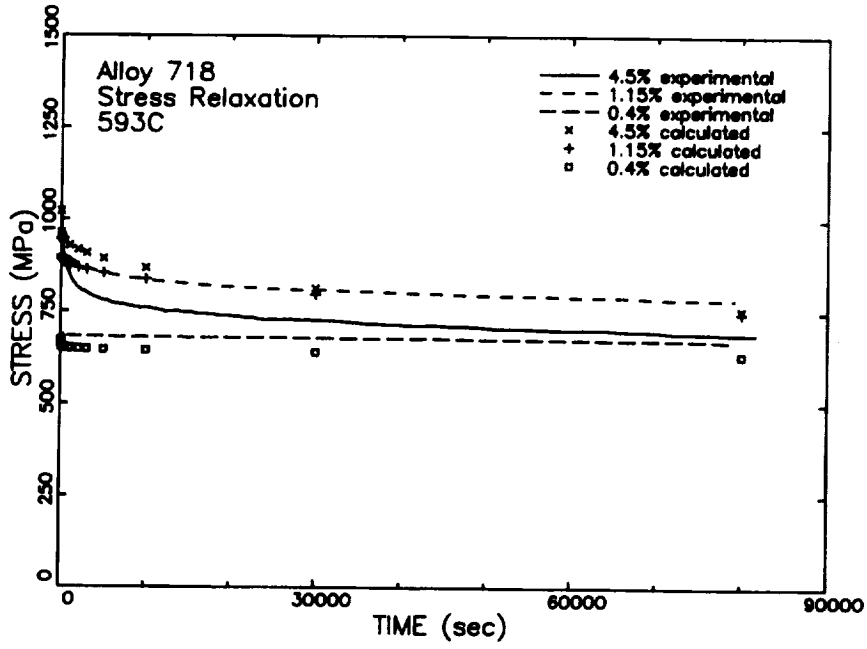

(a)

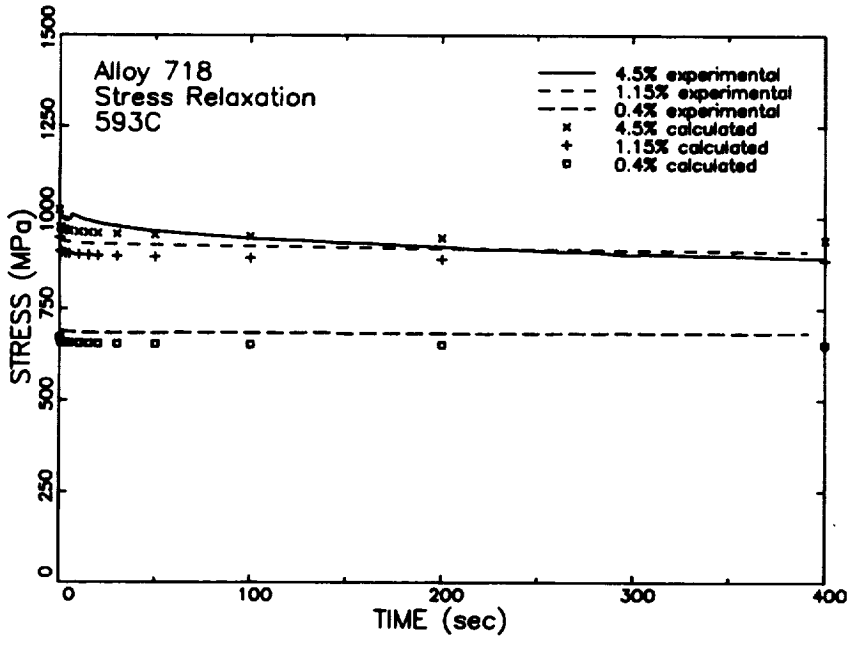

(b)

Figure 51. Alloy 718 stress relaxation at 593°C with (a) large and (b) small times.

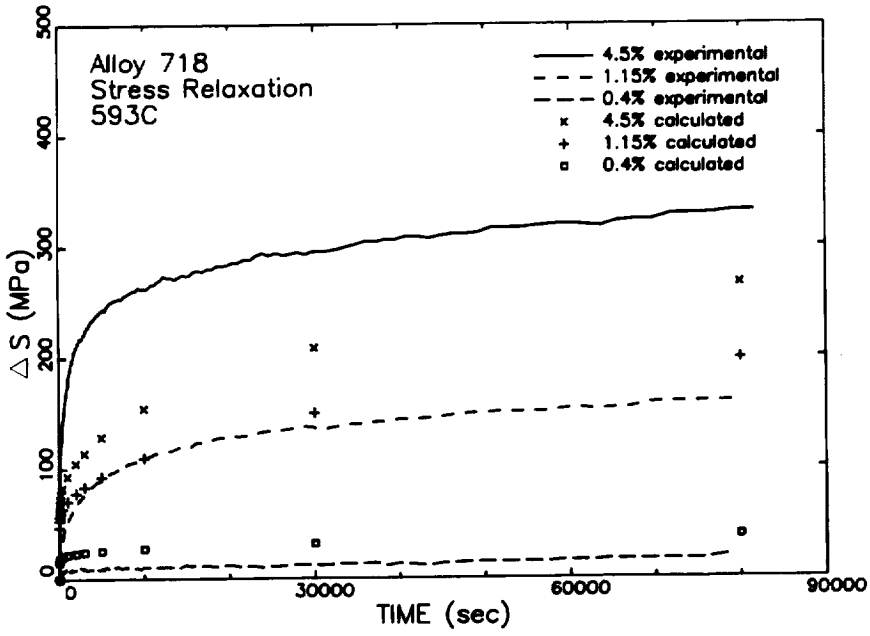

(a)

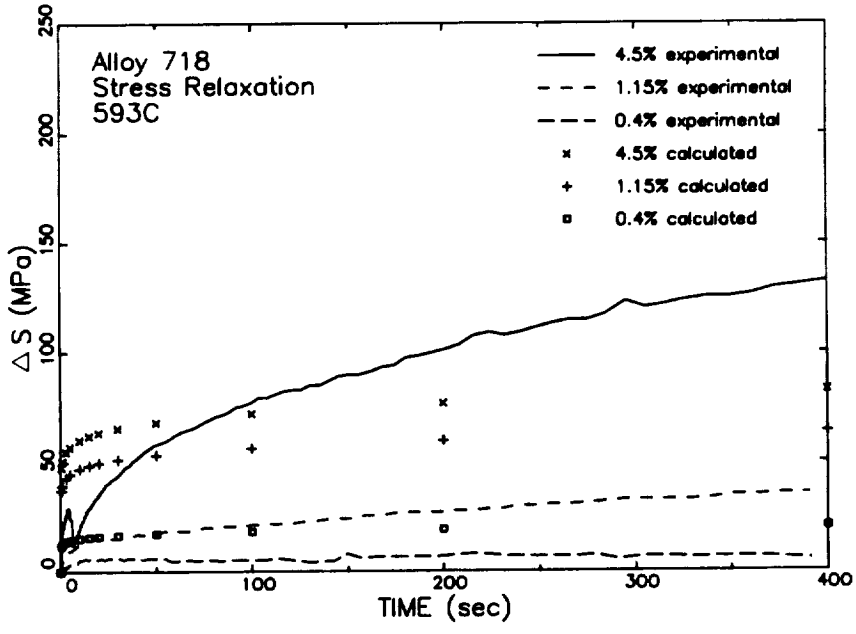

(b)

Figure 52. Magnitude of Alloy 718 relaxed stress at 593°C for (a) large and (b) small times.

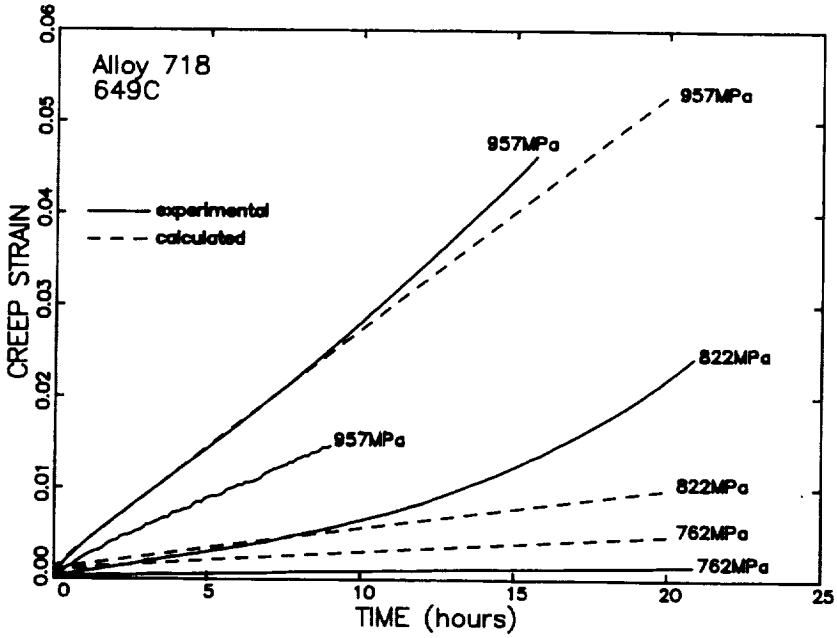

Figure 53. Alloy 718 creep strain versus time at 649°C.

yielding. The front face displacement increased and the back face displacement decreased as the crack grew.

The third test (specimen N11-32) was performed with a strain range of 1.15% and a 3-second ramp cycle (3-30-3). Small EDM depressions were used to locate the extensometers and prevent slippage. This test was performed without incident. Qualitatively, the sum of the back face and front face displacements appeared to remain constant as the crack grew.

The experimental data from specimen N11-32 were analyzed and finite element analyses were performed to study the sensitivity of different displacement boundary conditions. Figure 56 shows the variation of stress (load/uncracked specimen area), control displacement, back face displacement, and front face displacement with cycles in this specimen. Also shown in Figure 56d is the linear extrapolation of the front face from the control and back face displacements. Although the extrapolated displacement mirrors the trends in the experimental data, there is not absolute agreement, particularly for the displacement at the minimum strain condition. In this case, the extrapolated value is approximately 0.02mm larger than the near-zero experimental value throughout the entire test. The extrapolated maximum value is initially higher than the experimental data, but approaches the experimental data with increased cycling.

The load-displacement hysteresis loops for cycles where the crack lengths are approximately 0.95mm (cycle 16) and 2.54mm (cycle 44) are shown in Figures 57 and 58. Figures 57c and 58c show that the linear extrapolated front face displacements are close to the experimental data, but there appears to be a small but consistent difference. As a result of this difference, a second extrapolation technique was attempted, where the front face displacement was adjusted using the minimum back face displacement from the first cycle. During the remainder of the experiments, this approach was utilized because it was extremely difficult to simultaneously measure the remote crack front displacement and the crack mouth opening displacement (CMOD). The influence of the two extrapolation approaches on the experimentally measured remote front face displacements is shown in

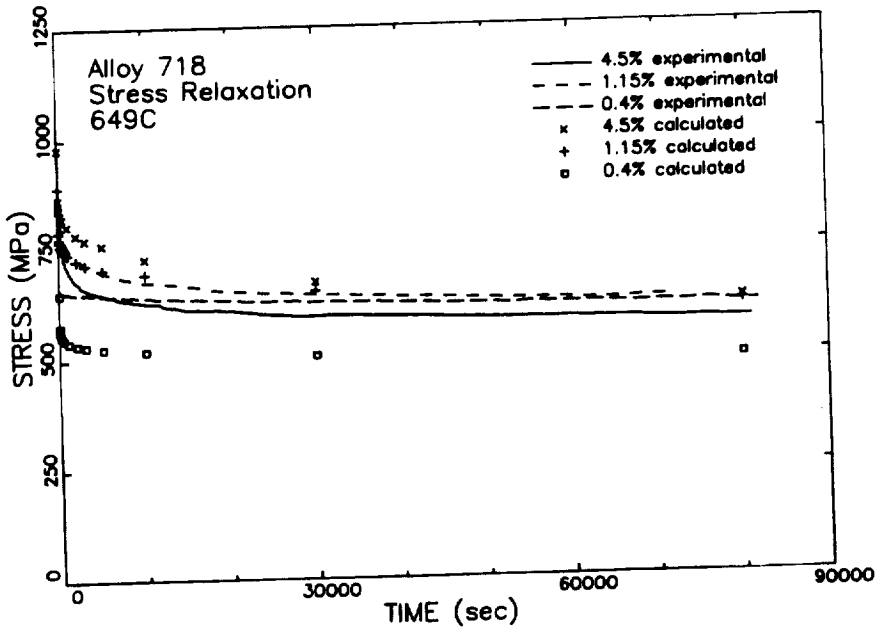

(a)

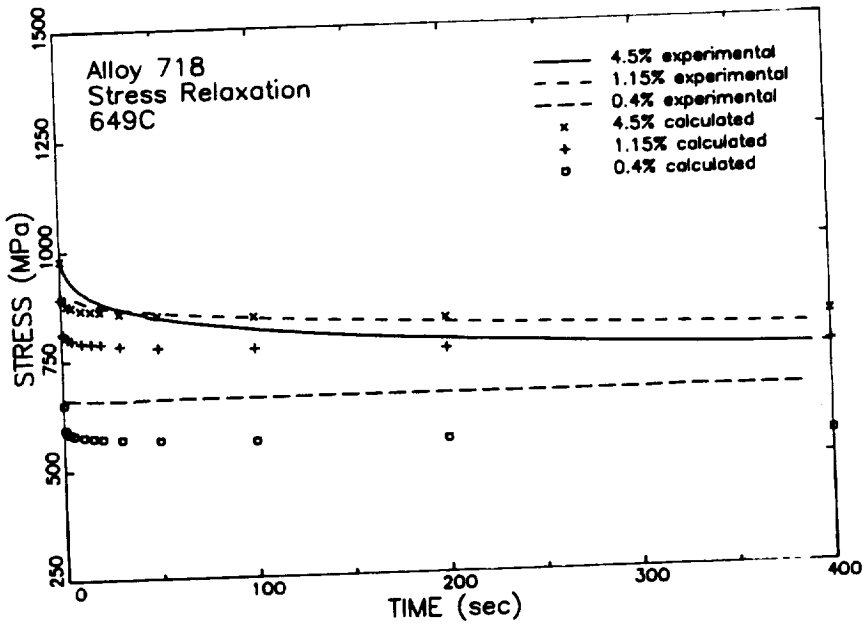

(b)

Figure 54. Alloy 718 stress relaxation at 649°C with (a) large and (b) small times.

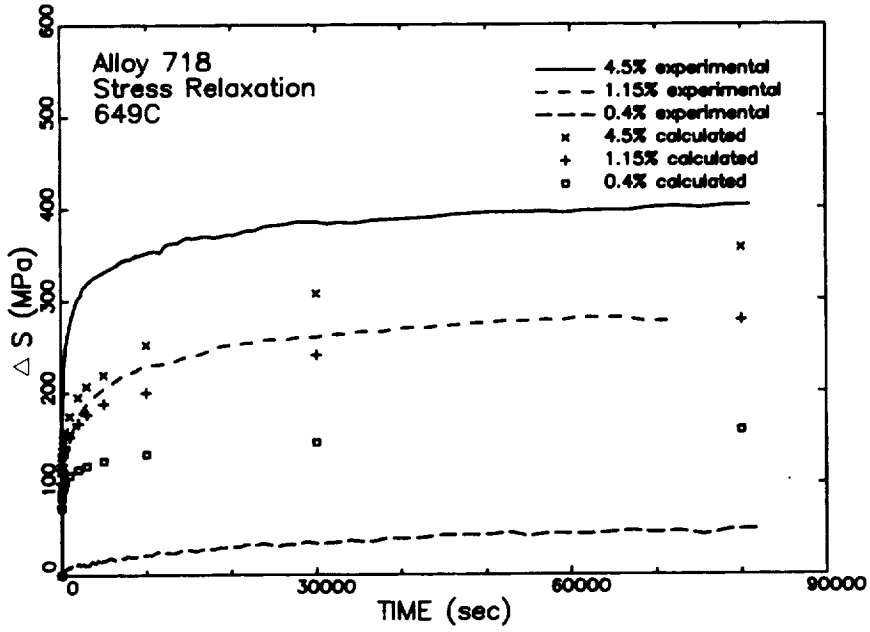

(a)

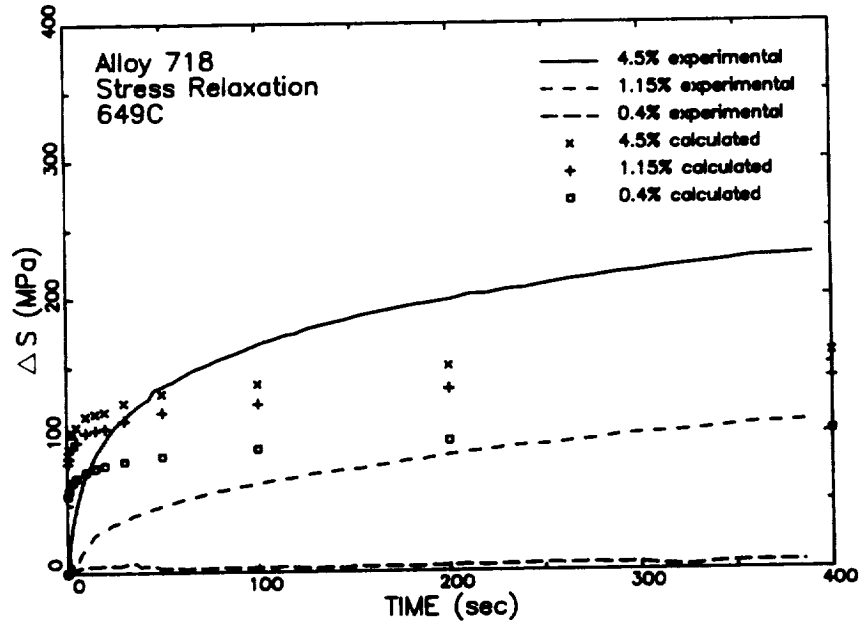

(b)

Figure 55. Magnitude of Alloy 718 relaxed stress at 649°C for (a) large and (b) small times.

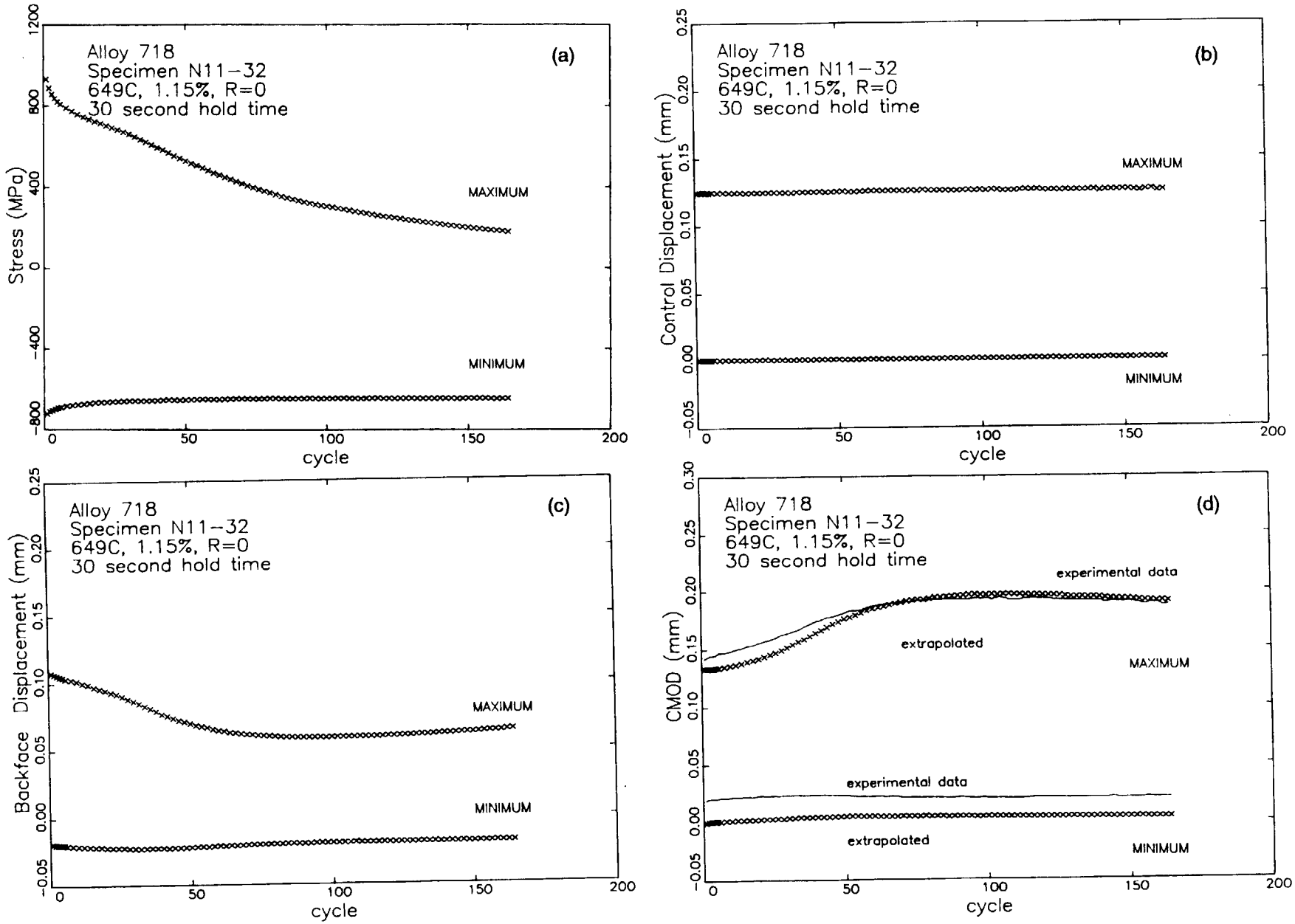

Figure 56. Variation of (a) stress, (b) control displacement, (c) back face displacement, (d) front face displacement with cycles in Alloy 718 specimen N11–32.

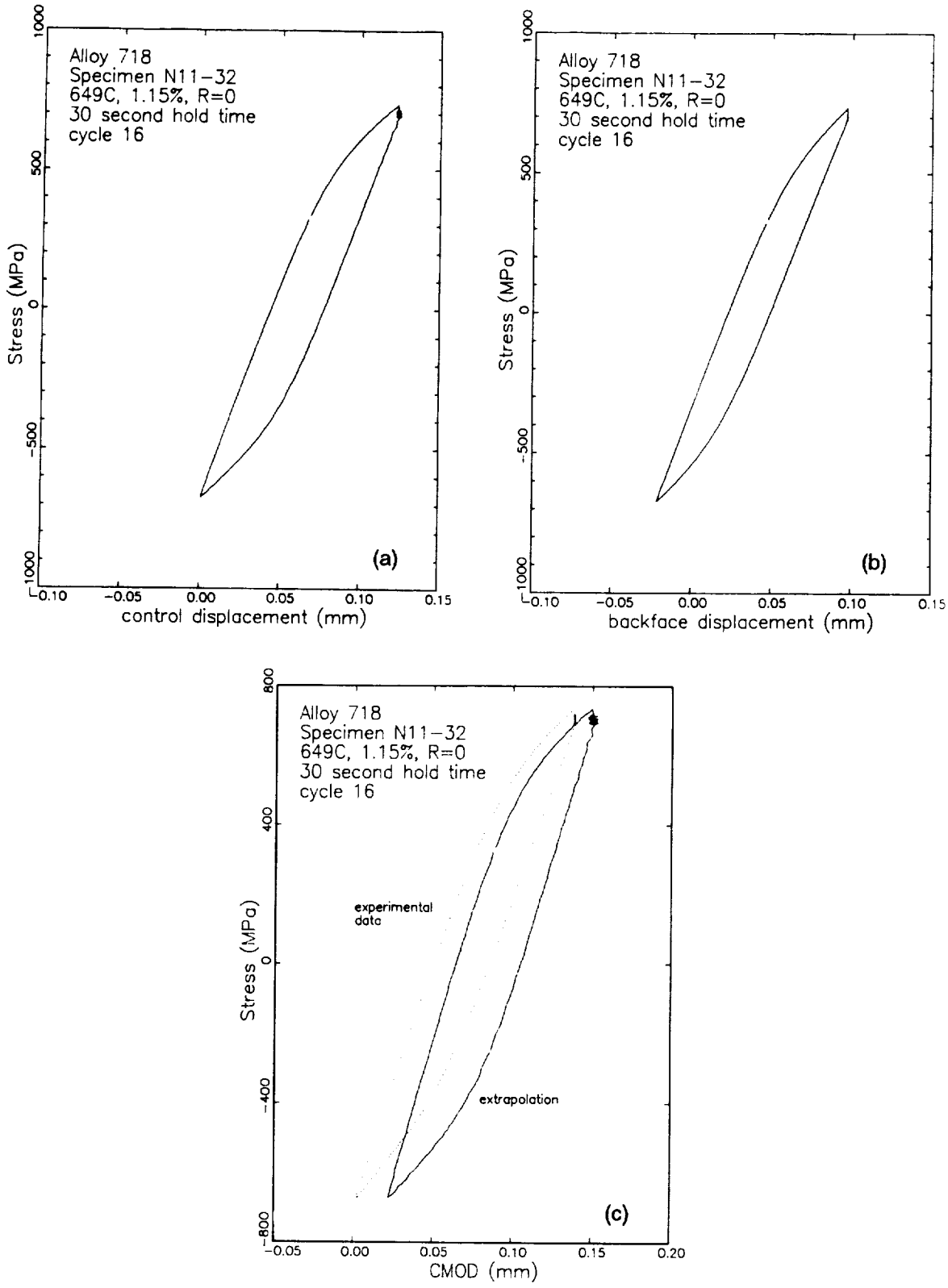

Figure 57. Hysteresis loops of (a) control displacement, (b) back face displacement, and (c) front face displacement at cycle 16 of Alloy 718 specimen N11-32.

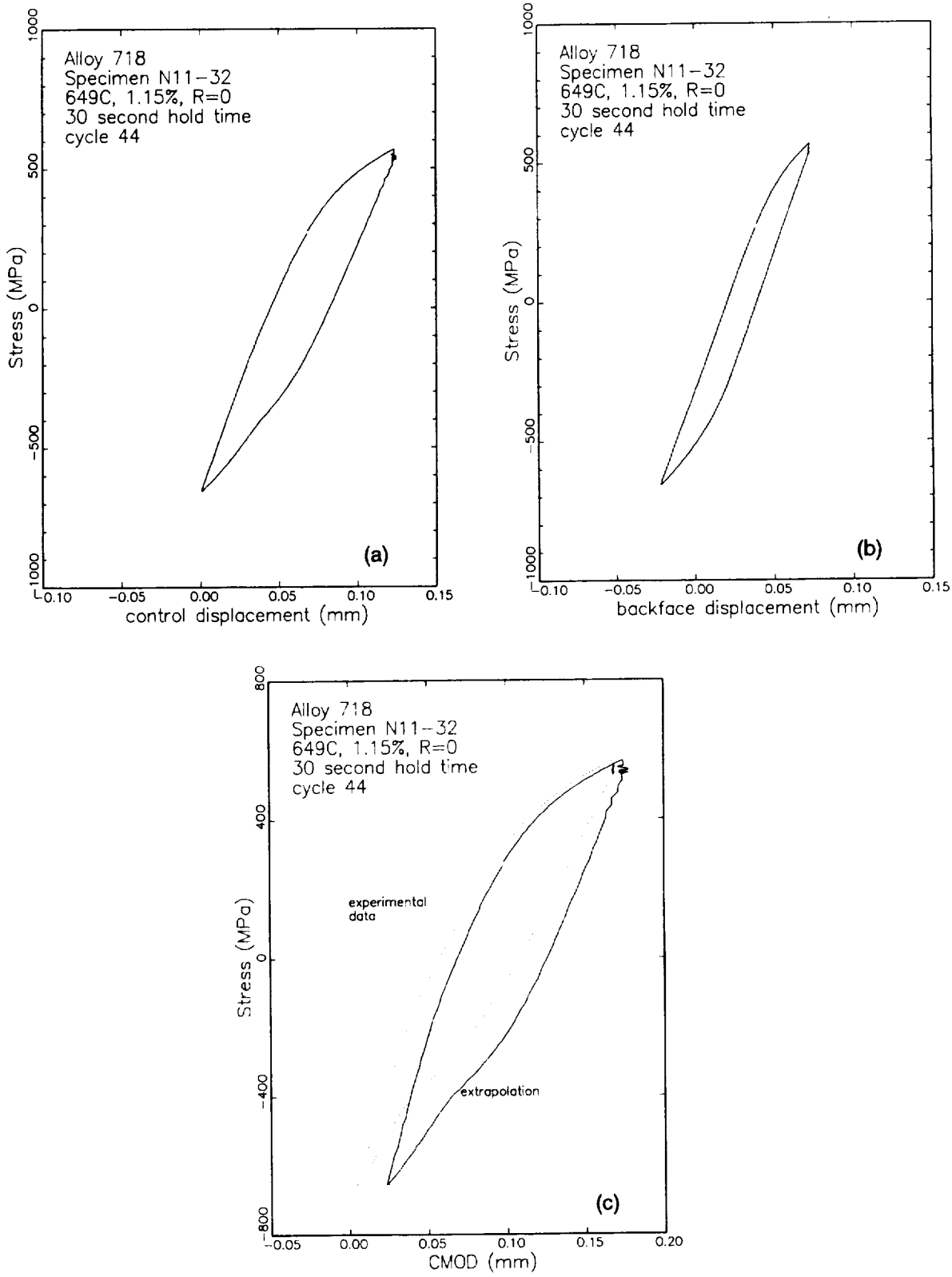

Figure 58. Hysteresis loops of (a) control displacement, (b) back face displacement, and (c) front face displacement at cycle 44 of Alloy 718 specimen N11–32.

Figure 59. The linear extrapolation are the same values shown in Figure 56d, and thus have the same trend. The offset extrapolation predicts the minimum displacements and the initial maximum displacement very well. The agreement between the experimental and offset extrapolation of the maximum displacement diminished as the crack grew. Based on these data, it is not obvious which extrapolation technique should be used for the finite element method (FEM) simulation of crack growth.

This was investigated by performing FEM simulation using three different sets of remote displacement boundary conditions:

1. Linear extrapolation
2. Offset extrapolation
3. Experimental data obtained at the three locations.

For the latter two cases, the nodal displacements were determined assuming quadratic variation of displacement with distance. A FEM analysis was performed using the cyclic properties for Alloy 718 determined in the base program[1]. This does not consider the time-dependent stress relaxation experienced during the hold time. This crack growth simulation was used as a sensitivity study of the boundary displacement distribution on some measurable variables. The results of the FEM analysis are shown in Figure 60. Neither the stress, CMOD values, nor CMOD range vary significantly with these three distributions. It was concluded from these that the linear extrapolation would be satisfactory for the analyses to be performed in this program.

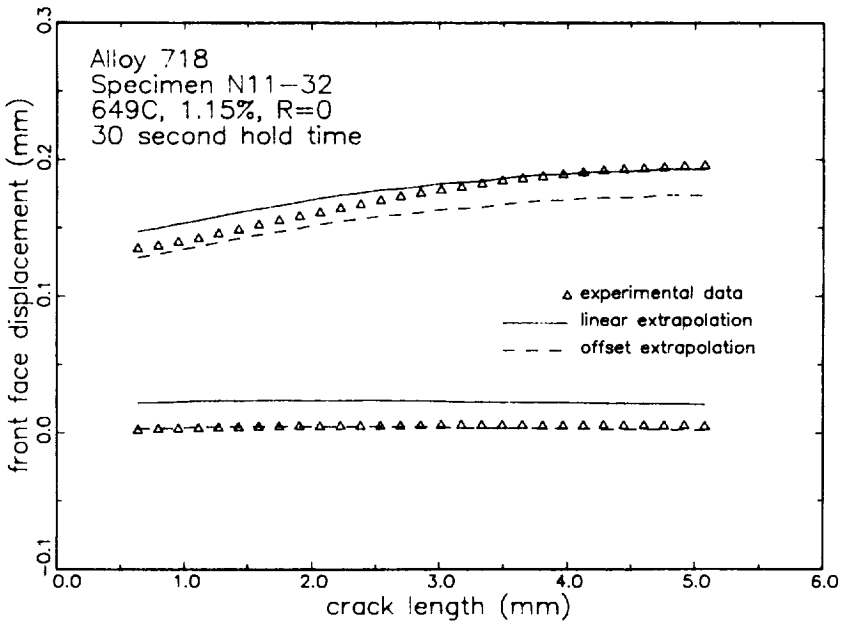

Figure 59. Comparison of Alloy 718 experimental front face displacements with the linear and offset extrapolation of remote displacements.

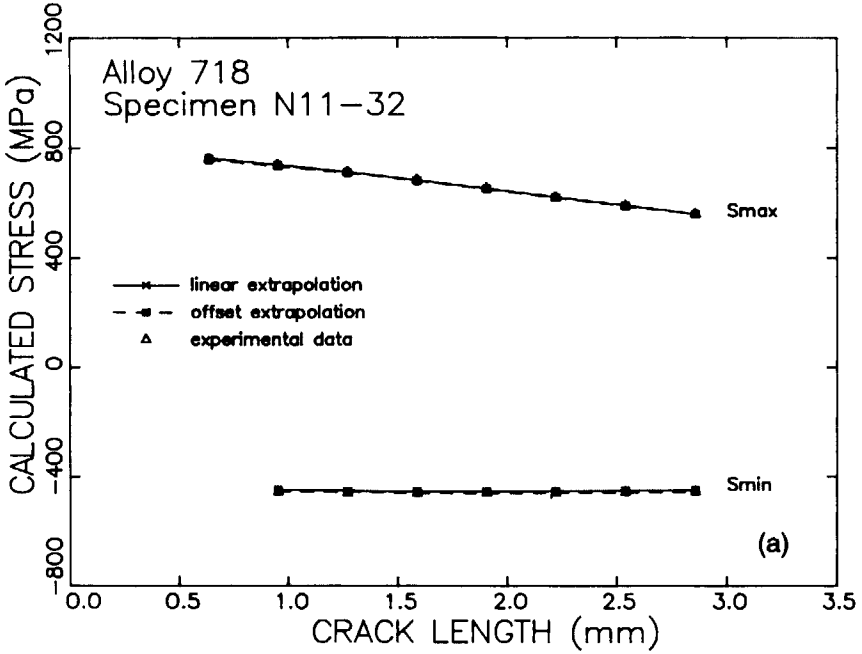

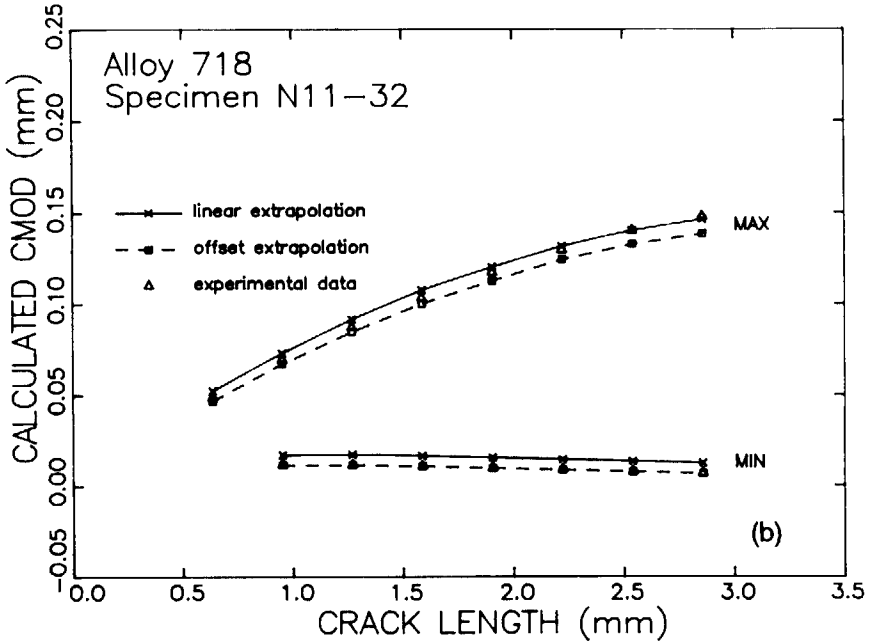

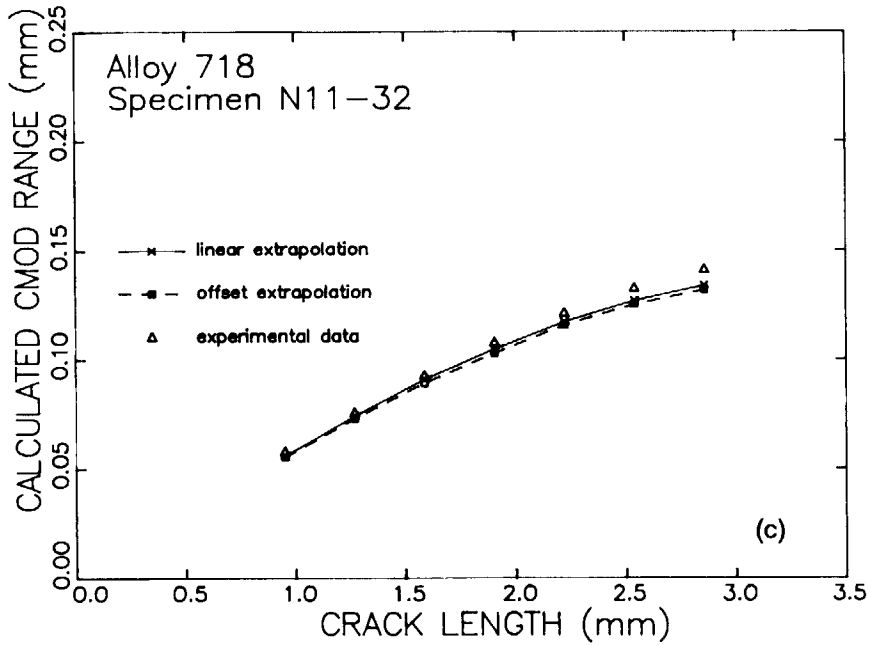

Figure 60. Comparison of predicted (a) stress, (b) CMOD, and (c) CMOD range in Alloy 718 with crack length for linear and offset extrapolation of remote displacement boundary conditions.

6.0 Crack Growth Under Static Loading Conditions

The objective of this task was to investigate if any of the non-rate or rate path-independent integrals reviewed in Section 2 are capable of correlating Alloy 718 crack growth data under static strain and stress conditions.

6.1 Crack Growth Test

The crack growth tests were performed on 12 SEN specimens. The test conditions are shown in Table 3. The load, control strain, back face strain, CMOD, and crack growth rates were measured during crack propagation. The control strain and the back face strain were used to provide boundary conditions for the analysis by linear extrapolation to the front face. The validity of the linear extrapolation boundary conditions was discussed in Section 5. The load and CMOD were used to verify the accuracy of the finite element analysis.

Table 3. Alloy 718 crack growth test conditions under static control.

Test Number	Temperature, °C	Strain or Load
N11-11	593	0.40%
N11-7	593	0.75%
N11-33	593	0.75%
N8-13	593	1.15%
N8-11	593	1.15%
N11-31	593	700 MPa
N8-15	649	0.40%
N11-45	649	0.75%
N11-3	649	0.75%
N11-10	649	1.15%
N11-1	649	1.15%
N8-4	649	700 MPa

The experimental crack growth rate was plotted against the stress intensity factor at 593°C and 649°C in Figure 61. Although the 593°C data appear to be correlated with K if the first data point and the data points after the maximum da/dt values are attained in each specimen are neglected, it is clear that the linear elastic fracture mechanics approach does not correlate the crack growth data at 649°C.

6.2 Finite Element Analysis of Crack Growth

The finite element analysis of the crack propagation was performed on all specimens except specimens N8-13 and N11-1. The finite element model used in the simulation of crack growth under

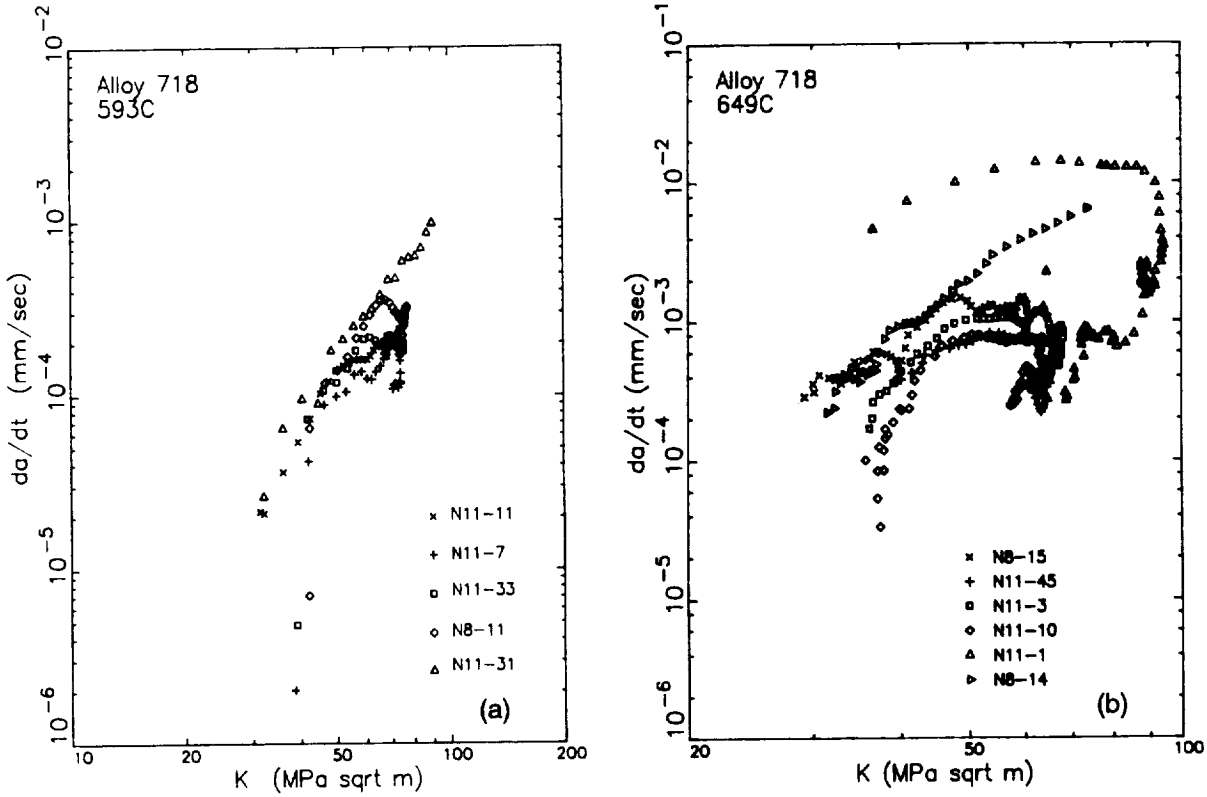

Figure 61. Correlation of Alloy 718 static crack growth data with stress intensity factor at (a) 593°C and (b) 649°C.

the static strain or static stress in this task is the same model used in the base program and shown in Figure 4. The initial crack tip location did not coincide with the position of a node on the crack plane in this model, so a minor adjustment of the nodal x-coordinate was made for each specimen to locate a node at the initial crack length. The initial crack tip was the fourth node from the crack mouth in all analyses. The boundary conditions were generated by linearly interpolating and extrapolating the control and back face strain measurements. The modeling method is schematically illustrated in Figure 62. The crack propagation was simulated in a series of strain (or stress) holds and crack tip node releases. For all constant strain analyses, two nodes were released at a time to save the computational time except the load case (LC) 3 where one node was released. The initial crack length was approximately 0.5mm and the final crack length was 2.54mm (a/W=0.25). The constant stress test at 649°C (specimen N8-14) did not have valid test data after the crack grew to 1.75mm, so the smaller increment of the crack length was used by releasing one node at a time. The total number of load cases was 16 for the constant strain cases and it was 18 for the case of specimen N8-14.

The P-I integrals computed are J*, $\hat{J}$, Tp* and their rate integrals. The rate quantities in the rate integrals were computed by dividing the difference of the quantities between two adjacent odd load cases (for instance LC=5 and LC=3) by the time required for the corresponding crack length increment in the experiment. The non-rate quantities in the rate integrals were averaged between the two load cases. The non-rate integrals were computed at the two load cases, then average values were

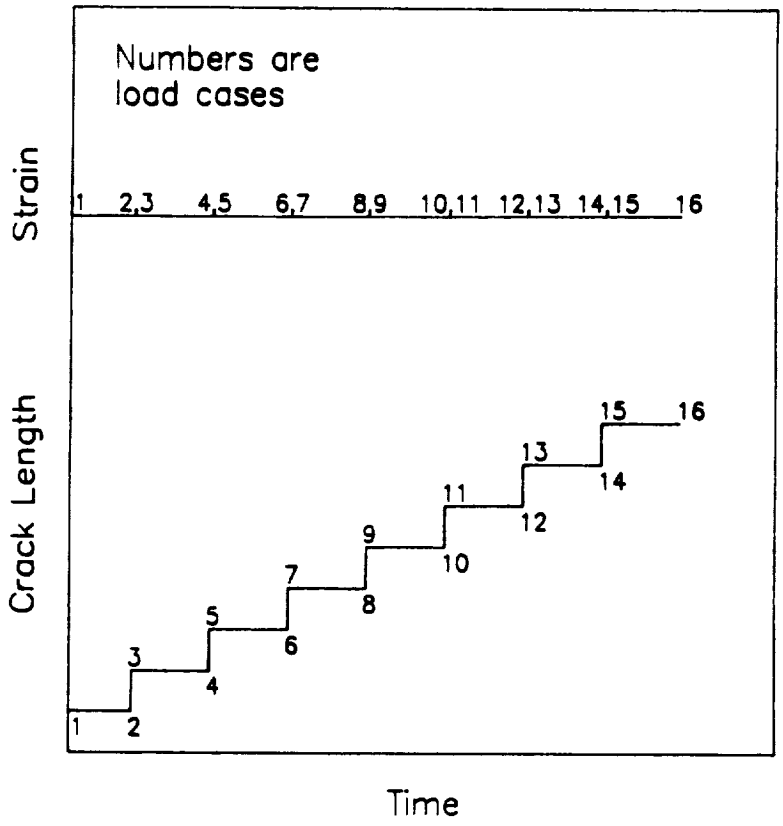

Figure 62. Schematic of the modeling scheme for Alloy 718 crack growth simulation under static control conditions.

taken. These values of non-rate and rate integrals were interpreted as those at the average crack length between the two load cases, and these values were used to correlate the crack growth rates at the average crack lengths.

It is also noted that the stress-strain curves used in these analyses were the monotonic stress-strain curves determined in the base program[1], because the specimens did not experience cyclic loading.

6.3 Results of Analysis

The typical crack profiles for constant strain and constant stress are shown in Figure 63. The waviness of the crack surface in Figure 63a is due to the simultaneous release of two nodes. A smoother crack profile is obtained if a node is released each time as shown in Figure 63b. The effect of the residual plasticity on the crack profile is clearly seen in these figures for both cases.

The variation of the average stress with crack length at 593°C and 649° C is plotted in Figure 64. The predicted stress was initially higher than the experimental data for constant strain cases, perhaps because the stress relaxation during initial loading was not accounted for in the analysis. The faster decrease of the predicted stress with crack length for the constant strain cases than the experimental stresses could result from the creep model used in the analysis. Nevertheless, the agreement between the experiment and prediction appears to be satisfactory. For the constant stress cases, the analyses were performed using the measured displacements as the boundary conditions, since the

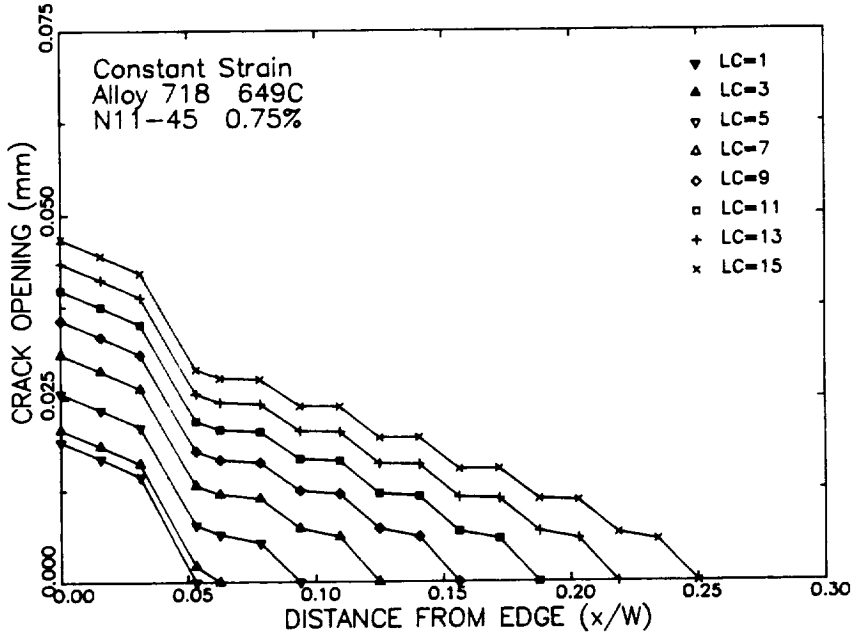

(a)

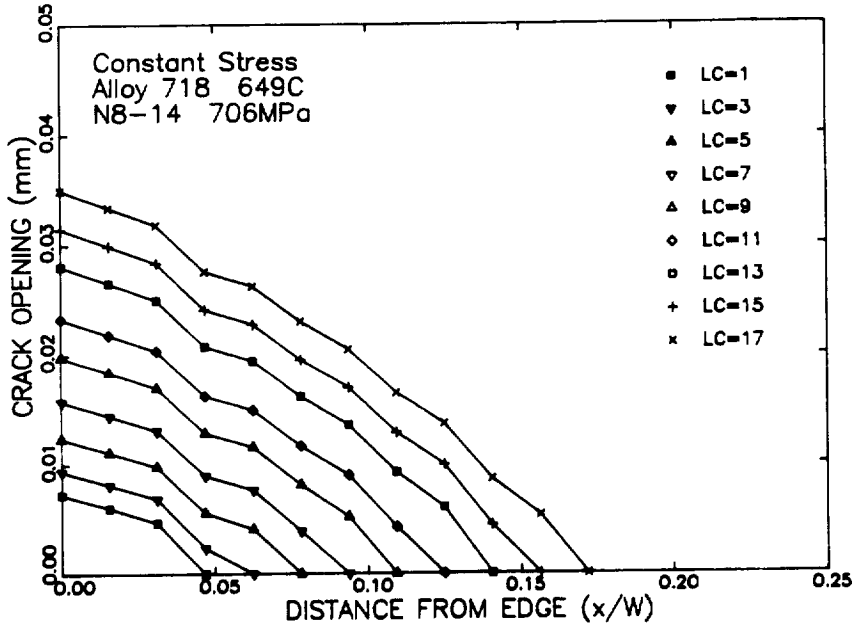

(b)

Figure 63. Predicted Alloy 718 crack profiles during crack propagation at 649°C under (a) 0.75% constant strain and (b) 706 MPa constant stress.

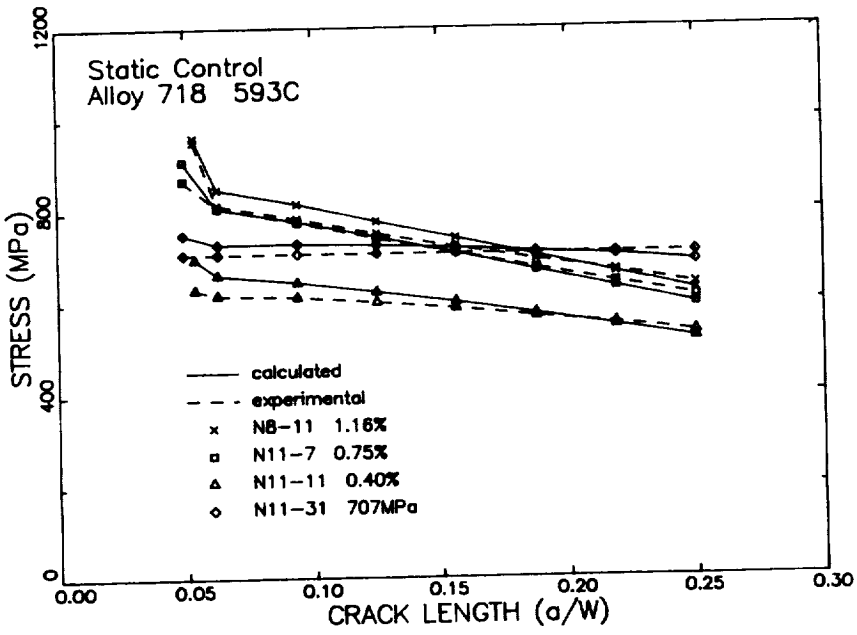

(a)

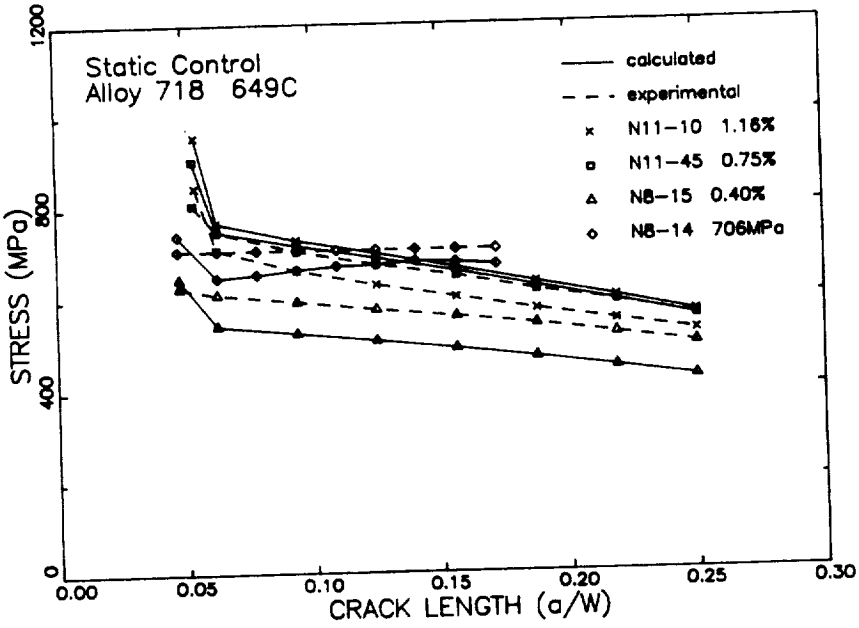

(b)

Figure 64. Variation of the average stress with crack length in Alloy 718 static loaded tests at (a) 593°C and (b) 649°C.

stress distribution on the model boundary was unknown. The calculated average stress was found to be slightly larger than the experimental data initially and became smaller as the crack propagated.

The predicted CMOD was also compared with the experimental results in Figure 65. The correlation looks quite good.

The calculated values of the non-rate and rate P-I integrals were plotted against equivalent distances in Figures 66 and 67, respectively for specimen N11-45. They appear to be path-independent. Similar degrees of path-independence were also observed for other cases.

The 593°C time-dependent crack growth data were correlated with the non-rate and rate integrals in Figures 68 and 69, respectively. Figures 70 and 71 show the correlation between the 649°C time-dependent crack growth data and the non-rate and rate integrals, respectively. The data in Figures 68 through 71 show that only two rate integrals, $\dot{J}^*$ and $\dot{\hat{J}}$, correlate the crack growth data, and all non-rate integrals and $\dot{T}p^*$ failed to normalize the data. It must also be noted at this point that the ΔTp-integral is not being evaluated any more, because the capability to correlate the constant temperature crack growth on Hastelloy-X (Section 4) was not as good as other parameters. The da/dt – $\dot{J}^*$ and da/dt – $\dot{\hat{J}}$ data at 593°C and 649°C were replotted in Figure 72 to inspect the temperature effect. Notice that the slopes at the two temperatures are almost identical and these lines are fairly close to each other.

Finally, it is noted that two specimens were analyzed with a single node release for each cycle in the analysis to see the effect of the node release method. Unlike the cases of time-independent deformation, there was a significant change in the values of the non-rate integrals. The rate integrals, however, did not change significantly. The non-rate integrals from the single node release analysis did not correlate the crack growth data, so the results obtained with two node release are still valid. The effect of the modeling scheme requires further investigation.

6.4 Conclusion

The conclusion of this task is that the rate P-I integrals $\dot{J}^*$ and $\dot{\hat{J}}$ can consolidate crack growth data under constant strain or constant load conditions. All non-rate integrals (J^*, $\hat{J}$ and Tp^*) and the rate integral $\dot{T}p^*$ failed in correlating the data.

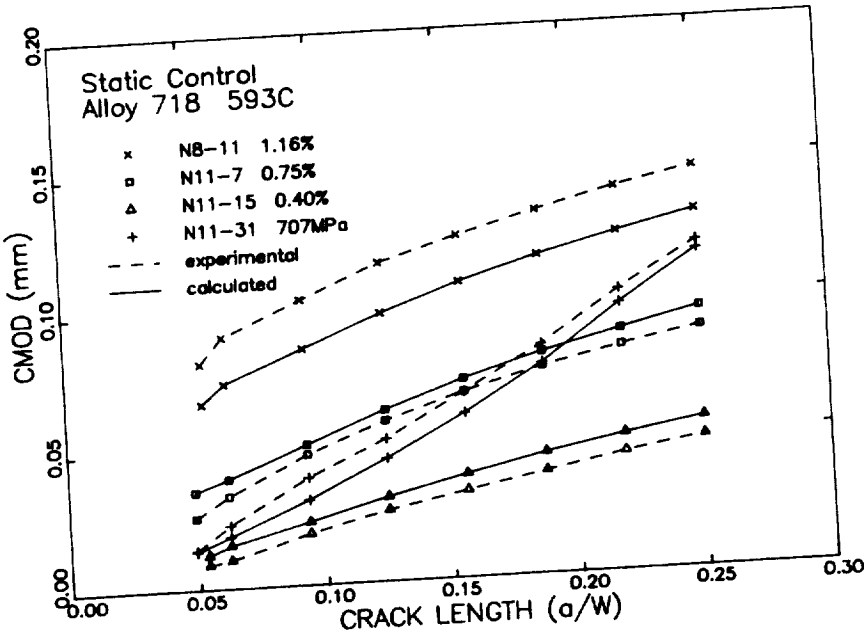

(a)

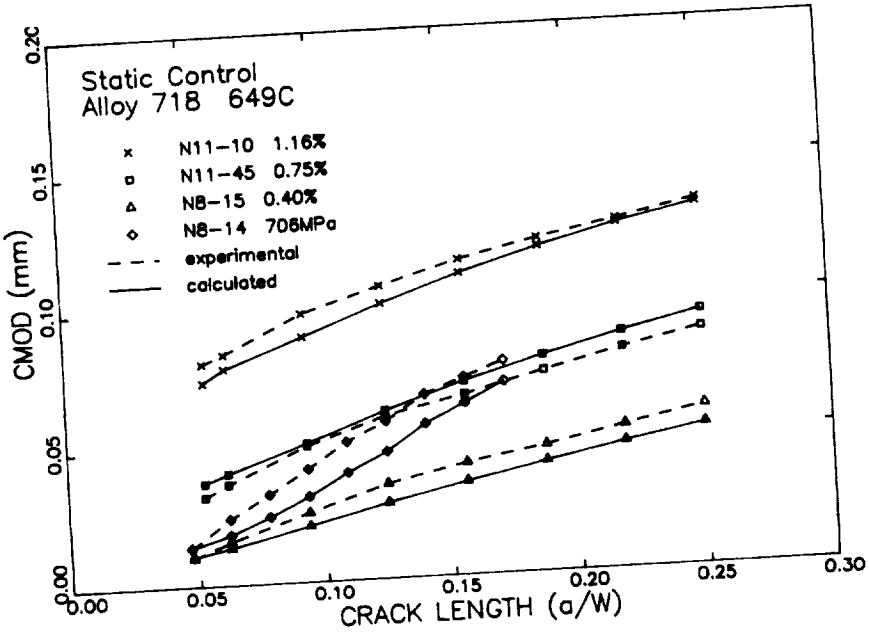

(b)

Figure 65. Variation of CMOD with crack length in Alloy 718 static loaded tests at (a) 593°C and (b) 649°C.

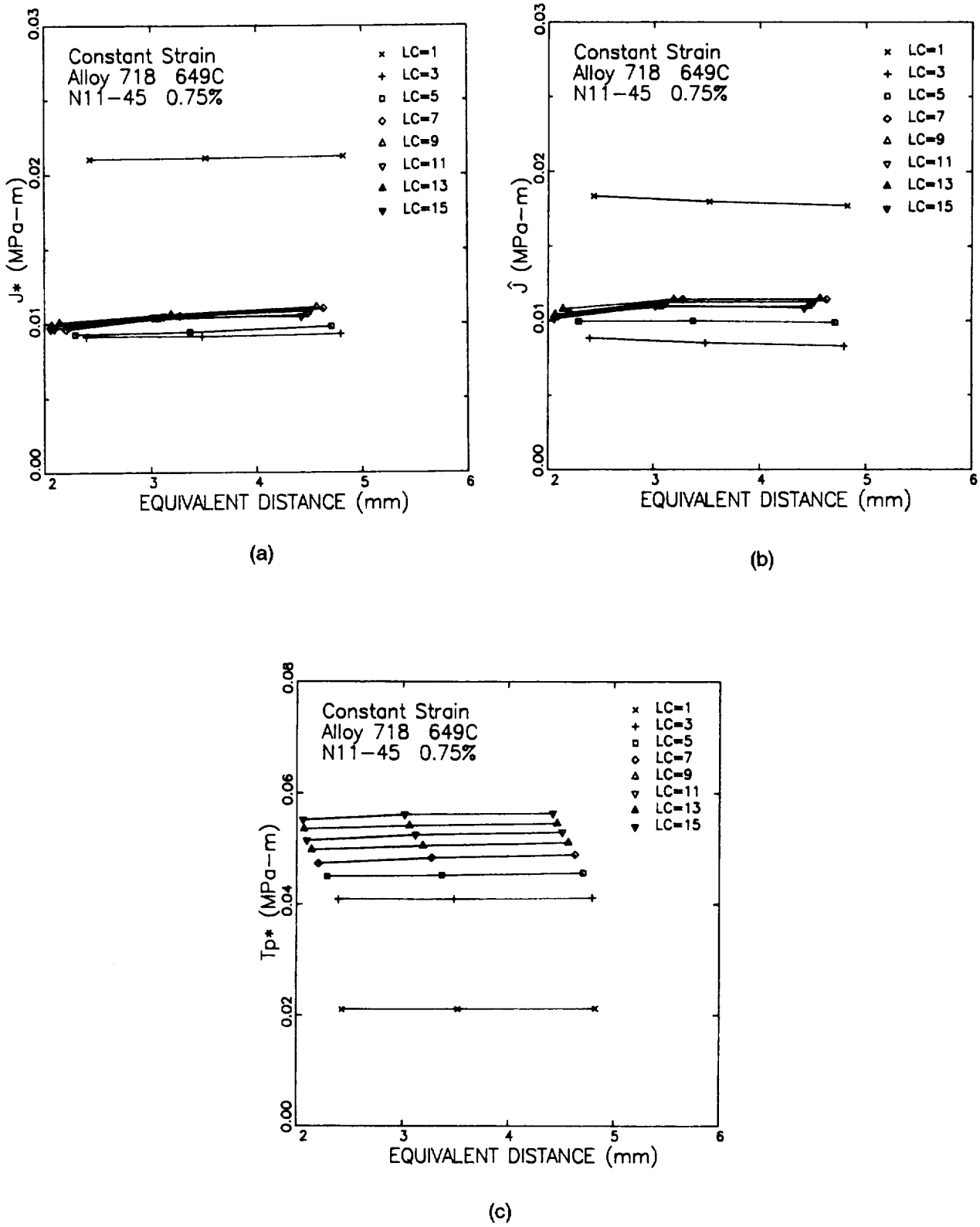

Figure 66. Variation of (a) J*, (b) $\hat{J}$, and (c) Tp* with path for Alloy 718 specimen N11–45.

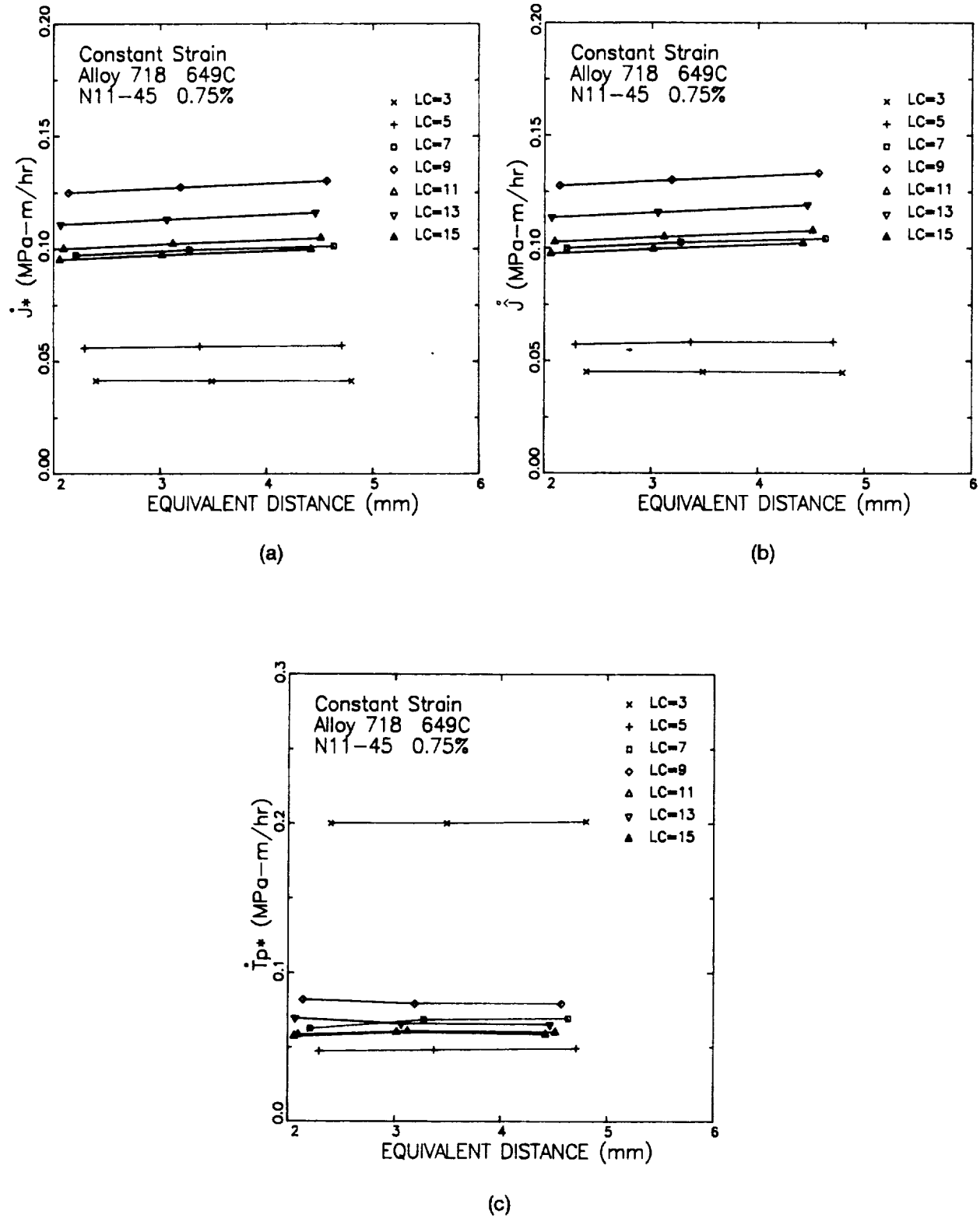

Figure 67. Variation of (a) $\dot{J}^*$, (b) $\dot{\hat{J}}$, and (c) $\dot{T}p^*$ with path for Alloy 718 specimen N11-45.

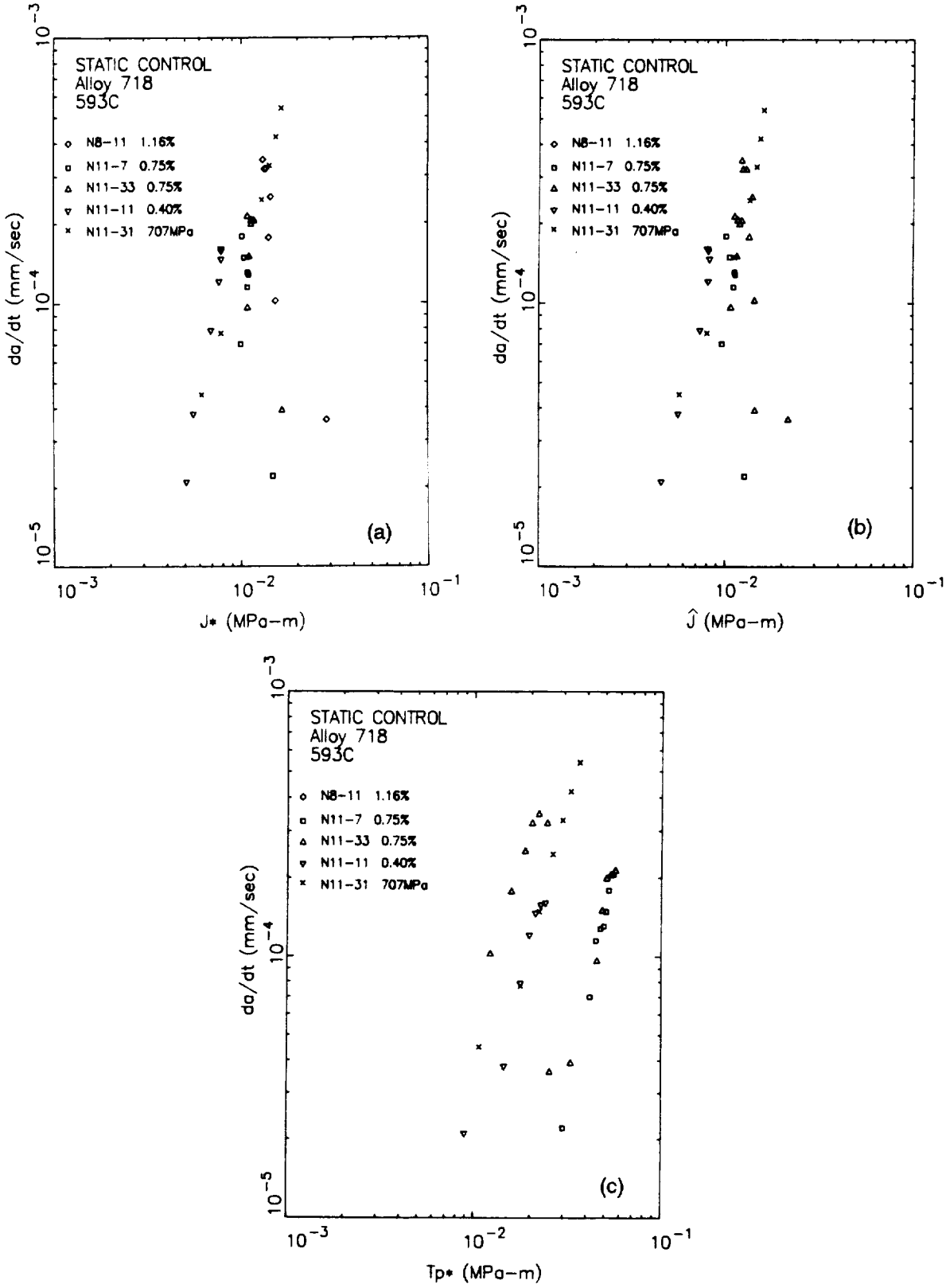

Figure 68. Variation of Alloy 718 time dependent crack growth rate at 593°C with (a) J*, (b) $\hat{J}$, and (c) Tp*.

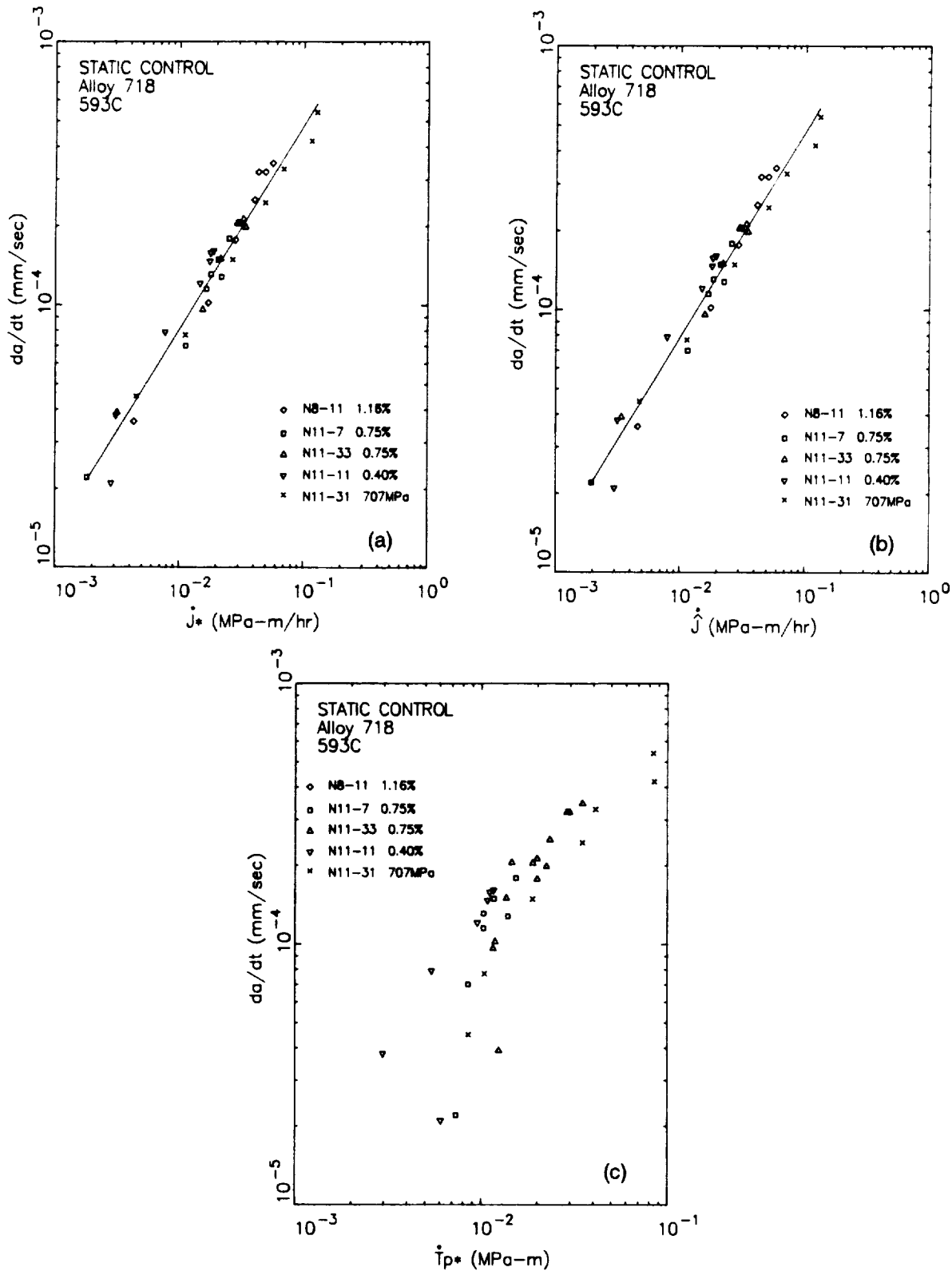

Figure 69. Variation of Alloy 718 time dependent crack growth rate at 593°C with (a) $\dot{J}^*$, (b) $\dot{\hat{J}}$, and (c) $\dot{T}p^*$.

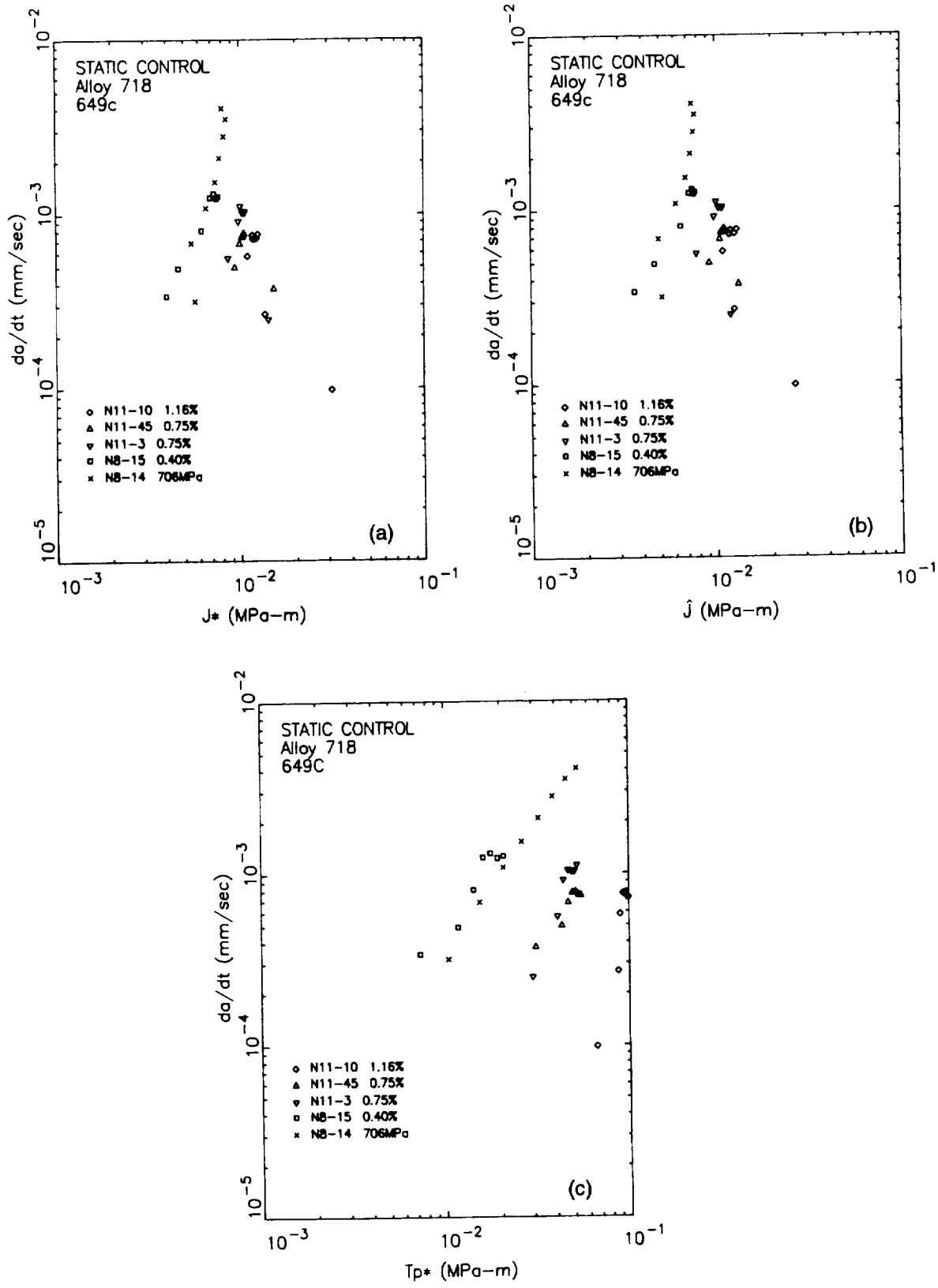

Figure 70. Variation of Alloy 718 time dependent crack growth rate at 649°C with (a) J*, (b) $\hat{J}$, and (c) Tp*.

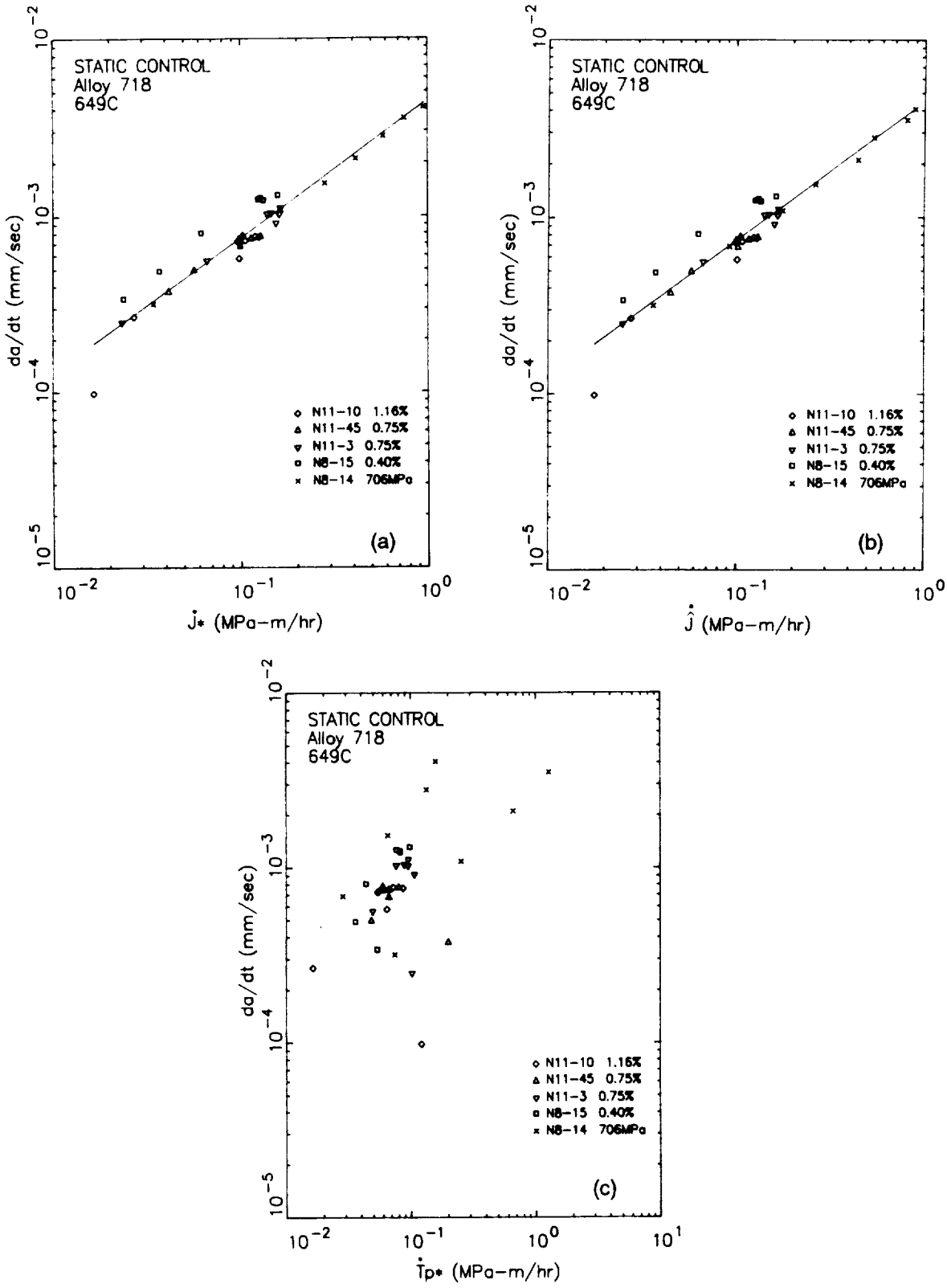

Figure 71. Variation of Alloy 718 time dependent crack growth rate at 649°C with (a) $\dot{J}^*$, (b) $\dot{\hat{J}}$, and (c) $\dot{T}p^*$.

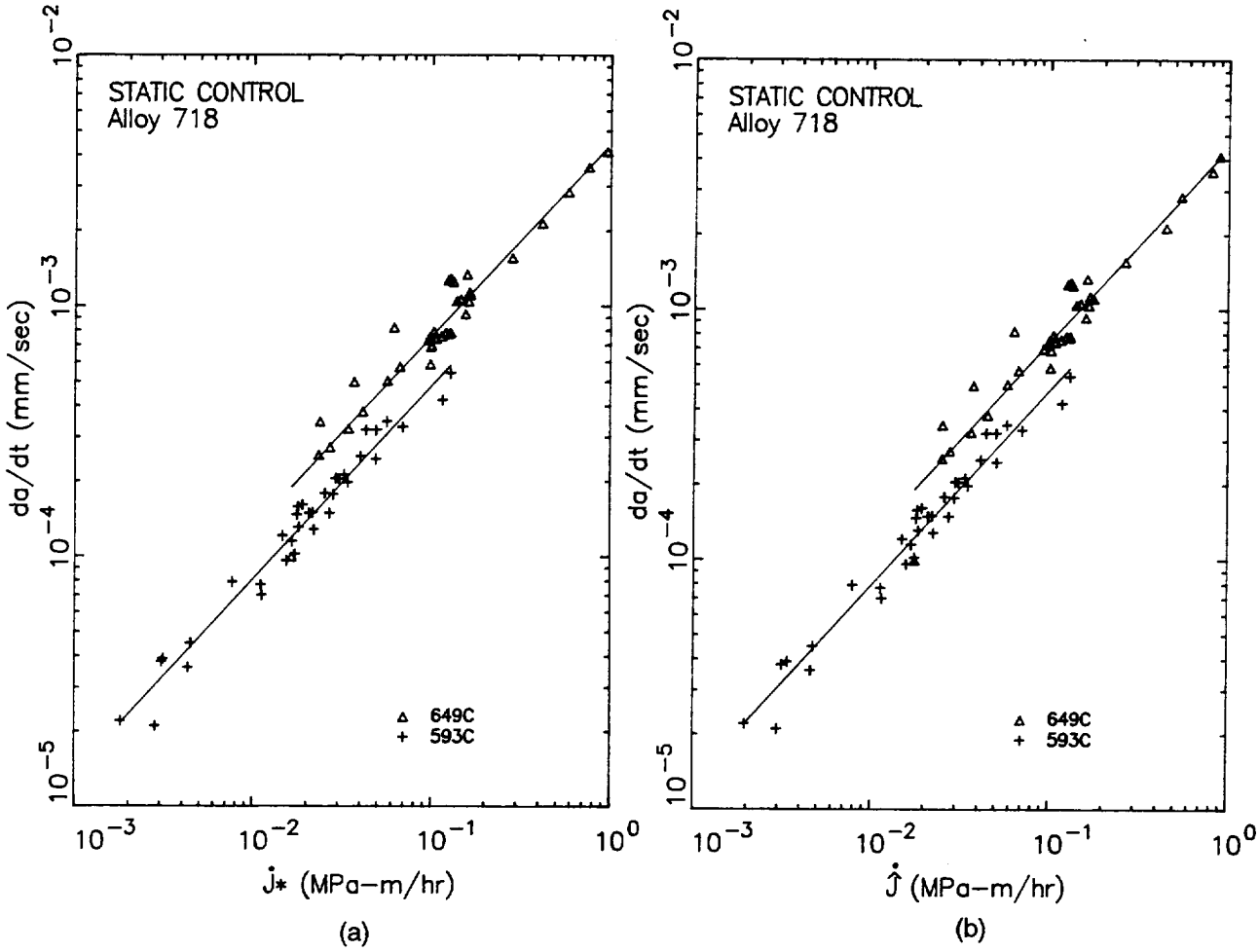

Figure 72. Comparison of Alloy 718 time-dependent crack growth rates at 593°C and 649°C with (a) $\dot{J}^*$ and (b) $\hat{\dot{J}}$.

7.0 Crack Growth Under Strain Cycling With Hold Time

The objective of this task was to investigate crack propagation behavior in Alloy 718 under isothermal strain cycling with hold time at the maximum strain. A finite element modeling scheme of crack growth in the presence of hold time was developed. Methods of crack growth prediction were studied based on the path-independent cyclic and rate integrals computed from the results of finite element analyses.

7.1 Crack Growth Test

The test conditions are shown in Table 4. As in other tasks, the measured variables were the load, control strain, back face strain, CMOD, and crack growth rates. The control strain and the back face strain were used to provide boundary conditions for the analysis by linear extrapolation to the front face. The load and CMOD were used to verify the accuracy of the analysis.

Table 4. Strain and temperature conditions for Alloy 718 hold time crack growth tests.

(R_ε = 0, 3 second loading ramp, 3 second unloading ramp)

Test Number	Temperature, °C	Strain Range	Hold Time at Maximum Strain, sec
N8-5	538	1.15%	300
N11-5	538	0.40%	300
N11-38	593	0.40%	0
N11-35	593	0.40%	30
N11-6	593	0.40%	300
N11-9	593	1.15%	0
N8-4	593	1.15%	30
N8-6	593	1.15%	300
N11-2	649	0.40%	0
N8-12	649	0.40%	30
N8-3	649	0.40%	300
N8-7	649	1.15%	0
N11-13	649	1.00%	30
N11-34	649	1.15%	300

The no-hold-time crack growth rates are plotted against the K_{max}, ΔK (from the minimum strain to the maximum strain), and ΔK_{eff} (from the crack opening point to the maximum strain) in Figures 73 and 74 for the 593°C and 649°C tests, respectively. None of these approaches are satisfactory over the whole range of data points. However, the ΔK and ΔK_{eff} approaches appear to correlate the

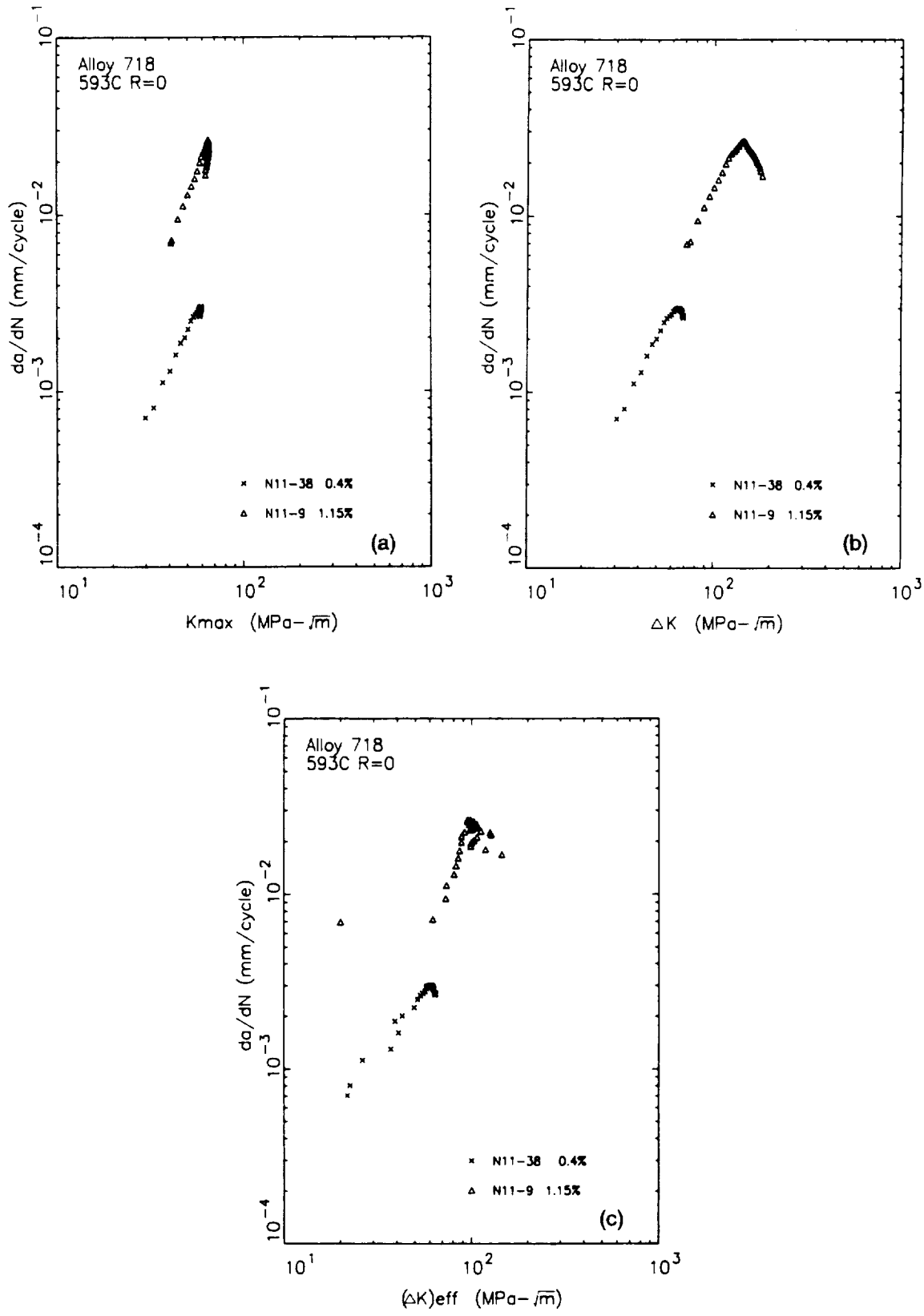

Figure 73. Variation of 593°C R_ε=0 Alloy 718 cyclic crack growth rates with (a) K_{max}, (b) ΔK, and (c) ΔK_{eff}.

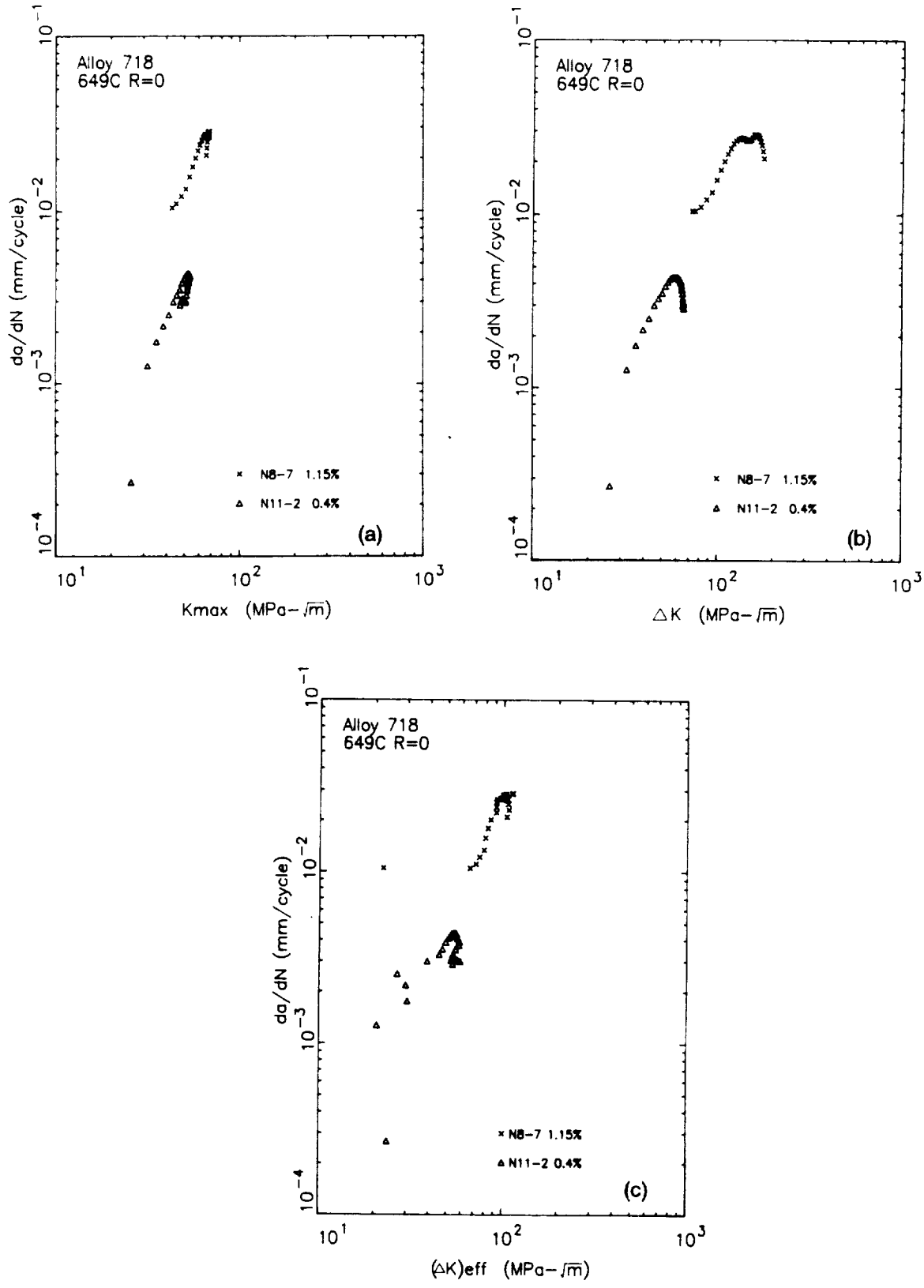

Figure 74. Variation of 649°C R_ε=0 Alloy 718 cyclic crack growth rates with (a) K_{max}, (b) ΔK, and (c) ΔK_{eff}.

crack growth data up to the crack length of 2.54mm. In most cases, the crack growth rate decreases at larger crack lengths. Much of the scatter of data points in the ΔK_{eff} approach is due to the difficulty in determination of the crack opening point at small crack lengths when the load-CMOD data is almost linear.

7.2 Finite Element Analysis of Crack Growth

The finite element analysis of crack propagation under the loading conditions in the present task is more complicated in nature, and only an approximate analysis is possible unless one attempts a precise modeling by increasing the crack size during the strain ramp and hold time separately for each test cycle. In the analysis with a pre-determined crack size increment for a given finite element model, an analysis cycle was comprised of more than one experimental cycle. In this circumstance, a question is raised on how to represent the hold time for more than one experimental cycle in a single analysis cycle. An easily conceivable method is to use the total hold time of the experimental cycles for the crack length increment in the analytical model. This method was used in this investigation. The modeling scheme constitutes four load cases in a cycle: (1) load up to the maximum strain, (2) hold the strain, (3) release crack tip nodes, and (4) load down to the minimum strain. These steps are repeated until the crack length reaches 2.54mm. The variation of the applied control strain and the crack length with load cases in this scheme is depicted in Figure 75. For the specimens with no hold time (specimens N8-7, N11-2, N11-38 and N11-9), the second step was deleted, thus the scheme reduces to that of the isothermal modeling in the base program. Two nodes were released in each cycle as in analyses in other tasks, except the first cycle where one node was released only because the initial crack position, taken from experimental data, was approximately one node away from the next crack size (0.635mm) taken in the analyses throughout this program. The coordinate of the initial crack tip node was adjusted to the experimental initial crack size. The total load cases were 22 for no hold time analyses and 29 for hold time analyses.

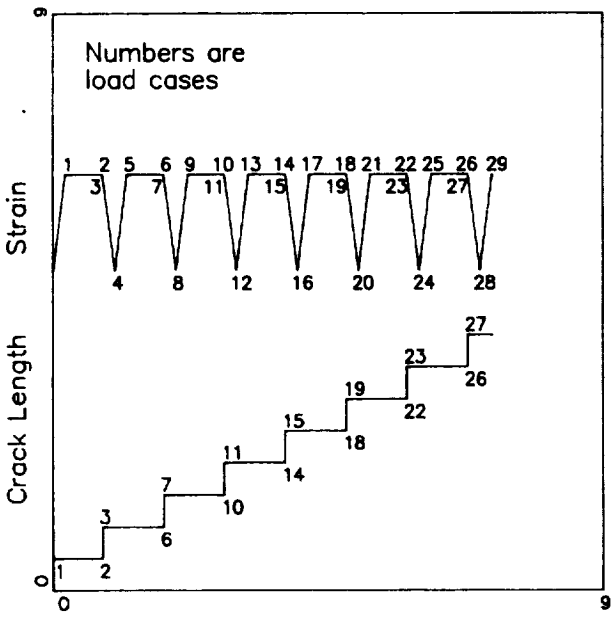

Figure 75. Schematic of the modeling scheme for Alloy 718 crack growth simulation under strain cycling with hold time.

7.3 Prediction of Crack Growth Rate

The results of other tasks lead to the conclusion that the path-independent integrals and rate-integrals that are most likely to correlate the hold time crack growth data are the following two pairs of integrals:

1. The J*-integral and its rate integral
2. The $\hat{J}$-integral and its rate integral.

These integrals were computed based on the finite element analysis results. The increments of J* and $\hat{J}$ from the minimum strain to the maximum strain (say, from load case 4 to load case 5) were used to estimate crack growth due to strain cycling from the da/dN versus ΔJ_x data obtained from no hold time cases. The average value of the rate integral during hold time was approximately

calculated from the field data at two adjacent load cases at the maximum strain (say, load case 5 and load case 1). The rate quantities were computed by dividing the difference of the variable between the two load cases by the hold time for this cycle (say hold time for load case 2). The crack growth during hold time was then estimated from the static test data (Section 6) using these rate integrals. It is noted that crack growth during an experimental cycle is partially occurring during hold time and partially during strain cycling. The test data indicate that crack growth in a cycle is more likely to occur during hold time as the applied strain, temperature and hold time increase. In this task, attempts were made to correlate the crack growth data using the superposition method[22] and modifications of that approach.

7.4 Results of Analysis

The average stress (total load divided by the cross section of the uncracked specimen) versus crack length is plotted at minimum and maximum strain in Figures 76 and 77 for the 593°C and 649°C tests, respectively. The calculated maximum and minimum stresses are shifted to the compressive direction at $\Delta\varepsilon$=0.4% at both temperatures. At $\Delta\varepsilon$=1.15% the prediction of the maximum stress appears satisfactory, however the minimum stress is less compressive contrary to the trend at $\Delta\varepsilon$=0.4%. These phenomena occur from the initial crack length and remain so until the final crack length. It might perhaps reflect the transient stress-strain behavior of this material while the finite element analysis implemented the cyclically stable stress-strain curve. The CMOD range was somewhat underpredicted at $\Delta\varepsilon$=0.4% and slightly overpredicted at $\Delta\varepsilon$=1.15% as shown Figures 78 and 79 for the 593°C and 649°C tests, respectively.

The continuously cycled (zero hold time) crack growth data are plotted against ΔJ^* and $\Delta\hat{J}$ at in Figures 80 and 81 for the 593°C and 649°C tests, respectively. It appears that if the straight lines fitting the individual sets of data points are drawn, they will be separated by some distance. However, all these data points can also be correlated by a straight line with a smaller value of slope within a reasonable accuracy. Similar trend was also observed in some Hastelloy-X data analyzed in Section 5. An inspection of the test data shows that the crack growth rate and the stress intensity factor decreases somewhat for each specimen at crack lengths larger than the final crack size in the analysis. Therefore, the deviation of the data points from the straight line would not increase, if it does so, significantly at larger crack lengths. These straight lines were used to calculate the crack growth rate due to strain cycling for hold time analyses. Both ΔJ^* and $\Delta\hat{J}$ correlated the data reasonably well. It must also be mentioned that the ranges of ΔJ^* and $\Delta\hat{J}$ used in these figures are from the minimum strain to the maximum strain. Two closure analyses performed on specimens N11-38 and N8-7 at the final crack length in the analysis (a=2.54mm) indicated that the values of J^* and $\hat{J}$ are very small at the minimum strain, the crack closing and opening points compared to those at the maximum strain. Therefore, the values of ΔJ^* and $\Delta\hat{J}$ used in these figures can also be interpreted as those from the crack opening point to the maximum strain. This was also true for R_ε=-1 loading as discussed in[1]. It would be interesting to investigate what happens if R_ε becomes positive.

The da/dt versus rate integrals are given in Figure 72. The crack growth rate prediction was performed by three methods. In the first method, the superposition method employed in Reference[22] was used. This method is given by

$$(da/dN)_{ht} = (da/dN)_{cy} + (da/dN)_{st} \qquad (32)$$

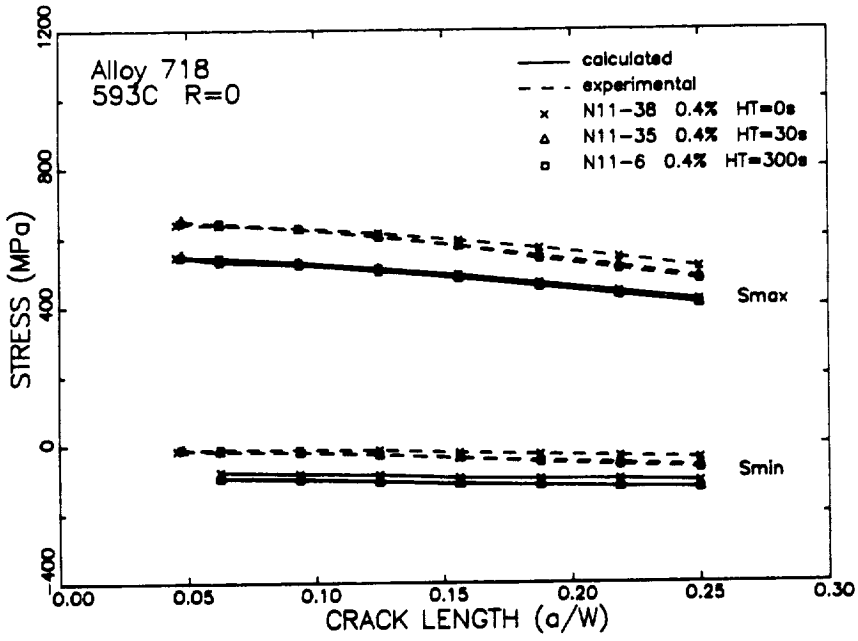

(a)

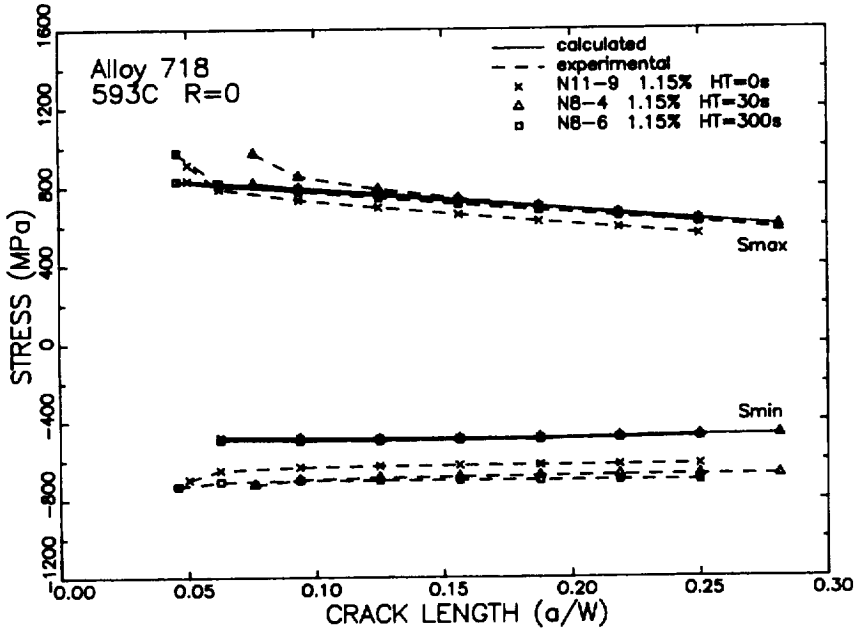

(b)

Figure 76. Variation of the average stress with crack length for R_ε=0 593°C Alloy 718 hold time tests with $\Delta\varepsilon$ of (a) 0.4% and (b) 1.15%.

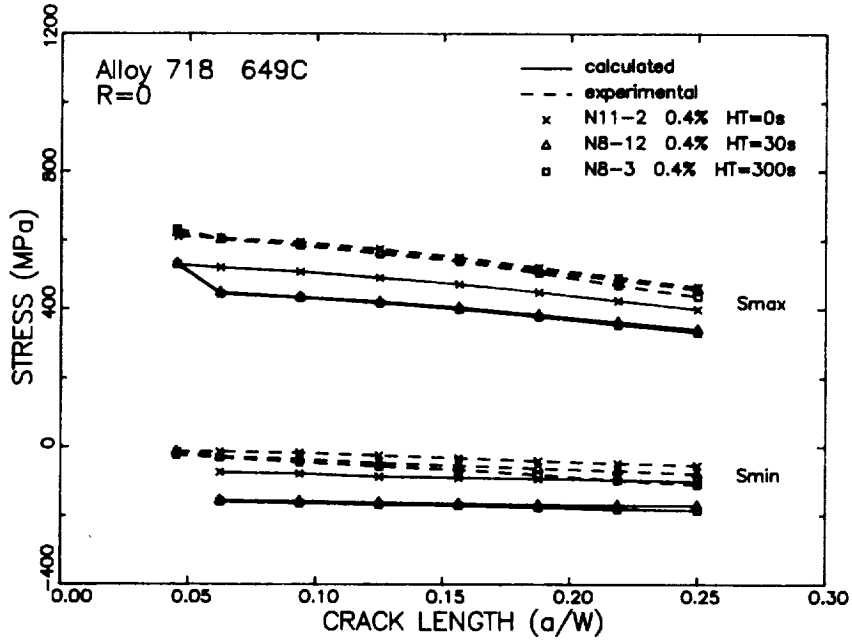

(a)

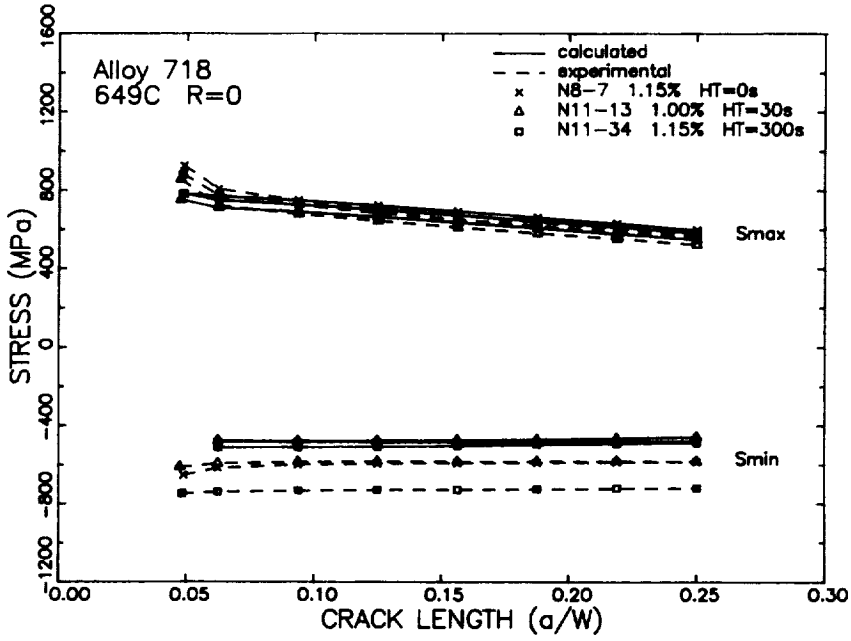

(b)

Figure 77. Variation of the average stress with crack length for R_ε=0 649°C Alloy 718 hold time tests with $\Delta\varepsilon$ of (a) 0.4% and (b) those greater than 1.00%.

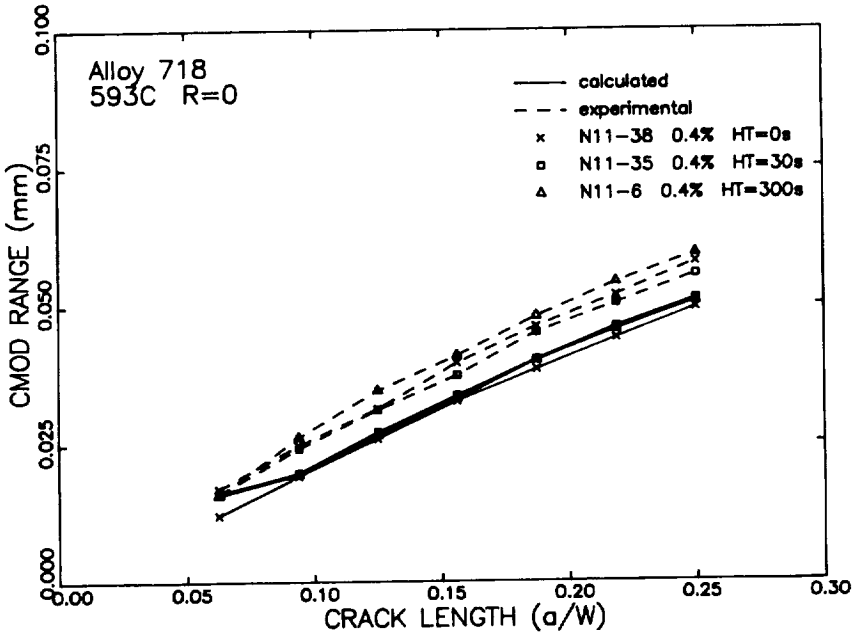

(a)

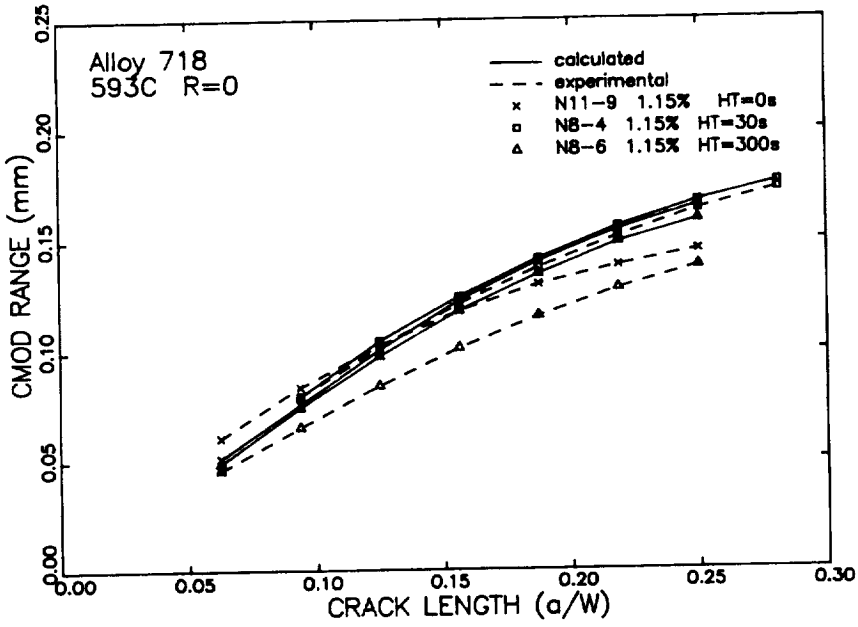

(b)

Figure 78. Variation of the CMOD range with crack length for R_ε=0 593°C Alloy 718 hold time tests with $\Delta\varepsilon$ of (a) 0.4% and (b) 1.15%.

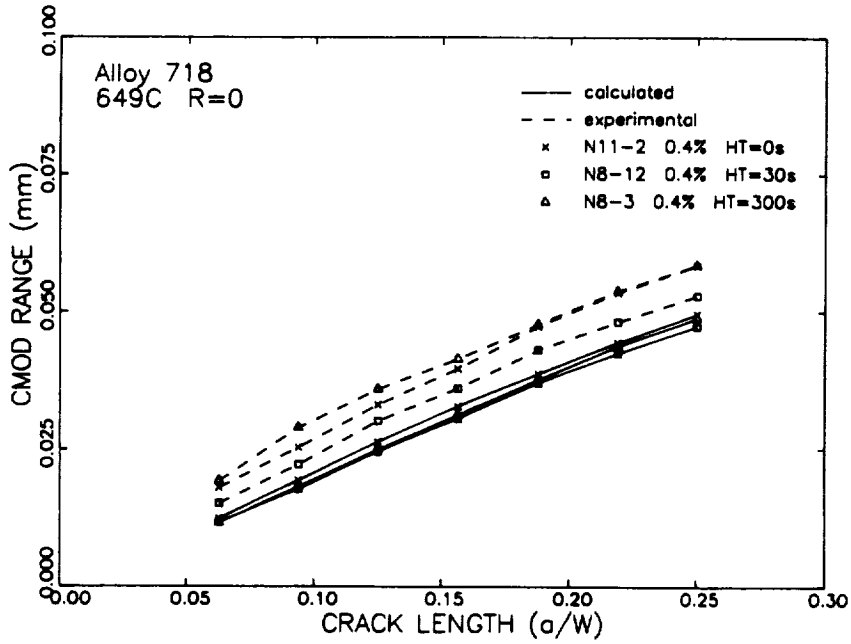

(a)

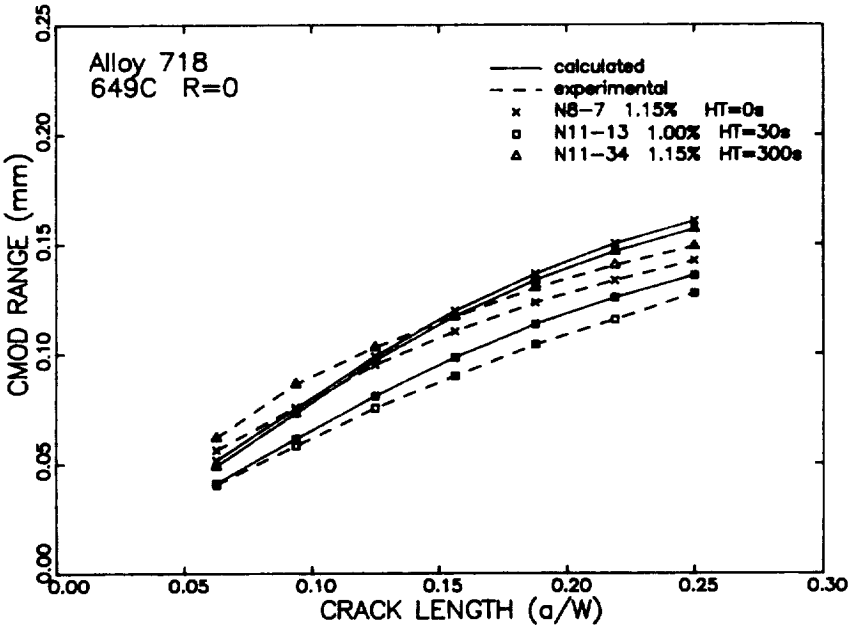

(b)

Figure 79. Variation of the CMOD range with crack length for R_ε=0 649°C Alloy 718 hold time tests with $\Delta\varepsilon$ of (a) 0.4% and (b) those greater than 1.00%.

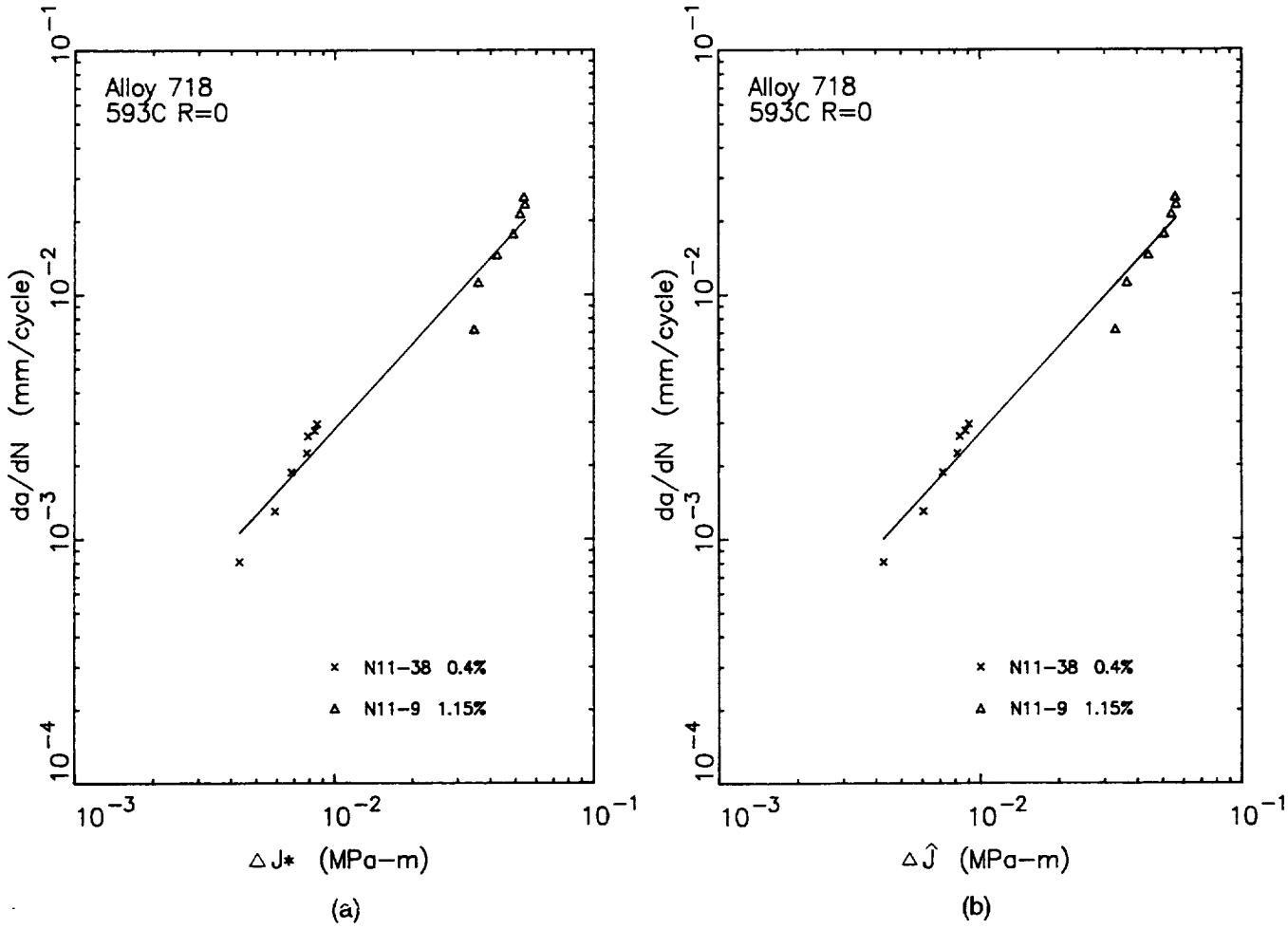

Figure 80. Correlation of Alloy 718 cyclic crack growth data at 593°C, R_ε=0 with (a) ΔJ^* and (b) $\Delta\hat{J}$.

where

$$(da/dN)_{st} = (da/dt) \cdot t_h \tag{33}$$

The subscripts "ht", "cy" and "st" represent, respectively, the total crack growth rate during strain cycling with a hold time (t_h), the cyclic crack growth rate determined from da/dN – ΔJx data, and the crack growth data during hold time determined from da/dt – $\dot{J}$x data obtained in static tests.

The predicted and experimental $(da/dN)_{ht}$ for the $\hat{J}$ and J* parameter systems using the superposition are compared in Figures 82 and 83 for the 593°C and 649°C tests, respectively. In these figures, the solid line indictes perfect correlation and the dashed lines enclose a region within a factor of two of perfect correlation. It is apparent that the superposition method works well at small applied strains, but it overpredicts crack growth at large strains.

A modification of the superposition method was developed to better correlate the data over the lower and higher strain ranges. This method was conceived after evaluating several approaches. It is given by

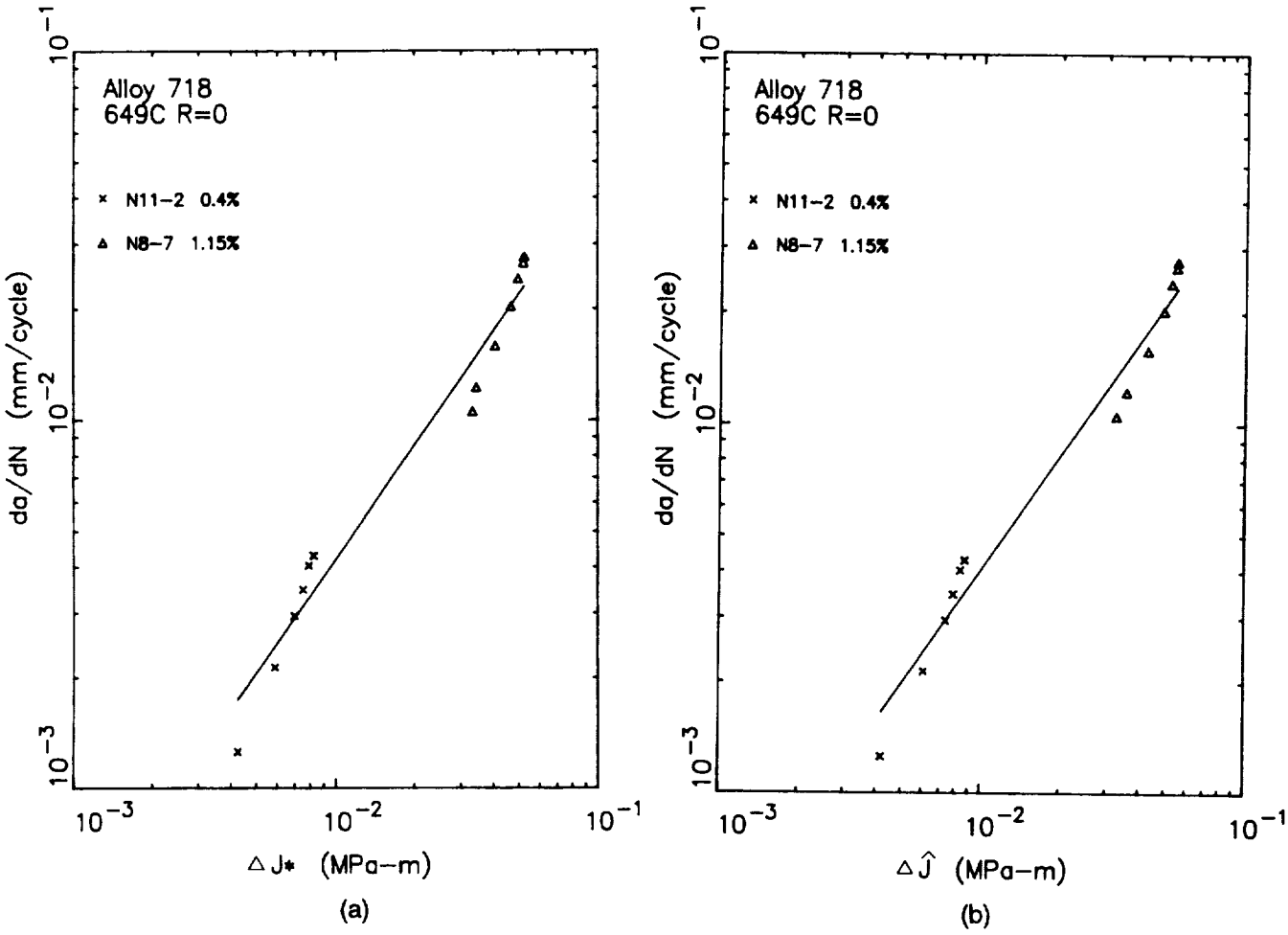

Figure 81. Correlation of Alloy 718 cyclic crack growth data at 649°C, R_ε=0 with (a) ΔJ^* and (b) $\Delta\hat{J}$.

$$(da/dN)_{ht} = (da/dN)_{cy} + \beta(da/dN)_{st} \tag{34}$$

where $0 \le \beta \le 1$.

β is a function of the maximum strain, hold time and temperature, i.e.,

$$\beta = \beta(\varepsilon_{max}, t_h, T) \tag{35}$$

The constant β was determined to minimize the standard deviation between the predicted and experimental crack growth data for individual specimens. The predicted and experimental $(da/dN)_{ht}$ for the $\hat{J}$ and J* parameter systems using the modified superposition model are compared in Figures 84 and 85 for the 593°C and 649°C tests, respectively. The lines in these figures have the same meaning as those previously described for Figures 82 and 83. The modified superposition method yielded good correlation over the strain levels tested. The variation of β with hold time and maximum strain is shown in Figures 86 for both temperatures. The lines in the Figure 86 were estimated from data points. Obviously, many tests are needed to establish the data base for β. It is observed from these figures that β decreases as the maximum strain increases. Also, it is obvious that β must approach unity if hold time becomes larger, since this is the case of crack growth under static strain.

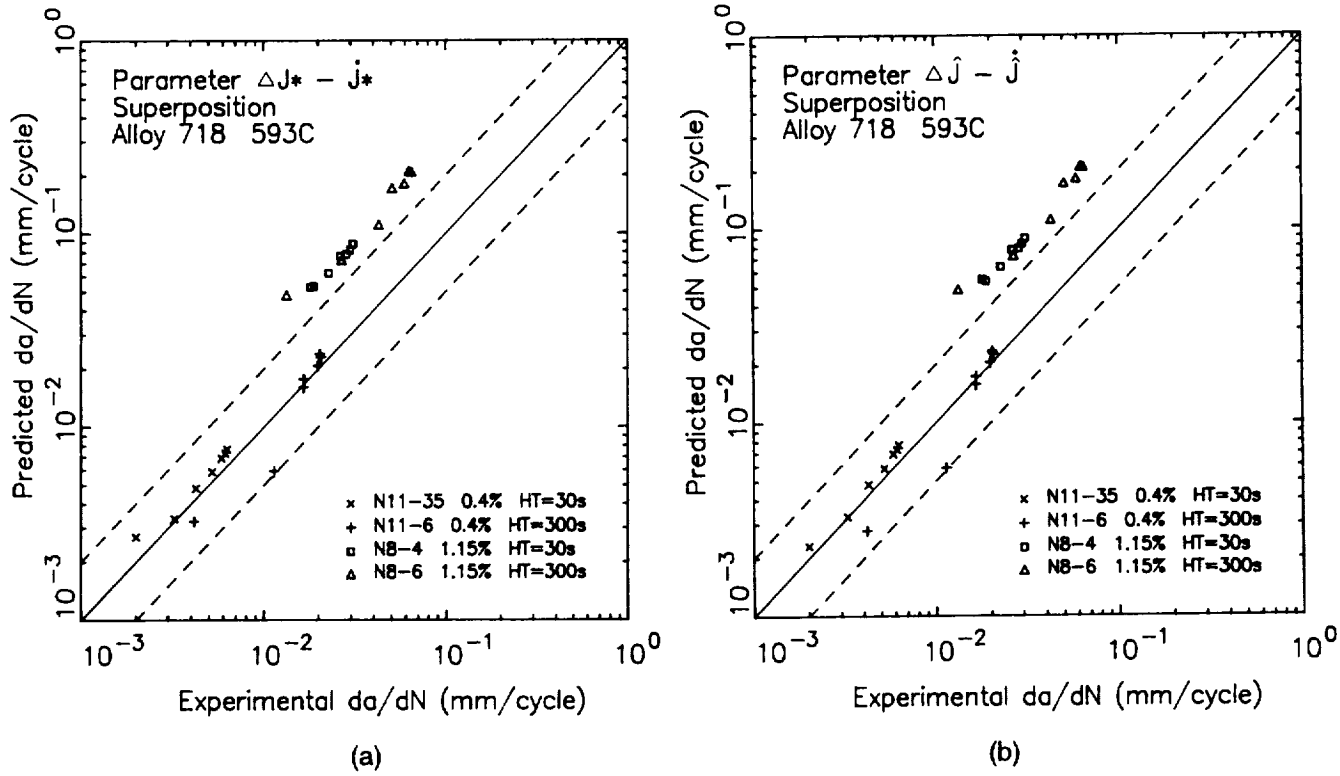

Figure 82. Comparison of experimental and predicted Alloy 718 hold time crack growth data at 593°C using (a) $\Delta J^* - \dot{J}^*$ and (b) $\Delta\hat{J} - \dot{\hat{J}}$ superposition methods.

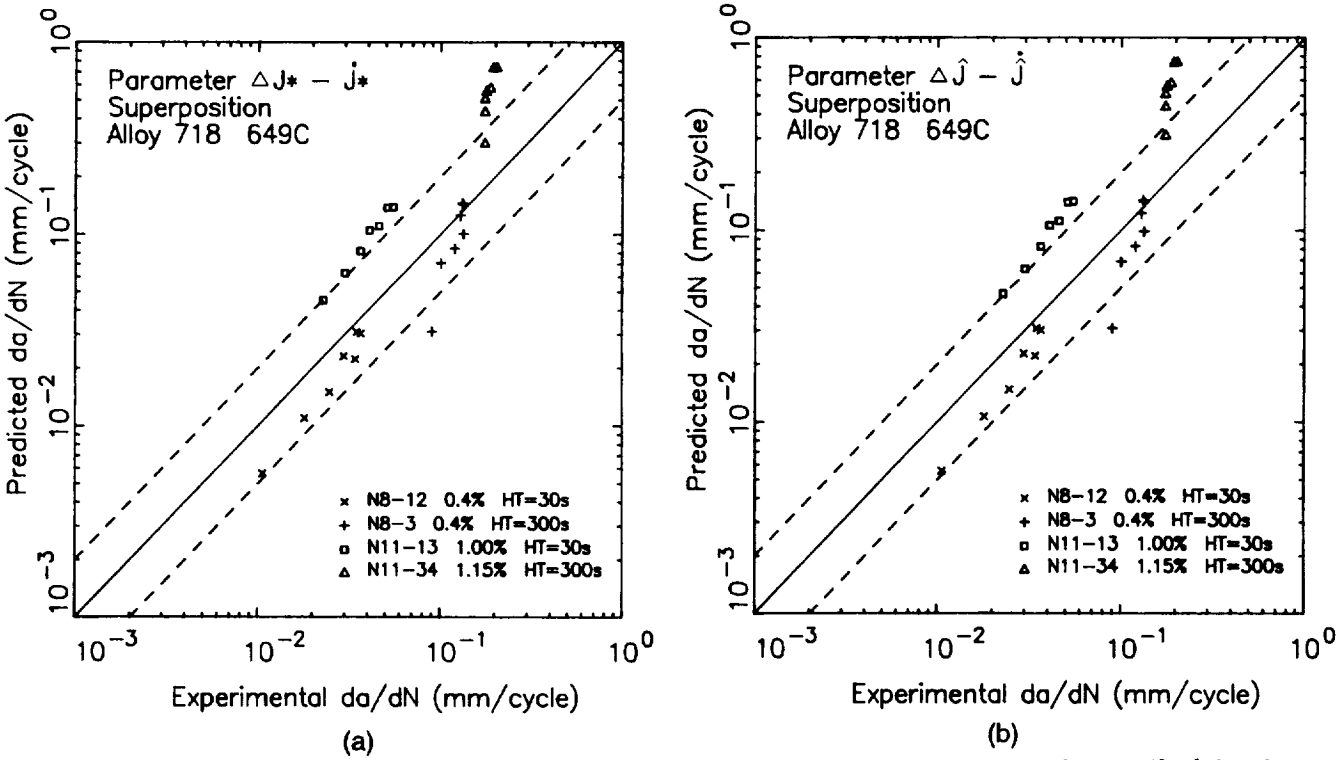

Figure 83. Comparison of experimental and predicted Alloy 718 hold time crack growth data at 649°C using (a) $\Delta J^* - \dot{J}^*$ and (b) $\Delta\hat{J} - \dot{\hat{J}}$ superposition methods.

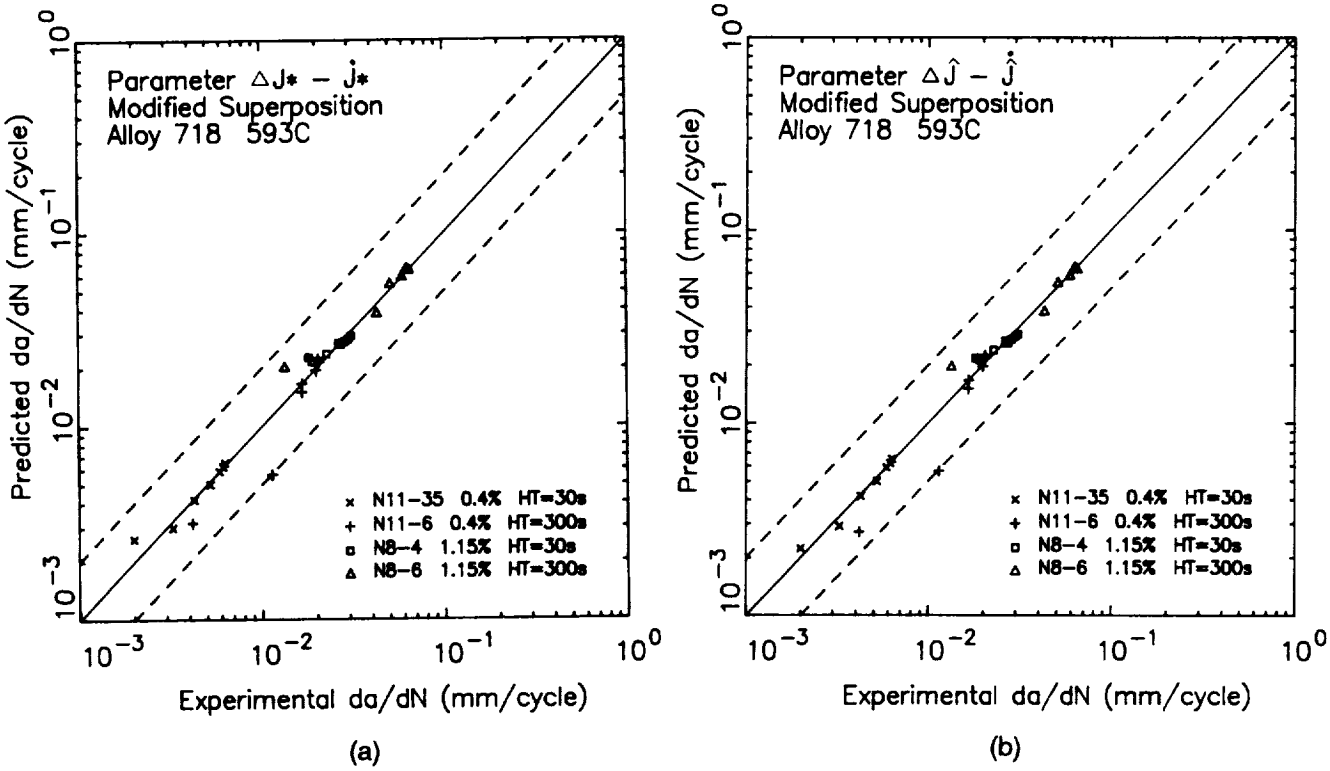

Figure 84. Comparison of experimental and predicted Alloy 718 hold time crack growth data at 593°C using (a) $\Delta J^* - \dot{J}^*$ and (b) $\Delta\hat{J} - \dot{\hat{J}}$ modified superposition methods.

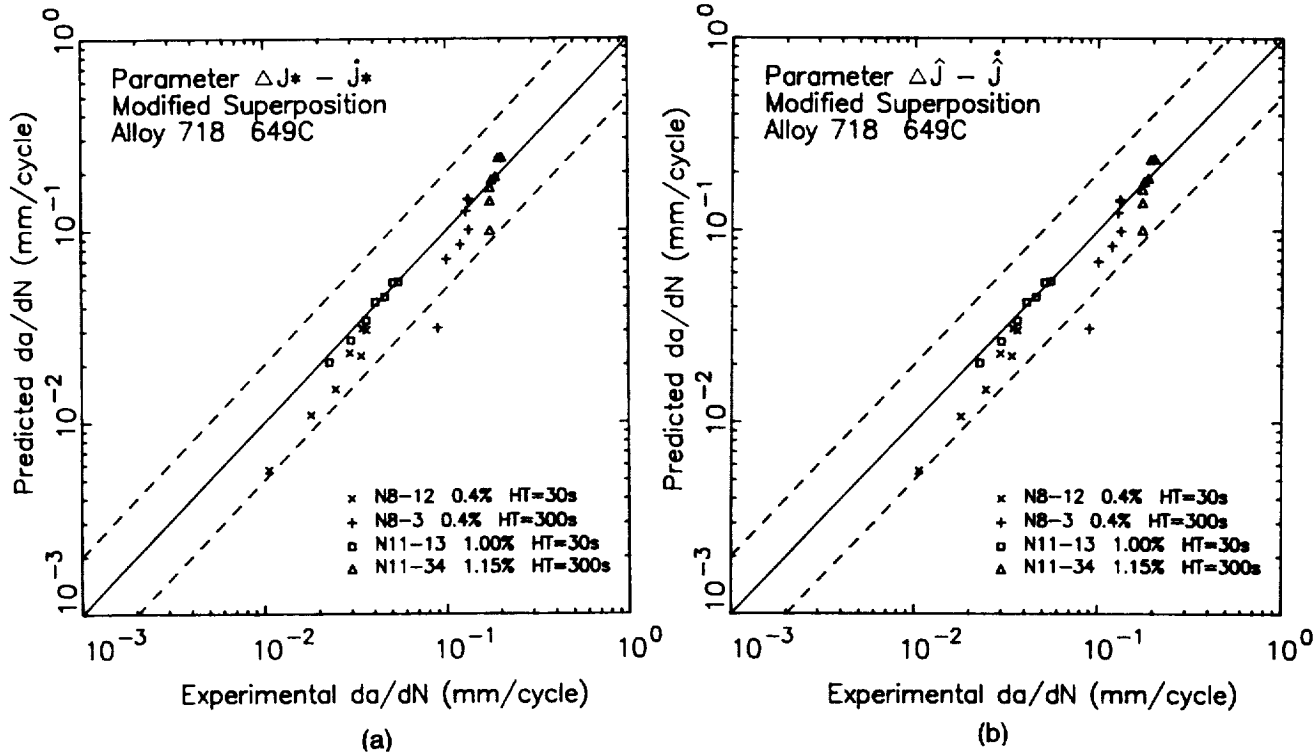

Figure 85. Comparison of experimental and predicted Alloy 718 hold time crack growth data at 649°C using (a) $\Delta J^* - \dot{J}^*$ and (b) $\Delta\hat{J} - \dot{\hat{J}}$ modified superposition methods.

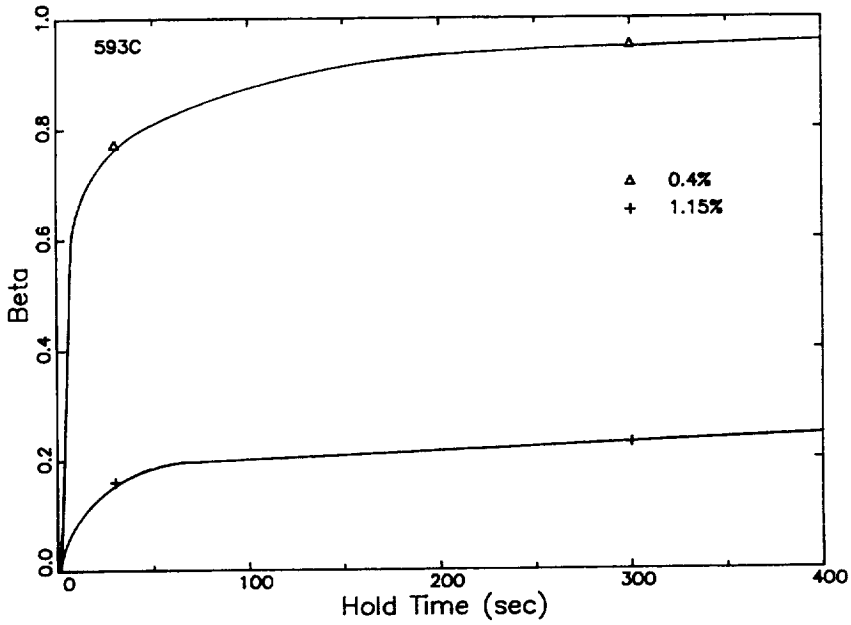

(a)

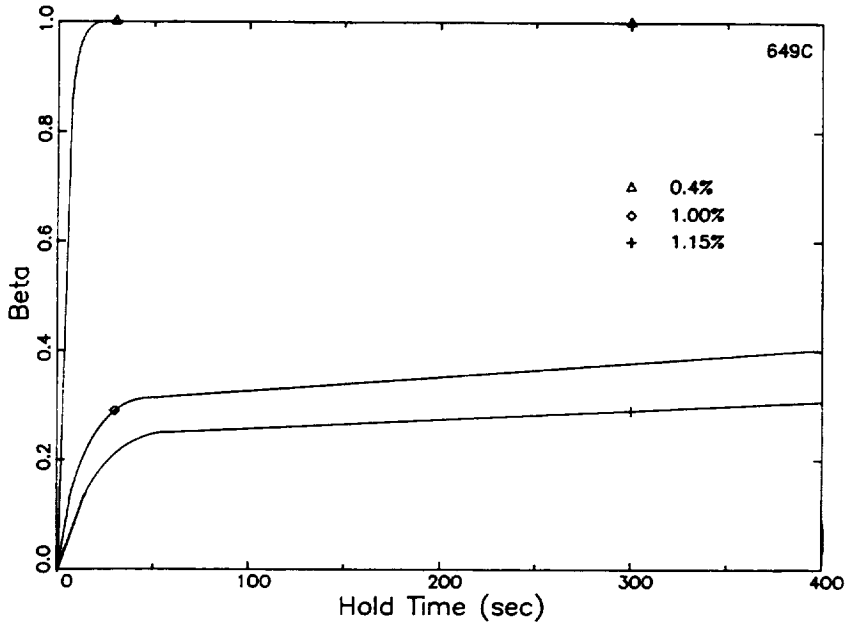

(b)

Figure 86. Variation of β in Alloy 718 as a function of hold time and ε_{max} at (a) 593°C and (b) 649°C.

It is noted that the performance of these methods of crack growth prediction may vary with the scheme of simulating crack growth in the finite element analysis and the way the integral parameters are computed. Therefore, it is suggested that the new method must be used as a package with the finite modeling scheme of crack propagation used in this section. It is also noted that the crack growth prediction during strain (or stress) cycling with hold time based on the present scheme of finite element analysis necessitates the advanced knowledge on the total hold time for the crack length increment in the model, which can be known only if the number of cycles required for the crack length increment is estimated. Therefore, an iterative numerical scheme must be developed in which the finite element analysis interacts with crack growth criteria. This iterative scheme must also be used for purely static loading for the same reason.

7.5 Conclusion

The applicability of path-independent integrals for prediction of crack growth under elementary loading conditions such as isothermal cyclic loading and static loading have been established in other tasks. In this task, the ability of path-independent integrals to correlate crack growth was further verified for R=0 strain cycling at 593°C and 649°C. The nature of the main work in this task was different in that this task is an application of the results obtained in elementary loading conditions (isothermal strain cycling and static loading) to develop a method of predicting crack growth in a more complicated loading condition (isothermal strain cycling with hold time). It was found that the simple superposition method based on the $\Delta J^* - \dot{J}^*$ or $\Delta\hat{J} - \hat{\dot{J}}$ is valid only for small strain cycles. A modified superposition method was proposed for both small and large strain cycles.

8.0 Crack Growth Under Thermomechanical Fatigue Loading With Hold Time

The objective of this task was to investigate crack propagation behavior in Alloy 718 under combined thermomechanical fatigue (TMF) cycling with with hold time at either the maximum or minimum strain.

8.1 Crack Growth Test

The test conditions are shown in Table 5. The TMF cycling was performed using the same method as previously described in the base program[1]. All tests were performed with $R_\varepsilon = 0$ or zero minimum strain. The strain range listed in Table 5 is both the maximum mechanical strain and the mechanical strain range. As in other tasks, the measured variables were the load, control strain, backface strain, CMOD, and crack growth rates. The results of these tests were analyzed using linear elastic fracture mechanics parameters, but FEM crack growth simulations and P–I integral evaluations were not performed.

8.2. Crack Growth Results

Figure 87 shows the results for the TMF tests which were cycled continuously (no hold time). These results are qualitatively similar to the results for the previous TMF tests. The previous tests were performed with $R_\varepsilon = -1$ (zero mean strain) while the tests shown in Figure 87 were performed with $R_\varepsilon = 0$. The crack growth rates measured in the in–phase tests at different strain ranges were not well correlated with linear elastic fracture mechanics indicating the need for non–linear fracture

Table 5. Strain and temperature conditions for Alloy 718 TMF/hold time crack growth tests.

(R_ε = 0, 427°C to 649°C
50 Second Loading Ramp, 50 Second Unloading Ramp)

Test Number	Strain Range (%)	Hold Time (sec, strain level)	TMF Description
N8–8	0.40	0	in–phase
N11–4	1.15	0	in–phase
N11–39	0.40	300 Maximum	in–phase
N11–40	0.40	300 Maximum	in–phase
N11–37	1.15	300 Maximum	in–phase
N11–44	1.15	300 Maximum	in–phase
N8–9	0.40	300 Zero	in–phase
N11–41	1.15	300 Zero	in–phase
N8–1	1.15	0	out–of–phase
N8–10	1.15	300 Maximum	out–of–phase
N11–43	1.15	300 Zero	out–of–phase

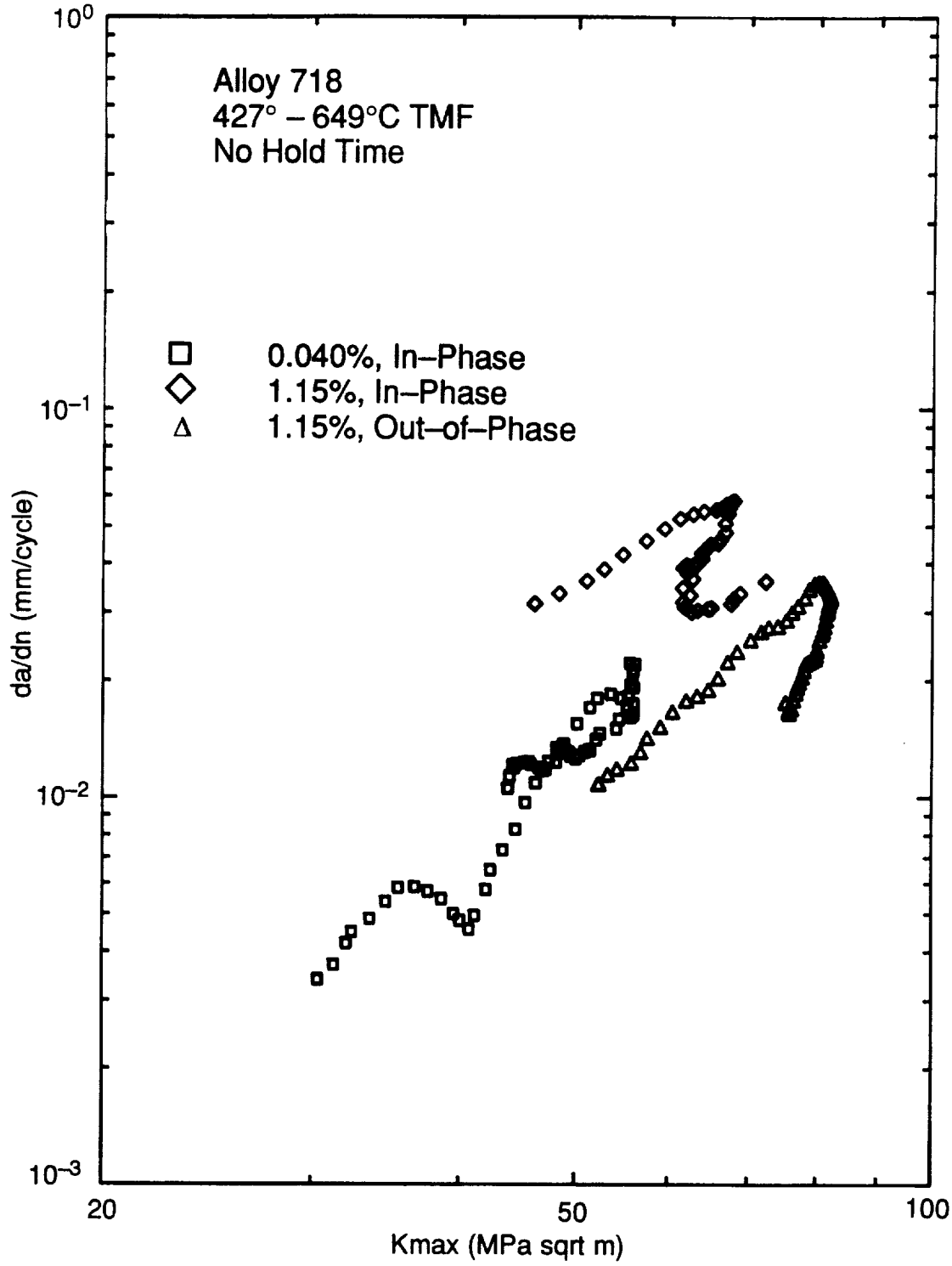

Figure 87. Variation of Alloy 718 crack growth rate with K_{max} for continuously cycled R_ε= 0 427°–649°C TMF tests..

mechanics approach to adequately model these results. At the higher strain range, crack growth in the in–phase test exceeded those in the out–of–phase tests. This is anticipated because the temperature at maximum stress in the in–phase tests was 649°C while the temperature at maximum stress in the out–of–phase tests was 427°C. Experience from isothermal tests show that crack growth response increases with increasing temperature.

The results of the 0.4% strain range in–phase TMF tests are shown in Figure 88. The crack growth rates from the continuously cycled test and 300 second hold time at zero strain hold time are very similar. The temperature during this hold time was 427°C. Based on Alloy 718 static and hold time tests at 593° and 649°C[22], very little time–dependent crack growth would be anticipated at 427°C. In addition, the load during this hold time was compressive. As a result, the hold time at zero strain would not be expected to accelerate the crack growth rate.

This is not the case for the hold time at maximum strain in the in–phase tests where the temperature during the hold time is 649°C and hold time occurs ant the maximum strain in the loading cycle. The static and hold time tests in this program show that significant amounts of static crack growth occur under these types of conditions. The 649°C hold time at maximum stain greatly accelerated the crack growth rate in the TMF tests. This is observed for tests with 0.4 and 1.15% strain ranges as shown in Figures 88 and 89, respectively.

The results of the out–of–phase tests are fairly similar whether there is no hold time, hold time at maximum strain, or hold time at minimum strain as shown in Figure 90. This results because when the hold time loads are tensile, the temperature during the hold time is 427°C where little time–dependent crack growth will occur. The loads are compressive for the 649°C hold time at minimum load so there in no driving force to cause crack growth.

These results are qualitatively similar to those shown independently for TMF and isothermal time–dependent crack growth tests. Both of those conditions have been successfully modeled with P–I integrals, so it would be anticipated that these could also be modeled successfully.

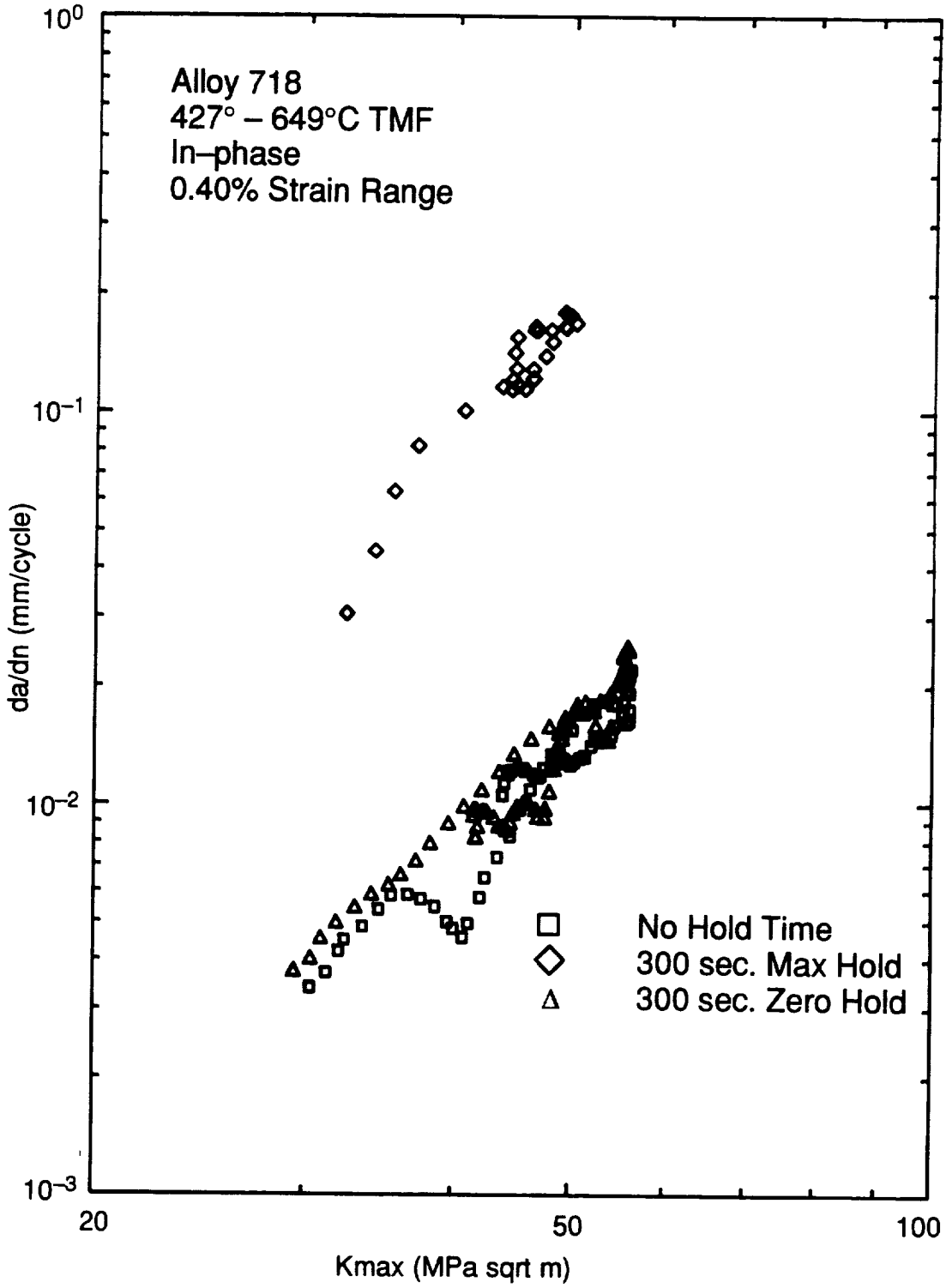

Figure 88. Variation of Alloy 718 crack growth rate with K_{max} for In–phase R_ε= 0 427°–649°C TMF tests with a mechanical strain range of 0.40%.

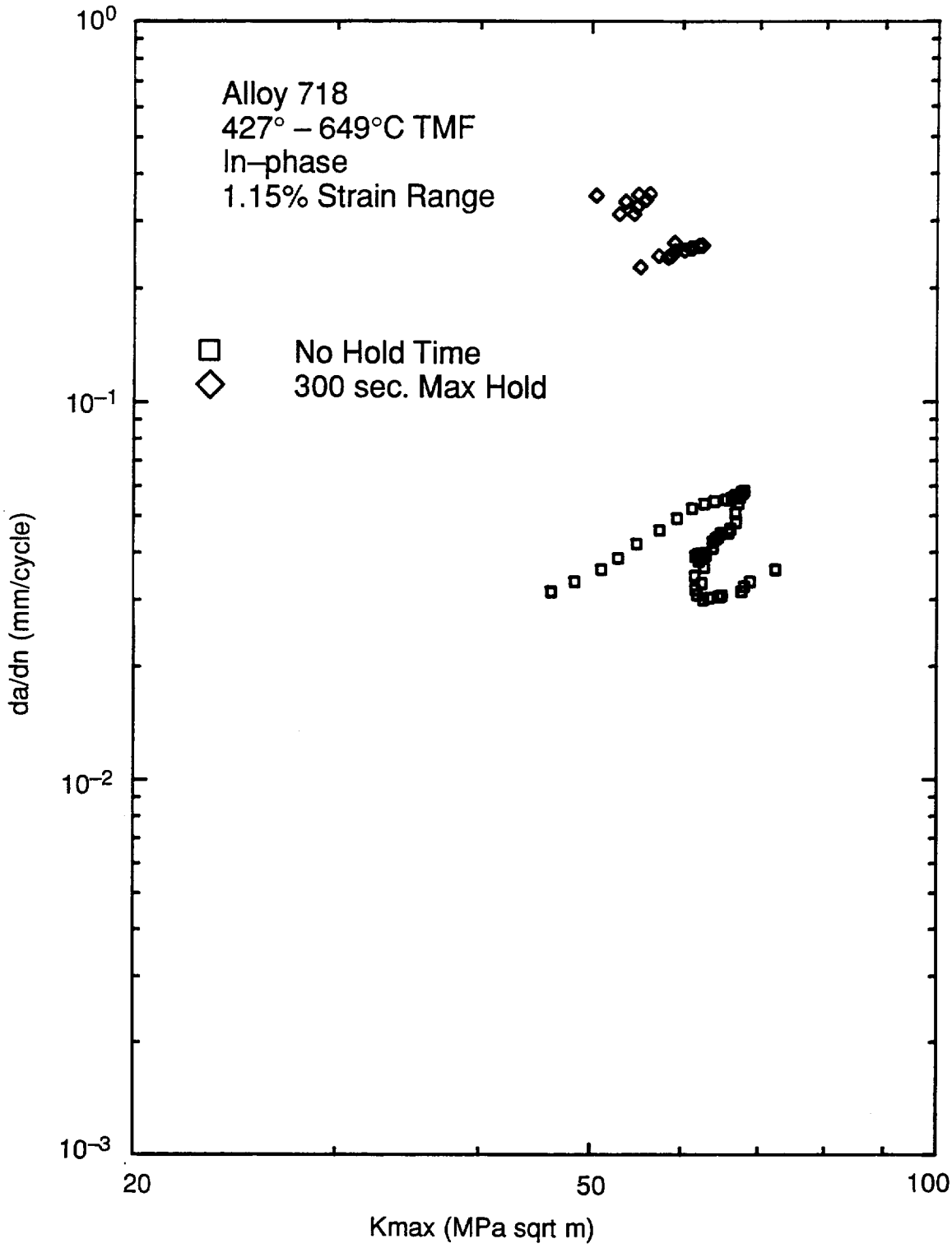

Figure 89. Variation of Alloy 718 crack growth rate with K_{max} for In–phase R_ε= 0 427°–649°C TMF tests with a mechanical strain range of 1.15%.

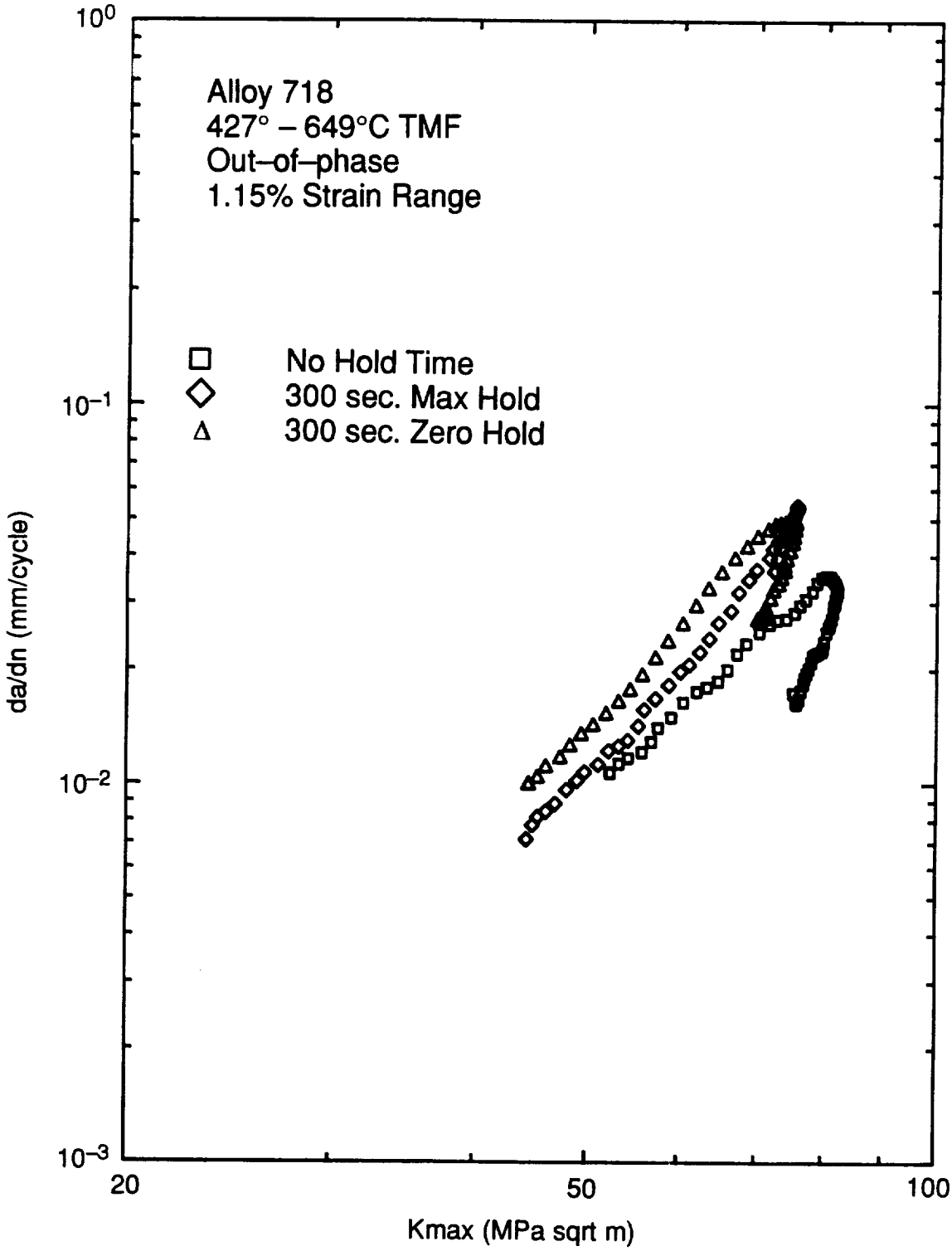

Figure 90. Variation of Alloy 718 crack growth rate with K_{max} for out–of–phase R_ε= 0 427°–649°C TMF tests.

9.0 Summary and Recommendations

The purpose of this program was to review the so-called path-independent integrals which were proposed to eliminate the various restrictions on loading and temperature conditions in the J-integral, and to investigate whether or not these integrals can be utilized to correlate crack growth data under realistic loading conditions. This investigation was performed using combined experimental and analytical efforts. The loading and temperature conditions for crack growth tests included isothermal strain cycling, thermomechanical fatigue loading, strain cycling with temperature gradients, constant strain and constant stress loading, and hold time loading under both isothermal and thermomechanical conditions. The applied strain ranges included loading in both the small scale yielding and in the highly nonlinear loading regimes. Alloy 718 tests were performed over the temperature range form 427°C to 649°C using a buttonhead single edge notch specimen with a short gage length to avoid buckling under compression at high temperatures. In addition, crack growth data generated in a pre-HOST program on Hastelloy-X tubular specimens were analyzed to see if there exists dependence on the material and geometry in the application of these integrals.

The conclusions drawn in this investigation are:

- The integrals J^*, $\hat{J}$, ΔTp^* and ΔTp, and the rate integrals $\dot{J}^*$, $\dot{\hat{J}}$ and $\dot{T}^*$ are path-independent regardless of material constitutive responses. A certain degree of smoothness of the mechanical field variables is, however, required for path independence. These integrals carry physical meaning only in some particular deformation conditions and/or with some assumptions. All these integrals are computable without difficulties.
- The parameters ΔJ^*, $\Delta\hat{J}$ and ΔTp^* appear to correlate crack growth data for time-independent isothermal, thermomechanical deformation conditions and temperature gradient cases. The parameter ΔTp correlated most of the isothermal and TMF crack growth data, but failed in a few cases.
- The rate integrals $\dot{J}^*$ and $\dot{\hat{J}}$ correlated time-dependent crack growth data under constant strain and constant stress conditions, but $\dot{T}p^*$ did not. The non-rate integrals J^*, $\hat{J}$, and Tp^* did not correlate crack growth data under static control conditions.
- Two combinations of parameters, ΔJ^* and $\dot{J}^*$, and $\Delta\hat{J}$ and $\dot{\hat{J}}$, correlated crack growth data for isothermal strain cycling with hold time. The parameters ΔJ^* and $\Delta\hat{J}$ were used for crack growth prediction under strain cycling. The rate parameters $\dot{J}^*$ and $\dot{\hat{J}}$ were used for crack growth prediction during hold time. The superposition method for the total crack growth rate worked satisfactorily only for small applied strains. For large applied strains, a modified superposition method was proposed.
- The TMF crack growth rate varied significantly with the phase between the mechanical loading and the thermal cycling. The crack growth rate was higher for the in-phase loading than the out-of-phase loading. The crack growth data of the same phase may be correlated with ΔJ^*, $\Delta\hat{J}$ or ΔTp^*.
- Overall, the most successful parameters were two pairs of non-rate and rate integrals. They are: (1) ΔJ^* and $\dot{J}^*$, (2) $\Delta\hat{J}$ and $\dot{\hat{J}}$.

Although an extensive amount of work was done in this program and the results obtained appear to be very significant for crack growth prediction, much work remains in order to apply these integral parameters to engineering applications. Some of the specific areas for further investigation are:

- The R_ε ratio used in this investigation was either –1 or 0. In these conditions, the values of the integral parameters at the crack closing point, crack opening point and the minimum strain were very small compared with those at the maximum strain. The ranges of parameters from the minimum strain to the maximum strain were therefore almost identical to those from the crack opening (or closing) point to the maximum strain. It has to be verified whether or not this is true for positive R_ε ratios. If it is not, the effect of crack closing may need to be modeled.
- The effects of the modeling method including the finite element mesh size around the crack path, the loading step size and the node release scheme needs further investigation. The effects of the loading step size and node release scheme for crack growth simulation were examined to a limited extent in this study. A more comprehensive study is recommended to establish the optimum procedure.
- The crack growth analysis in this research was terminated at the crack length 2.54 mm in almost all cases. Experimental data show that the crack growth rate under strain control appears to start to decrease in most specimens near this or somewhat larger crack length. The K_{max} still increases at larger crack lengths for a while. This results in degrading the correlative ability of da/dN with LEFM parameters. It is worthwhile to investigate if similar trends occur with the integral parameters used in this program by extending the analyses to larger crack lengths.
- The FEM-based prediction of the crack growth under static loading and cyclic loading with hold time needs the values of rate integrals such as $\dot{J}^*$ and $\hat{\dot{J}}$. The computation of these values requires an advanced knowledge on the hold time for the crack to advance by the incremental size in the finite-element model. This information is, however, not available *a priori*. Therefore, the analysis must be initiated with an assumed value and an iterative procedure must be taken to find the solution. This is a disadvantage compared with the LEFM approach where the stress intensity factor can be computed directly from the applied load and the crack length. It is needed to develop an appropriate numerical scheme to apply the new integral parameters to the FEM-based crack growth analysis for time-dependent crack growth.
- For general engineering use, the crack growth under TMF loading and thermal gradients should be able to be predicted using isothermal base data. This methodology needs further investigation.
- The parameters selected in this research need to be verified for material, geometry and loading and temperature conditions used in engine components.

References

1. Kim, K.S., Van Stone, R.H., Malik, S.N., and Laflen, J.H., "Elevated Temperature Crack Growth," Final Report, NASA CR–182247, November 1988.
2. Kim, K.S., and Orange, T.W., "A Review of Path–Independent Integrals for Elastic–Plastic Fracture Mechanics," Fracture Mechanics: Eighteenth Symposium, *ASTM STP 945*, 1988, pp. 713–729.
3. Meyers, G.J., "Fracture Mechanics Criteria for Turbine Engine Hot Section Components," Final Report, NASA CR–167896, United Technologies Corporation, Pratt and Whitney Aircraft Engine Group, May, 1982.
4. Rice, J.R., "A Path–Independent Integral and the Approximate Analysis of Strain Concentration by Notches and Cracks," *Journal of Applied Mechanics*, Vol. 13, 1980, pp. 841–850.
5. Kumar, V., German, M.D., and Shih, C.F., "An Engineering Approach for Elastoplastic Fracture Analysis," EPRI Report NP–1931, Electric Power Research Institute, Palo Alto, CA, July 1981.
6. Dowling, N.E. and Begley, J.A., "Fatigue Crack Growth during Gross Plasticity, and the J–integral," Mechanics of Crack Growth, *ASTM STP 590*, ASTM, Philadelphia, 1976, pp. 82–103.
7. Dowling, N.E. and Iyyer, N.S., "Fatigue Crack Growth and Closure at High Cyclic Strains," *Materials Science and Engineering*, Vol. 96, 1987, pp. 97–107.
8. Wilson, W.K. and Yu, I.W., "The Use of the J–Integral in Thermal Stress Crack Problems," *International Journal of Fracture*, Vol. 15, 1979, pp. 377–387.
9. Gurtin, M.E., "On a Path–Independent Integral for Thermoelasticity," *International Journal of Fracture*, Vol. 15, 1979, pp R169–R170.
10. Ainsworth, R.A., Neale, B.K., and Price, R.H., "Fracture Behavior in the Presence of Thermal Strains," Proceedings of Institute of Mechanical Engineer's Conference on Tolerance of Flaws in Pressurized Components, London, 1978, pp. 171–178.
11. Goldmam, N.L., and Hutchinson, J.W., "Fully Plastic Crack Problems: The Center–Cracked Strip under Plane Strain," *International Journal of Solids and Structures*, Vol. 11, 1975, pp. 575–591.
12. Landes, J.D., and Begley, J.A., "A Fracture Mechanics Approach to Creep Crack Growth," *ASTM STP 590*, 1976, pp. 128–148.
13. Blackburn, W.S., "Path–Independent Integrals to Predict Onset of Crack Instability in an Elastic Material," *Internatonal Journal of Fracture Mechanics*, Vol. 8, 1972, pp. 343–346.
14. Kishimoto, K., Aoki, S., and Sakada, M., "On the Path–Independent Integral – J," *Engineering Fracture Mechanics*, Vol. 13, 1980, pp. 841–850.
15. Liu, Y.J., and Hsu, T.R., "A General Treatment of Creep Crack Growth," *Engineering Fracture Mechanics*, Vol. 21, No. 3, 1985, pp. 437–452.
16. Atluri, S.N., Nishioka, T., and Nakagaki, M., "Incremental Path–Independent Integrals in Inelastic and Dynamic Fracture Mechanics," *Engineering Fracture Mechanics*, Vol. 20, No. 3, 1984, pp. 209–244.

17. Brust, F.W., and Atluri, S.N., "Studies on Creep Crack Growth Using T*–Integral," *Engineering Fracture Mechanics*, Vol. 23, No. 3, 1986, pp. 551–574.

18. Hawk, D.E. and Bassani, J.L., "Transient Crack Growth under Creep Conditions," *Journal of the Mechanics and Physics of Solids*, Vol. 34, No. 3, pp. 191–212, 1986.

19. Riedel, H., "Creep Crack Growth," Fracure Mechanics: Percepectives and Directions (Twenties Symposium), *ASTM STP 1020*, ASTM, Philadelphia, 1989, pp. 101–126.

20. Hui, C.Y. and Riedel, H., "The Asymptotic Stress and Strain Field near the Tip of a Growing Crack under Creep Conditions," *International Journal of Fracture*, Vol. 17, 1981, pp.409–425.

21. Smelser, R.E. and Gurtin, M.E., "On the J–Integral for Bi–Material Bodies," *International Journal of Fracture*, Vol. 13, 1977, pp. 382–384.

22. Van Stone, R.H., Gooden, O.C., and Kruger, D.D., "Advanced Cumulative Damage Modeling," AFWAL–TR–88–4146, Materials Laboratory, AFWAL, Dayton, Ohio, 1988.

23. Nicholas, T. and Ashbaugh, N.E., " Fatigue Crack Growth at High Load Ratios in the Time–Dependent Regime," Fracture Mechanics: Nineteenth Symposium, *ASTM STP 969*, T.A. Cruse, Ed., ASTM, Philadelphia, 1988, pp. 800–817.

24. Walker, K.P., "Research and Development Program for Non–Linear Structural Modeling with Advanced Time Temperature Dependent Constitutive Relationships," Final Report, NASA Contract NAS3–22055, United Technologies Research Center, 1982

25. Yuen, Shik Hung, "Development of an Uncoupled Viscoplastic Constitutive Model for Cyclic Plasticity of Hastelloy–X at High Temperatures," Master of Science Thesis, Texas A & M University, 1983.

26. Jordan, E.H. and Meyers, G.J., "Fracture Mechanics Applied to Nonisothermal Fatigue Crack Growth," *Engineering Fracture Mechanics*, Vol. 23, No. 2, pp. 345–358, 1986.

27. Jordan, E.H. and Meyers, G.J., "Fracture Mechanics Applied to Elevated Temperature Crack Growth," *Journal of Engineering Materials and Technology*, Vol. 111, pp. 306–313, ASME, July 1989.

28. *Stress Intensity Factors Handbook*, Y. Murakami, Editor–in–Chief, Pergamon Press, Oxford, 1987.

29. McKnight, R.L., "Finite Element Cyclic Thermoplasticity by the Method of Subvolumes," Ph.D. Thesis, Univeristy of Cincinnati, 1975.

30. Kim, K.S., Van Stone, R.H., Laflen, J.H., and Orange, T.W., "Simulation of Crack Growth and Crack Closure under Large Cyclic Plasticity," Fracture Mechanics: Twenty–First Symposium, *ASTM STP 1074*, ASTM ,Philadelphia, 1990, pp. 421–447.

31. Besseling, J.F., "A Theory of Plastic Flow for Anisotropic Hardening in Plastic Defromation of an Initially Isotropic Material," Report S. 410, National Aeronautical Research Institute, Amsterdam, 1953.

32. Krause, H., *Creep Analysis*, Wiley–Interscience, 1980, Chapter 2.